2019

Single Enzyme Synthesis and Bio-imitation of Functional Nanocrystals

Abdolhamid Sadeghnejad
Lehigh University, abdolhamid9002@gmail.com

Recommended Citation

Sadeghnejad, Abdolhamid, "Single Enzyme Synthesis and Bio-imitation of Functional Nanocrystals" (2019). *Theses and Dissertations*. 4369.
https://preserve.lehigh.edu/etd/4369

Single Enzyme Synthesis and Bio-Imitation of Functional Crystals

by

Abdolhamid Sadeghnejad

A Dissertation Presented to the Graduate and Research Committee
of Lehigh University
in Candidacy for the Degree of
Doctor of Philosophy

in
Chemical Engineering

Lehigh University
Bethlehem, PA

January 2019

Approved and recommended for acceptance as a dissertation in partial fulfillment of the requirements for the degree of Doctor of Philosophy.

Date

Accepted Date

Dr. Steven McIntosh
(Dissertation Advisor)

Committee members:

Dr. Christopher J. Kiely

Dr. Mark Snyder

Dr. Muhannad Sulieman

ACKNOWLEDGMENTS

To begin, I would like to give special thanks to many awesome people in my life. Without them, I believe it would be impossible to complete my academic career as a PhD in chemical engineering. Firstly, I would like to thank my parents, Habibeh and Ali Sadeghnejad for all on-going support in my life. They always encourage me to go forward after any failure by teaching me how to be strong, patient, creative, and motivated in my plans even academic or non-academic. Thanks for your support in my decision of studying abroad, far away of you, emotionally and economically during my academic life.

I would like to thank my advisor, Dr. Steven McIntosh, who made this academic journey productive and possible. You supported me when I really need someone to encourage and motivate me to complete my PhD at Lehigh University. I am grateful to have such a patient and understanding advisor who teaches me how to be a productive researcher.

Also, I would like to thank Dr. Christopher Kiely for being always optimistic, incredible mentor, and supportive whenever I needed a fruitful advising in my projects. I have been fortunate to have you in my PhD committee member. I`d also thank Dr. Mark Snyder and Dr. Muhannad Sulieman, as my PhD committee members who provided me with helpful suggestions and guidance during my research.

My gratitude also extends to my lab mates during the last four years in the lab. Thank you Dr. Zhou Yang, Dr.Chris Curran, Dr. Leah Spangler, Dr. Li Lu, John Sakizade, Nur Ozdemir, and Robert Dunleavy.

Most importantly, none of this would be happen without my beloved wife, Neda Sabbagh. Your loving support help me to be focused on my research more than our new marriage life. Whenever my research was in a terrible direction, or I was frustrated, you`ve been enthusiastic and unconditional supportive to overcome the challenges of life. I cannot thank you enough for your help, feedback, support, encouragement, and great love for every step of the way. Thank you for being in my life!

CONTENTS

LIST OF TABLES

LIST OF FIGURES

Abstract

Green synthesis methods of inorganic materials have gained lots of attention due to lower pollution and toxic precursors during the synthesis. One of the modern green methods of synthesis is biosynthesis in which a DNA, small peptide molecule, or amino acids plays the main role of synthesis. Biomineralization, the biosynthesis process happens in the nature by elements, has been considered as a green, low cost, and scalable method of synthesis. In comparison with conventional synthesis methods, biomineralization happens under ambient conditions in aqueous phase that can be applied for synthesis of inorganic nanostructure metal sulfide semiconductors gained interest due to their remarkable physical and chemical properties such as electronic, magnetic, and optical[1]. Their conventional synthesis methods of semiconductors are cost effective nowadays; however, Environmental-friendly biosynthesis is going to be a potential replacement in near future. Biomineralization of semiconductor nanocrystals (Quantum Dots) offers a low cost and greener approach of semiconductors under ambient conditions in aqueous phase in which a single enzyme plays the role of catalyzing the reaction and templating the nanostructure of quantum dots.

To begin, we showed the templating role of a single protein in biosynthesis of $CaCO_3$ crystallization. In nature, various crystal structure of $CaCO_3$ formation happen by living organisms such as sea shells, snails, and corals. In this study, a single well-known protein, Silicatein α, has been utilized to be responsible for templating the crystal structure of $CaCO_3$ mineralization at ambient conditions in aqueous phase. Templating vaterite and aragonite crystal structure, confirmed by XRD and SEM, in the presence of Silicatein showed a change in state level of $CaCO_3$ crystal structure from calcite to vaterite and aragonite. Also, the influence of protein concentration on aragonite

crystallization has been studied in this work that confirms the role of Silicatein in $CaCO_3$ crystallization.

Furthermore, we have focused on both roles of single enzyme in catalyzing and templating in biomineralization process. In this study, an engineered enzyme called cystathionine γ-lyase (CSE) has been playing two roles in biomineralization of various metal sulfides. First, CSE can turn over L-cysteine to generate reactive source of sulfur, H_2S, in solution continuously. Second, CSE plays the role of templating the nanocrystal growth of metal sulfides.

Single enzyme direct biomineralization of nontoxic metal chalcogenide such as ZnS by utilizing CSE enzyme was reported in this work. Synthesized ZnS, $Zn_{1-x}Cd_xS$ alloy, and ZnS-$Zn_{1-x}Cd_xS$ core-shell showed considerable optical properties such as great absorption and fluorescence lead to 97.6 ns increase in decay time confirmed by life time decay photoluminescent. Also, narrow size distribution, well crystallinity, nanomaterial composition and shape of QDs were characterized by HRTEM, HAADF, and EDAX. Biosynthesized method lead to achieve 7% enhancement in quantum yield.

Also, we have synthesized SnS and Cu_2ZnSnS_4 alloy by utilizing CSE single enzyme in the presence of L-cysteine as a source of sulfur. Biosynthesized SnS nanocrystals and its relative compound, confirmed by XRD and HAADF, showed great photocatalytic property regard to the potential application in quantum dots-sensitized solar cell (QDSCs). SnS and CZTS have been applied as an absorber layer by in-situ growth on TiO_2-paste as a working electrode in the presence of polysulfide electrolyte and Cu_2S cathode. We have presented the uniform penetration of QDs into TiO_2-paste by in-situ growth, confirmed by SEM-EDAX line scanning, that improved solar cell characterization parameters such as V_{oc}, J_{sc}, and FF to 5.5 V, 3.1 $\frac{\mathrm{mA}}{\mathrm{cm}^2}$, and 61%, respectively.

Chapter 1

Introduction

1.1. Motivation

In recent years, semiconductor quantum dots or nanocrystals have gained lots of interest due to their significant optical and electrical properties lead to potential applications in various fields such as energy harvesting, energy storage, and catalytic applications. The synthesis of these materials is typically accomplished in an organic phase at elevated temperature with the addition of a reactive chemical precursor. While these conventional approaches enable fine control over materials, crystallinity, size and often shape, and allow us to achieve highly active functional materials, this synthesis methodology inherently leads to significant environmental and thus economic implications for scale-up.

In contrast, biological process of inorganic materials by living species has inspired researchers to apply various chemicals and synthesis methods to mimic materials with favorable properties, called biomineralization. Biomineralization is a modern and an attractive synthesis method of materials owning to the nontoxic, available, and environment-friendly precursors[2]. Also, synthesis in aqueous phase under ambient conditions leads to a significant interest in developing synthetic biomineralization or bioinspired synthesis routes to generate functional nanomaterials[3]. Thus, biomineralization process can eliminate many economically and environmentally implications for scale-up synthesis routes.

In this work, biomineralization of ZnS and SnS QDs studies by applying an engineered enzyme, cystathionine γ-lyase (CSE), in aqueous phase at ambient conditions. In addition, CSE showed the functionality of making relative alloys such as $Zn_xCd_{1-x}S$, and Cu_2ZnSnS_4 with enhanced quantum yield and optical properties. It was shown that CSE is able to form core-shell structures such as $Zn_xCd_{1-x}S$-ZnS, which causes improvement of QDs optical properties.

Also, it was interesting to demonstrate the influence of biomineralized metal sulfide QDs in different applications. In this work, SnS QDs were utilized in solar cell as an absorber layer in anode to improve the solar cell characterization parameters. Compared with conventional solar cell fabrication methods, direct synthesis of QDs on TiO_2 pate showed better performance than drop casting method. In drop casting procedure, QDs only distribute on the surface of TiO_2 paste. However, in-situ growth of SnS QDs on TiO_2 paste showed that QDs can penetrate into the thickness of TiO_2 paste uniformly as well as uniform distribution on the surface of TiO_2 paste.

In addition to biomineralization o functional nanomaterials such as metal sulfide QDs and their relative compounds, bioimitation of polymorph $CaCO_3$ microcrystals by a protein called Silicatein α has studied in this work. Silaicatein α is a well-known protein in live organism like sea shell that is responsible for changing the crystal structure of $CaCO_3$ calcite to vaterite and aragonite. Thus, it was interesting to imitate the crystallization of aragonite crystal structure by utilizing the purified Silicatein protein and optimize the crystallite of aragonite by tuning the concentration of protein under ambient conditions.

1.2. Background

1.1.1. Quantum Dots Confinement and Optical Properties

A quantum dot is a semiconductor nanocrystal whose diameter varies between 1-10 nm. The size of quantum dots is one of the most important factors that characterize their optical properties that are mostly different from optical properties of the bulks semiconductors. Size and shape of quantum dots result in free charge carriers of semiconductors, which allows some adjustable properties such as band gap, emission color, and absorption spectrum controlled by size distribution of quantum dots during the synthesis. In addition to the small size of quantum dots compared to bulk semiconductors, the number of atoms are very different in quantum dots, i.e.10-50 atoms. While the number of atoms in a bulk semiconductor can be 100-100000 atoms which cause numerous electron interactions and energy level overlaps. On the other hand, quantum dots contain small number of electrons that can move in limited space, often inside the semiconductor crystals.

Bohr radius which is a physical constant for every material that shows the most distance between electron and proton. When the size of quantum dot crystal is equal or bigger than its Bohr radius, band gap, that is the distance between valence and conduction band, keeps constant for each material. Quantum confinement happens when the electrons turn in an orbit smaller than Bohr radius. Regard to optoelectronic applications, important properties of materials such as fluorescence in the UV, visible, or infrared range depend on the energy of emitted light, which is controlled by the amount of quantum confinement, increased at larger band gap, and the band gap, limited to each material.

1.1.2. Quantum Dots as an Alloy or a Core/Shell

The importance of grown core/shell semiconductor materials from IIA to VIA is critical in regard to the bright photoluminescence (PL) and electroluminescence and more stability against photo-oxidations. Decision of what metals can play the role of core/shell quantum dots depends on the band gap of the metals used as a core and shell. If the shell has a higher band gap than the core material, the photogenerated electron and hole of core/shell will be restricted to the core[4].

Since most of the semiconductor metals groups of II-VI are typically have an emission in the visible range, some of the metal groups of IV-VI can be interesting for researchers to synthesis quantum dots as an alloy or a core/shell. For example, CdSe/ZnSe enhanced the photoluminescence properties[5], or $Cd_xZn_{1-x}Se_yS_{1-y}$/ZnS optimized performance and stability of LED by controlling the shell gradient[6], and enhancement in photoluminescence efficiencies and electrical response of CdS Nanorods by adding ZnS Shell to core[7].

1.1.3. Quantum Dots Application

Quantum dots semiconductor materials are known as tunable band gaps, strong stable emission, and low thresholds for multiple excitation generation, which is a significant property compared with bulk materials. These properties can be useful potentially in various fields and industries regard to solid-state lighting[8], bioimaging[9], photovoltaic applications[10], leasers[11], and biological markets[12].

The other application of Quantum dots that some research groups have worked on is in the catalysis area. For example, CdS semiconductor is a well-known photocatalyst that can capture visible light and convert it to chemical energy in different usages such as CO_2 photoreduction, water splitting[13], organic photosynthesis[14].

While conventional organic dyes are photobleaching sensitive, semiconductors quantum dots have been interested due to their tunable emission properties by size and compositions. Conjugation of quantum dots to antibodies or other peptides can be used to target cellular ligands regard to their applications in fluorescence assays or cell labeling. For example, introducing fluorescence semiconductor quantum dots into cytoplasm to track the population of cells[15].

1.1.4. Quantum Dots Biomineralization

Biomineralization is the process in which a living organism used to form structured organic-inorganic materials such as shells, bone, and teeth. Some example of Biomineralization is the formation of cell walls of diatoms, large group of single-celled eukaryotic algae that are mostly living in the water. Diatoms cell walls are made by SiO_2, silica, with amorphous structure and porous pattern. Also, some other organisms been producing mineralized skeleton are carbonates in invertebrates, and calcium phosphates and carbonates in vertebrates. One of the other common biomineralization in the nature is iron oxides, such as magnetite (Fe3O4) in birds and bacteria (navigational devices) and ferrihydrite FeO(OH) in ferritin of mammals, plants, and bacteria.

the study of the mechanisms of biomineralization in general is relatively recent; a great deal of the information currently available to understand the effect of organic molecules such as proteins, lipids, and carbohydrates, which leads to a new, low cost synthesis pathway of functional materials and potentially independent applications.

Recently, biomineralization of quantum dots has been interested as a low cost, environment- friendly procedure, and potential to be applied in industrial scales. Firstly, biomineralization of quantum dots was studied in yeast organism against heavy metals[16–18]. Under biological conditions, some other organisms such as bacteria[19,20], and bi-functional peptide[21] have the ability of form nanocrystals at low concentration of metals. Some studies have investigated in templating the quantum dots in aqueous phase by DNA[22], amino acids[23], or short length peptides[24].

1.1.5. Quantum dots sensitized solar cell

Solar cell is a new technique of converting sun light energy into electrical energy in which solar cell absorber can produce a current flow by absorbing the energy of sun light photons. Three major types of solar cells are dye-sensitized solar cells (DSSC), bulk heterojunction (BHJ) photovoltaic cells or organic photovoltaic cells, and quantum dot solar cells (QDSC). As an important candidate of light absorber, semiconductor nanocrystals present better performance due to simplicity in synthesis, tunability of light absorption, and sensitivity to diffused light. Control of electrical and optical properties of quantum dots due to the size and shape provide the flexibility of tuning solar cell performance. While electron injection from excited dye into semiconductor oxide in DSSC or excited interaction between the polymer and QDs, the principle of QDSC is the separation of photoinduced charge carriers at the interface of semiconductor QDs, semiconductor oxide, and electrolyte.

Semiconductor oxide as an acceptor and redox couple reaction of electrolyte as scavenger can increase the lifetime of charge carrier, which leads to photocurrent delivery. Also, the assembly of liquid junction solar cell (or QD-sensitization solar cell) needs to deposit of thin layer of metal such as Au or Pt on top to make an electric contact as a cathode.

The first aspect of solar cell performance is photocurrent, that is basically the separation of photogenerated electrons and holes that is limited to the absorption properties of absorber. The absorber can absorb photons with the energy greater than the band gap energy of absorber. The other absorption limitation of absorber is the weak absorption in the visible region between specific wavelength, for example organic absorbers strongly absorbs light around 430 nm to 660 nm. The second aspect is photovoltage, that is the maximum voltage produced by solar cell. As light shines on the absorber, more photoexcited carriers are produced the carrier bands, that causes the separation of Fermi level of absorber. Photovoltage is basically the potential difference between the Fermi level of electrons in metal oxide and the redox level of electrolyte (Figure 1). Photoexcited electrons migrate from absorber to the metal oxide and the holes transfer to redox carrier. The accumulation of carriers in the metal oxide and redox carriers are relevant to the recombination mechanism, which is the main limitation in photovoltage. At higher voltage, the dominant charge recombination mechanism is the recombination from the metal oxide to the electrolyte[25]. Deposition of large absorption semiconductor on metal oxide such as TiO_2 can play as an effective blocking layer to avoid recombination of electrons from metal oxide to redox couple carriers in electrolyte.

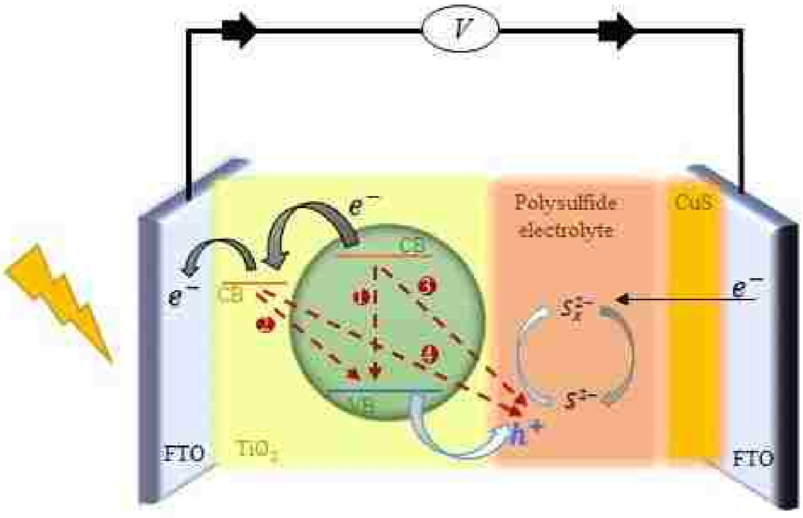

Figure 1: Scheme of QD sensitized solar cell showing Voc at open circuit condition

Maximum open circuit voltage (V_{oc}) occurs when there is no load connected to the solar cell or no current flowing between photoanode and cathode through external circuit. As mentioned above, V_{oc} depends on the difference potential of fermi level of TiO_2 and redox level of electrolyte that is independent to the light intensity, which is the reason of low changes in V_{oc} when current starts to increase under illumination. Based on the suggested formula that can predict the voltage at which current described in I-V curve, the voltage depends on saturation current, temperature, and fabrication of cell.

$$V_{oc} = \frac{nkT}{q} Ln(\frac{I_L}{I_0} + 1)$$

Theoretical estimation of voltage by difference potential of fermi level in photoanode and redox level of electrolyte can be found by band alignment in which valence band offset (VBO) and conduction band offset (CBO) should be calculated for the junction. VBO is calculated by the following formula:

$$VBO = E_{VB}^{b} - E_{VB}^{a} + V_{bb}$$

Where E_{VB}^{b} and E_{VB}^{a} are the valence bond energy positions of two materials as a junction (such as TiO_2 and QD) that can be found by photoelectron spectra in XPS. Also, V_{bb} is the band bending that is the energy difference of core levels of species a and b at interface. Then, the CBO can be calculated by following formula:

$$CBO = VBO - \Delta E_g$$

Where ΔE_g is the difference in band gaps of two species that can be found by their absorption spectrum[26–28]. Figure 2 shows the band diagram of a CdS sensitized solar cell and maximum theoretical V_{oc} that is the potential difference in fermi levels of photoanode and electrolyte.

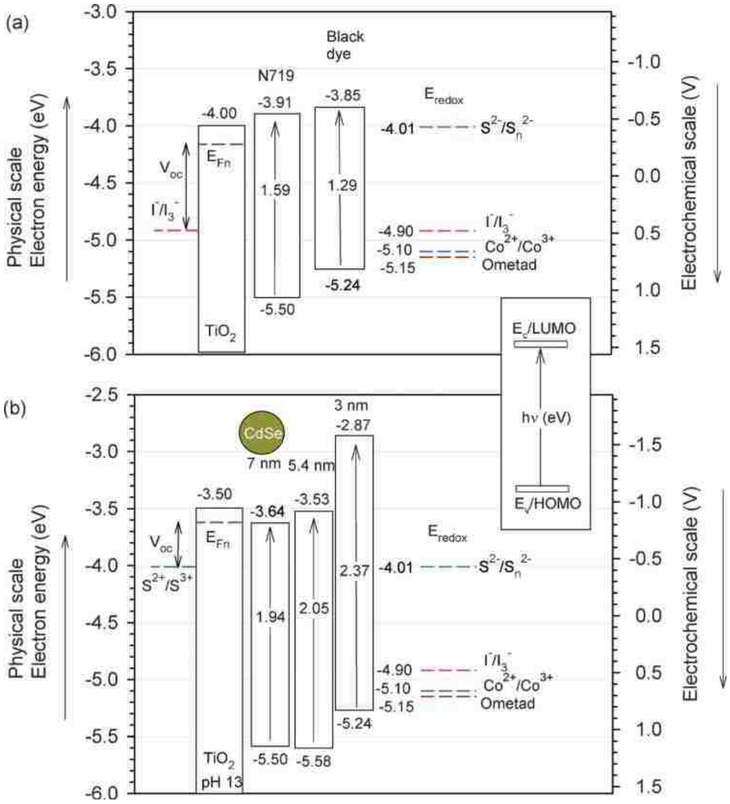

Figure 2: Diagram of Energy band alignment of components in QDSSC showing maximum Voc that is the potential difference between fermi level of photoanode and redox level of electrolyte29.

Under illumination, excess of charged carriers can increase electron flow from photoanode to cathode for redox couple regeneration, while ideally the V_{oc} is still constant until the maximum amount of current (I_{sc}) is reached at short circuit condition in which potential difference is zero, Figure 3a.

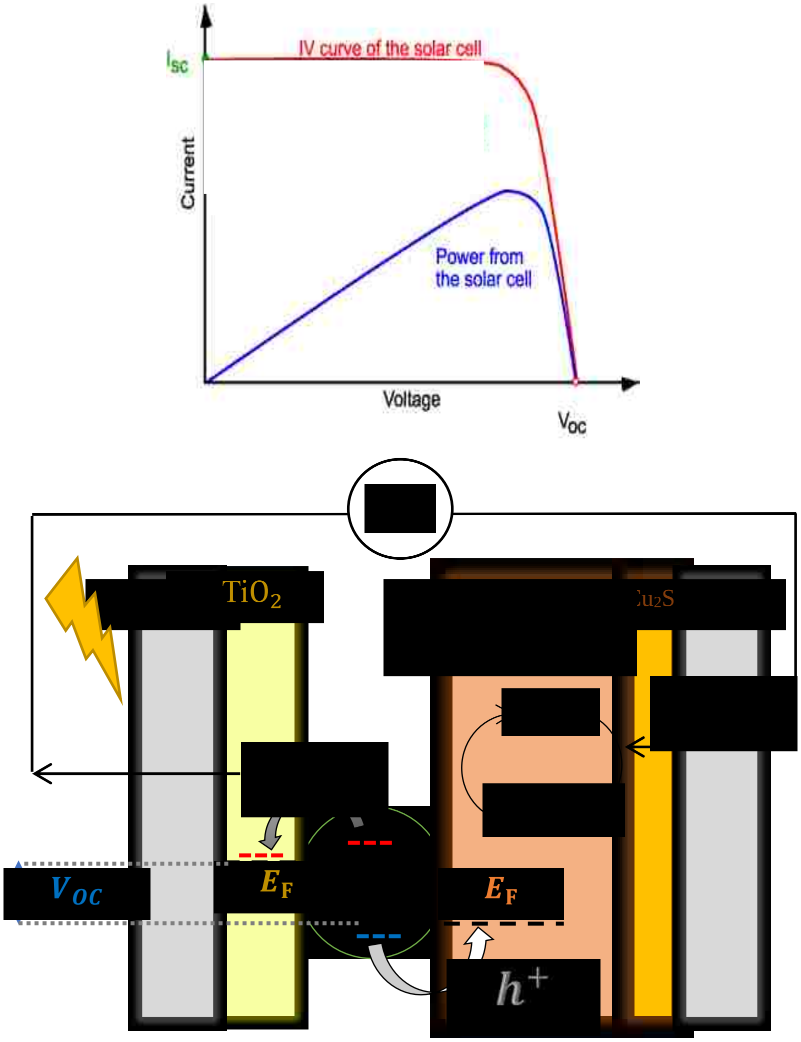

Figure 3: (a) I-V curve of solar cell under illumination showing V_{oc} and I_{sc}, describing the current at which voltage. (b) scheme of QD sensitized solar cell in short circuit condition

In opposite to voltage, current strongly depends on number of photons (light intensity), optical properties, and area of absorber, describes by suggested formula:

$$I = I_L - I_0\ [\exp\left(\frac{qV}{nkT}\right)]$$

The series of charge carrier transfer process in QDSC includes (1) photogenerated electron excited from valence bond to conductive bond of light absorber (or metal chalcogenide such as SnS), (2) the photoexcited electron migrates to the conduction bond of metal oxide such as TiO_2, (3) electron transports to the collecting electrode surface, (4) photogenerated hole in valence bond of absorber transfers to the redox couple carriers (electrolyte), (5) regeneration of electron-hole pair through the redox couple reaction at the counter electrode. While excited electron start migration from conduction bond of absorber to regenerate with hole in counter electrode favorably, there are couple of two factors that cause losses in solar cell efficiency such as recombination and resistance. The main recombination forces occur in the interface of working electrode and electrolyte such as (1) recombination of excited electron in conduction band of QDs with redox couple in electrolyte, (2) recombination of transferred electron in metal oxide with redox couple in electrolyte. Many reports describe and estimate the rate of charge transfer in each process to have a better understanding of charge carrier mechanism and to improve solar cell efficiency. The most effective recombination process that changes the efficiency is the recombination of excited electron from TiO_2 to redox couple. Also, it is reported that the main resistance in solar cell fabrication happens in the interface of electrolyte and counter electrode[29].

Charge transfer rate of electron migration from QDs to metal oxide is reported in the range of 1.9×10^{10} to $4.6 \times 10^{11}\ s^{-1}$. Minimizing the losses due to recombination happens with ultrafast injection of electrons form QDs into semiconductor oxide and quick scavenging of holes by redox couple in electrolyte. In the absence of electrolyte, electron-hole recombination happens as a natural decay of QD[30]. However, in the presence of electrolyte, regeneration of electron-holes occurs in counter electrode interface. The rate of hole transfer from QD to the redox couple is $8.5 \times 10^{7}\ s^{-1}$ that is 2-3 magnitude of order lower than electron migration rate of electron from QD to metal oxide. This lower rate causes the accumulation of holes in valance band of QDs, which increases the rate of electron-hole recombination. Improvement of liquid junction QDSC is reached to 10.9% efficiency recently[31].

In the presence of electrolyte such as Na_2S, hole trapping and hole scavenging happen by S^{2-} in electrolyte to produce $S^{\cdot-}$ radicals. Then, sulfide radicals react with S^{2-} ions to generate polysulfide radicals.

$$S^{2-} + QDs\ (hole)\ \rightarrow\ S^{\cdot-}$$

$$S^{\cdot-} + nS^{-2}\ \rightarrow\ (S_{n+1})^{\cdot-}$$

As mentioned before, one of the main recombination mechanisms is the recombination of TiO_2 electron and redox couple due to poor charge rate of redox couple regeneration at counter electrode. In this case the reduction of polysulfide radicals occurs by electrons injection from TiO_2 with the rate of $5.2 \times 10^{3}\ s^{-1}$.

$$(S_{n+1})^{\cdot-}\ + TiO_2(e) \rightarrow\ (S_{n+1})^{2-}$$

In addition of hole accumulation in QDs valence bond due to the slow rate of hole transfer from valence bond to redox couple, anodic corrosion is another effect of slow rate of hole scavenging. Under illumination, small changes in the electrolyte medium forms a thin layer of sulfide on QDs. The formation of sulfide layer can act as a barrier for the main recombination mechanism from photoanode to the redox couple of polysulfide electrolyte. As a result, coating of QD particles with large band gap such as ZnS can achieve better solar cell performance. Additionally, surface treatment of electron collecting material of counter electrode such as a thin TiO_2 passivating layer, as a blocking layer, can decrease back electron recombination from photoanode to electrolyte. Reduction reaction at counter electrode interface happens by electron discharge in counter electrode.

$$S_n{}^{2-} + e^- \rightarrow nS^{2-}$$

One of the considerable reasons that causes back electron transfer from photoanode to electrolyte is overpotential in counter electrode. Low rate of charge transfer between polysulfide electrolyte and Pt as counter electrode is due to high resistance in interface of electrolyte and counter electrode. The effect of counter electrode resistance is reflected as a size of first arc in Impedance spectrum as well. Alternative counter electrode such as Cu_2S presents lower resistance with polysulfide and better solar cell efficiency[32]. Although the sheet resistance of Cu_2S as a counter electrode is higher than Au, however, very small charge transfer resistance (2 magnitude of order) at the interface of Cu_2S and polysulfide causes better performance of solar cell[33].

Chapter 2

Experimental Details

2.1. Expression and purification of Silicatein α

The modification and expression of engineered Silicatein-α from Escherichia coli BL21 (DE3) is described in detail elsewhere[37,40]. Briefly, the modified silicatein was grown at 37◦C for 16 hours in 200 ml LB broth media. Then, 200 ml grown media was added to 800ml fresh LB broth in the presence of 1mM IPTG, and the total 1000 ml media is kept at 20˚C for 24 hours for further expression. Then, expressed media was centrifuged in 10 minutes at 8500 rpm to make pellet, then it was resuspended in 30 ml D.I. water and 3 ml bugbuster (10X protein extraction reagent, Novegan). The solution was shaked for 1 hour to break the cell wall of E.coli and release the protein. To get rid of heavy protein and impurities, the solution was centrifuged in 10 minutes at 8500 rpm, and supernatant of cell lysis was purified by Immobilized Metal Affinity Chromatography (IMAC) according to the described method previously[37,41]. Then, purified protein solution was dialyzed 4×4 h (Thermo Scientific Snakeskin 3.5 kDa MWCO) against D.I. water to get rid of residual salts of IMAC process. The purified protein was stored in 4˚C before uses. Concentration of purified protein was measured by adsorption of protein solution at 280 nm and Beer-Lambert law[37].

2.2. Biomineralization of $CaCO_3$ crystals

$CaCO_3$ crystallization occurred in the presence of $CaCl_2$ (Fisher Science) as a source of Ca^{2+} cations in the solution. As a source of carbonate, CO_2 was mixed with $(NH_4)_2CO_3$, and the mixture of gas was bubbled through each solution with the rate of

100 mL/min in 200ml flask. Then, samples were centrifuged at 8500 rpm in 10 minutes and pellets were dried at room temperature for crystal characterization analysis. In the first set of experiment, depend on the type of $CaCO_3$ crystals, biomineralization of calcium carbonate methods, being different in precursors, was initiated by adding either a mixture of (i) 50mM $CaCl_2$ and purified protein (6.75µM) to form vaterite, or (ii) 50mM $CaCl_2$, 125mM $MgCl_2$, and purified protein (6.75µM) to form aragonite crystal structure. The CO_2 gas mixture was bubbled into the solution for 16 hours. As a control sample, calcite crystal structure was formed only by 50mM $CaCl_2$ and protein absence under the same synthesis procedure as the primary samples. In the second set of experiments, the effect of Silicatein was tested by both (i) 50mM $CaCl_2$, 125mM $MgCl_2$, and purified protein (6.75µM) and (ii) 50mM $CaCl_2$, 125mM $MgCl_2$, and 500mM imidazole. Also, to understand the function of time, aragonite was biomineralized by 50mM $CaCl_2$, 125mM $MgCl_2$, and purified protein (6.75µM) and CO_2 gas mixture was bubbled at 4, 12, 16, and 24 hours. Finally, in the last set of experiments, the aragonite biomineralization ratio was improved by tuning the ratio of Mg:Ca changed in 0.1, 0.5, 1, 1.5, 2, and 2.5 in the presence of purified protein (6.75µM) and CO_2 gas mixture for 16 hr. Also, the effect of Silicatein concentration was tuned from 2.25 to 9 µM in the presence of 50mM $CaCl_2$, 125mM $MgCl_2$ and 16 hours CO_2 gas flow.

2.3. Expression and purification of SCE

The development, expression and purification of the smCSE enzyme has previously been described in detail elsewhere[34]. This enzyme was previously identified as being associated with CdS quantum dots biomineralized utilizing a strain of *Stenotrophomonas maltophilia* bacteria[35]. Briefly, an *E. coli* codon optimized form of smCSE was expressed within a BL21 strain of *E. coli.* The *E. coli* was grown to saturation at 37 ^{o}C, prior to dilution to OD 600 = 0.8 and induction of expression utilizing 1mM IPTG followed by incubation for 16 h at 20 °C. Cell lysis was achieved by re-suspending centrifuged cells in lysis buffer and sonicating. Finally, the enzyme was purified utilizing immobilized metal affinity chromatography[36] within an imidazole buffer. The purified enzyme was stored at 4°C in imidazole buffer prior to use.

2.4. Biomineralization of ZnS quantum dots

ZnS nanocrystals were grown by incubating a buffered solution (Tris–HCl at pH 9) of zinc acetate (1 mM, Alfa Aesar Puratronic, 99.995% metals basis), L-cysteine (8.25 mM, Spectrum Chemicals, 99.55%), and smCSE enzyme (OD_{600}=500) at 37 °C. An analogous procedure was utilized for CdS and ZnS-CdS alloy nanocrystal synthesis by varying only the cadmium acetate (1 mM, Alfa Aesar Puratronic, 99.995% metals basis) and zinc acetate molar ratios in solution. The nominal Zn:Cd ratios utilized in the current study were 0:1, 1:1, 2:1, 3:1, 4:1, and 1:0.

2.5. Biosynthesis of ZnS-$Zn_xCd_{1-x}S$ core-shell

Following the designated incubation period, the resulting solution was dialyzed (3500 MWCO, Thermo Scientific) against deionized water at 2°C for one day with the water being refreshed every 6 hr. Subsequent ZnS shell biomineralization was achieved using a similar approach. 1 mM zinc acetate, 8.25 mM L-cysteine, and 0.5 OD of smCSE enzyme were added to a dialyzed solution of $Zn_xCd_{1-x}S$ core nanocrystals and the solution incubated at 37°C for 3 h. For comparative purposes, conventional $Zn_xCd_{1-x}S$ nanoparticles were chemically precipitated from a 4mM zinc acetate, 1mM cadmium acetate and 8.25mM L-cysteine aqueous solution by addition of 8.25mM Na_2S.

2.6. Phase transfer

After synthesis the nanocrystals were sometimes phase transferred into an organic phase of 1/1 v/v oleylamine (98%, Aldrich, primary amine)/1-ctadecene (90%, Alfa Aesar) to facilitate sample characterization11. Phase transfer was accomplished by forcing contact between the aqueous solution and the organic mixture at 70 °C for 3 h by vigorous stirring. The nanoparticles in the organic phase were then precipitated with ethanol, centrifuged at 8500 rpm for 15 min and the resulting pellet was suspended in toluene. Samples for TEM analysis were prepared by drop-casting diluted dialyzed nanocrystal solution onto a holey carbon coated Ni-mesh grid and allowing the solvent to evaporate.

2.7. Biomineralization of SnS and CZTS quantum dots

SnS was biomineralized in buffered solution (Tris–HCl at pH 7) of tin (II) chloride (Alfa Aesar, Anhydrous, 98%), L-cysteine (8.25 mM, Spectrum Chemicals, 99.55%), and purified smCSE enzyme (OD_{600}=500) incubated at 37 °C for 6 hr. A similar procedure was utilized for biomineralization of $Cu_xZn_ySn_zS_4$ (CZTS) alloys by addition of copper acetate (Alfa Aesar Puratronic, 99.995% metals basis) and zinc acetate (Alfa Aesar Puratronic, 99.995% metals basis), to the tin (II) chloride buffered solution (Tris–HCl at pH 7). Optimization of the CZTS composition within the biomineralized nanocrystals was achieved by changing the molar ratio of Cu:Zn:Sn in the solution within the range 1:6:6 to 6:1:1.

2.8. QDSCs assembly

Two approaches were adopted to prepare quantum dot sensitized TiO_2 solar cell anodes; either drop casting of preformed QDs onto a preformed TiO_2 matrix or in-situ growth of QDs within the TiO_2 matrix. The TiO_2 anode structure was formed utilizing a standard process for both cases. FTO glass (Sigma Aldrich, 7 Ω sq^{-1} of glass) was cleaned by sonication in 1:10 Contrad 70 soap-deionized water solution for 15 minutes, followed by sonication in 200 proof ethanol for 15 minutes[36]. The TiO_2 layer was formed utilizing the approach previously reported by Kumnorkaew et al[39]. A TiO_2 blocking layer (13 µm) was deposited on the clean FTO by submerging the glass at 70°C for 30 min in diluted $TiCl_4$ (40 mM) solution. A 1 cm^2 area of the dried and washed substrates was coated with TiO_2 paste (opaque titania paste, Sigma Aldrich) utilizing a doctor blade method and Scotch magic tape (3M) to set the height. Annealing the resulting structure at 450 °C for 1.5 hrled to a 13 µm thick porous coating of TiO_2 on the FTO substrate. Drop cast electrodes were prepared by dropping 20 µl of as-synthesized biomineralized QD solution onto the anode with overnight drying at room temperature. In-situ growth of quantum dots in the anode structure was achieved by the TiO_2-coated FTO glasses into the biomineralization solutions described above and incubating at 37 °C for 6 hr.

The CuS cathode was prepared by electrochemical deposition of Cu on cleaned FTO glasses followed by a sulfidation step[40]. Cleaned FTO glass was immersed in 9mM Cu_2SO_4 electrolyte solution with a Cu foil counter electrode and a current of 80 mA/cm^2 held for 2000 cycles. The deposited Cu was washed by with deionized water and ethanol and dried at room temperature. The Cu-coated FTO was then immersed in 1M Na_2S solution for 1 minute followed by washing with ethanol[40].

The solar cells were assembled by clamping the two electrodes together with one layer of Parafilm (13 µm) as spacer and seal. The polysulfide electrolyte, 1 M Na_2S (Alfa Aesar), 1 M S (Alfa Aesar, 99.5%), and 0.1 M NaOH(BDH)[41], was injected into the interstitial space to complete the cell. Electrical connections were made by conductive copper tape (VWR). The electrochemical performance of the cells was analyzed utilizing a Reference 3000 potentiostat (Gamry Instruments). Current-Voltage (J-V) curves were recorded at a linear sweep voltammetry rate of 100 mV/s under 1 sun illumination (Solar simulator, ABET technology). Every solar cell was tested 3 times and the average performance was presented in J-V curve to measure the solar cell characterization parameters.

2.9. Instrumental characterization

The UV-Vis absorbance spectra of the solutions were collected periodically during this incubation period using a 2600 Shimadzu spectrophotometer with an ISR-2600-Plus integrating sphere.

Photoluminescence spectra were collected utilizing a QuantaMaster 400 spectrometer, (Photon Technology International) with excitation wavelength corresponding to the maximum absorbance wavelength. The quantum yields were measured utilizing Coumarin 1 (Sigma-Aldrich) in ethanol as a reference compound following dialysis of the as-synthesized materials[39]. Photoluminescence decay times were collected using g a Fluorolog Spectrofluorometer equipped with a Deltadiode laser having a peak wavelength of 287nm.

After synthesis the nanoparticles were precipitated with ethanol, centrifuged at 8500 rpm for 15 min and the resulting pellet was suspended in D.I. water. Samples for TEM analysis were prepared by drop-casting diluted dialyzed nanocrystal solution onto a holey carbon coated Ni-mesh grid and allowing the solvent to evaporate. High angle annular dark field (HAADF) imaging and X-ray energy-dispersive spectroscopy (XEDS) were conducted at 200kV using an aberration corrected JEOL ARM 200CF analytical electron microscope equipped with a JEOL Centurio XEDS system. Spherical equivalent particle size distributions were calculated from HAADF-STEM images using the Gatan Digital Micrograph software.

Additional XEDS spectra were collected on centrifuged and dried samples utilizing a Hitachi 4300SE/N FEG-SEM equipped with a light element energy dispersive (EDS) and electron backscatter diffraction (EBSD) camera. Samples were stick to a carbon tape on aluminum holder for SEM analysis at 8 kV.

The $CaCO_3$ Crystal polymorphs and crystallinity of particles were detected by X-ray powder diffraction measurement carried out by PANalytical XPert Pro PW3050/60 diffractometer with CuKα radiation with scanning angle between 20˚C-60˚C at room temperature and 40 kV. All of the achieved patterns were fitted by Highscore software at Lehigh University. All of the achieved patterns were fitted by GSAS-II software at Lehigh University.

Photovoltaic properties of SnS and CZTS were demonstrated by J-V curves plotted by running linear sweep voltammetry program of Gamry instrument reference 3000 under 1 sun illumination.

Chapter 3

Bio-mimetics of Calcium Carbonate Confined in Aragonite Crystals by a Single Silicatein α Protein

3.1. Introduction

Calcium carbonate is one of the abundant biological elements that is formed by organism in nature, and all three crystalline polymorph of calcium carbonate (calcite, vaterite, and aragonite) existed in organism are biomineralized under specific conditions[1–3]. Since each of calcium carbonate morphology has different mechanical properties, altering the kinetic of crystallization, control the nucleation, polymorph selection, and final morphology of mineral have been studied in past few years by utilizing biomacromolecules, called biomineralization, to achieve $CaCO_3$ with favorable crystallite and specific mechanical properties[4,5] in a non-toxic and environment-friendly synthesis route. Calcite is the most thermodynamically stable crystal that can be synthesized readily at room temperature and atmospheric pressure. The second structure, vaterite is not the thermodynamically favored stable under these conditions of $CaCO_3$, that causes lower presence as mineral or biomineral in nature. Some of the biological structures that showing the presence of vaterite are eggshell of Pelodiscus sinensis (soft-shelled turtle)[9], Lackluster Pearls[10], and asteriscus[11]. Also, vaterite has been found as a part of elements in Portland cement[12], gallstone[13], and meteorite[14]. Unique properties of vaterite such as high surface area, small specific gravity, and better dispersibility[15] in water attract more attention in vaterite crystal structure as potential industrial substances for paper and cement[16]. Recently, researchers have applied vaterite crystal structure as bioactive filler in degradable polymers for regeneration of bones[17,18], coating pigment[19], and anticancer drug delivery[20].

The third $CaCO_3$ crystal structure, aragonite, is a metastable but desirable structure with typically high aspect ratio crystallites that can be applied in the rubber and paper industries[6]. For example, aragonite can improve the quality of paper such as luster and color during the printing. Aragonite may also be applied in the biomedical industry as it is denser than calcite and can be integrated, resolved and replaced by bone[7,8]. Natural, biomineralization of $CaCO_3$ in aragonite crystal structure happens by marine species in several conditions depends on the nucleation barriers, pH, temperature, and concentration of inorganic materials in sea water[21,22]. Researchers have studied mimic of aragonite formation by adding soluble polymers such as PVA[23], organic additives likes cetyltrimethylammonium bromide(CTAB)[24], organic solvents like glycol[25], and surfactant macroemulsions[26] that can change the kinetics of $CaCO_3$ nucleation to aragonite crystal structure. The most drawbacks of previous works in aragonite synthesis are long reaction time[27], high temperature[28], and combination of two morphologies in irregular shape and size[29]. However, inorganic synthesis of aragonite crystal has been more interested to overcome most of difficulties in chemical synthesis routes.

One of the well-known inorganic additives to form the aragonite crystals is adding Mg^{2+} to the solution as the most influenced ion. Mg^{2+} is the most favor ion to form aragonite with Orthorhombic crystal system. However, previous studies achieved the formation of aragonite in the presence of Mg^{2+} showed some drawbacks in their synthesis routes such as applying further additives like chitin and cellulose[28], and imidazolium-based ionic liquids[30]; or, they worked under specific conditions of synthesis such as elevated temperatures[31], high-power ultrasonic[32], and microwave irradiation[33]. To overcome these issues of aragonite formation in the presence of Mg^{2+}, enzymatic synthesis pathway of aragonite formation by utilizing biomolecules that have significant functional groups (amino and carboxyl groups) to bind to the Ca^{2+} successfully, has attracts a new attention.

Native or recombinant forms of Silicatein have been previously applied in biomineralization of different oxides such as Gallium oxide[34], Titanium oxide[35], Tin dioxide[36], and ceria nanocrystal[37]. It has been demonstrated that Silicatein plays the main role in polymorph controlling and selection in crystallization routes[38,39]. Silicatein α is characterized an anionic polar amino acids[27] because of the presence of nearly 13 % Asx residues in the protein sequence carrying terminal sialic acid or anionic groups. Furthermore, Multiple residues such as Lys, Arg, Ser, Thr, and Glx involving more than 27 % of sequence causes that Silicatein play the role of polar protein in biomineralization, while only 12 % non-polar Gly residue is present in Silicatein sequence.

In this study, we describe the biomineralization of aragonite and vaterite crystals in the presence of Silicatein α protein and Mg^{2+} as an associated catalyzer. Hence, three sets of experiments are designed. First, to change the nucleation of crystals and control the morphology of $CaCO_3$ crystal structures, calcite, vaterite and aragonite are synthesized by utilizing Silicatein and Mg^{2+}. Since aragonite is the favorite $CaCO_3$ crystal structure with significant mechanical properties, second set of experiments provide better insights into the mechanism of protein in biomineralization of aragonite. The last set of experiments are tuning the ratio of Mg:Ca and increasing the concentration of protein to improve the ratio of synthesized aragonite as an interested $CaCO_3$ crystal.

3.2. Results:

3.2.1. $CaCO_3$ polymorph selection and Aragonite biomineralization

Bubbling CO_2 into precursor solutions causes the white precipitation in the solution at room temperature, that cannot be observed initially in the solution when precursors are mixed. Table 1 presents precursors concentration and experimental conditions in synthesis and morphology selection between $CaCO_3$ crystal structures.

Table 1: experimental design of precursors concentration and experiments condition in crystallization of three CaCO3 morphologies. The percentage of each resulted crystal structure was simulated of raw XRD data, Figure 4, by GSAS-II software.

	Concentration			**CO_2 flow**	**Particle precipitation**		
	$CaCl_2$ (mM)	Silicatein (µM)	$MgCl_2$ (mM)	(ml/min)	Calcite (%)	Vaterite (%)	Aragonite (%)
1	50	-	-	100	100	-	-
2	50	6.75	-	100	15.6	84.4	-
3	50	-	125	100	100	-	-
4	-	6.75	125	100	-	-	-
5	50	6.75	125	-	-	-	-
6	50	6.75	125	100	17.8	-	82.2

As a control morphology, calcite crystallization starts by injection of CO_2 into the solution in the presence of only $CaCl_2$, that increases the amount of white precipitation as time goes on. No particle precipitation occurred without bubbling the mixture of CO_2 and $(NH_4)_2CO_3$ into the each of solutions.

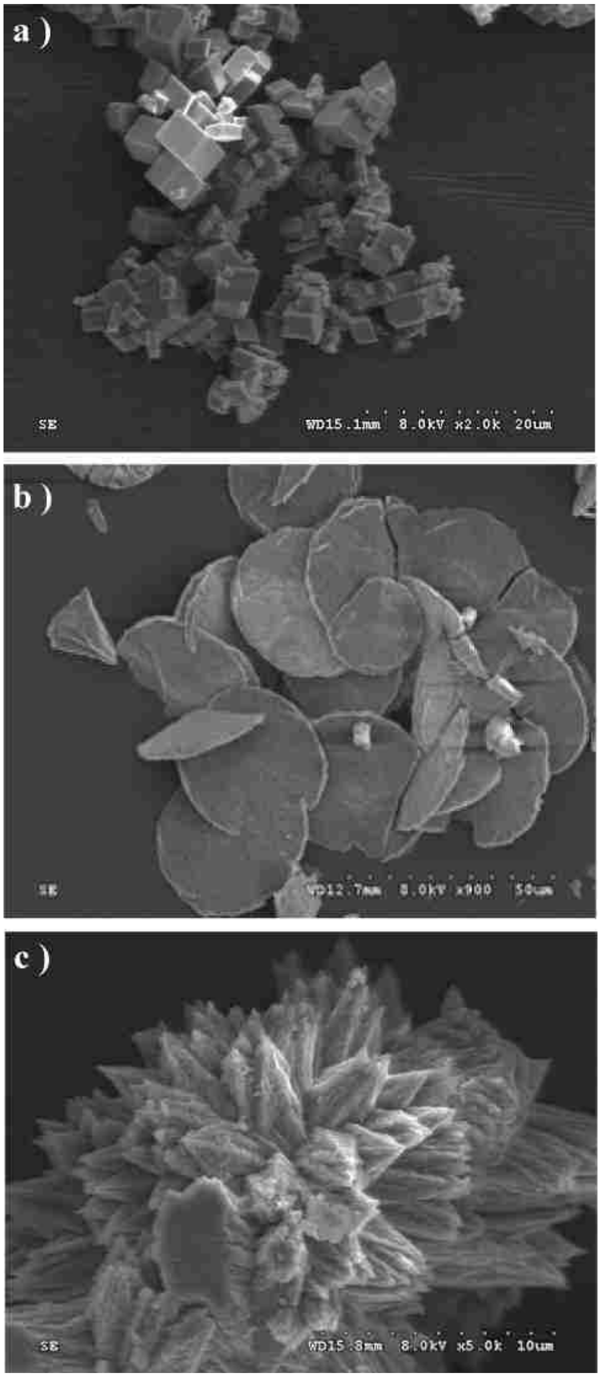

Figure 4: Typical SEM image of dried precipitated a) Calcite as a control sample in the presence of $CaCl_2$, b) Vaterite (mixture of protein and $CaCl_2$), and c) Aragonite morphology (mixture of $MgCl_2$, protein and $CaCl_2$) at 8KeV. Samples were coated by Iridium before imaging.

The characterization of calcite structure is presented in Figure 4(a) in which cubic morphology of agglomerated particles are seen in the typical SEM image. However, adding certain concentration of purified protein to the $CaCl_2$ solution affects the shape of precipitated particles to the Mushroom-like lamellar aggregation, Figure 4(b). The main reason of morphology change in $CaCO_3$ crystal is due to the presence of protein in the solution that influences the nucleation of crystals. The formation of vaterite in the presence of Silicatein can be explained by hydrogen bridge between Ca^{2+} and functional groups of Silicatein such as Ser and Glx amino acid residues, 20 % of protein sequence, providing a source of Hydrogen-binding[40]. Although This binding can play the role of primary nucleation of vaterite instead of calcite, but partial transition of vaterite to calcite can happen due to the weaker binding or lack of enough functional groups of Silicatein.

Based on the Ostwald rule, the least stable morphology formed initially is transformed into higher stable phases sequentially. However, some transformation happens if the growth of other morphologies is inhibited. Since the vaterite is unstable, it can transform to the aragonite when Mg^{2+} avoids the growth of vaterite and calcite. This sequence is very similar to others applied different salts or additives to form aragonite[41]. So, the next approach of $CaCO_3$ crystallization can be achieved by adding both protein and $MgCl_2$ into the $CaCl_2$ solution to form aragonite morphology observed as striation lines that outgrowing from one pole of the cluster to different angles, complex intergrowth aragonite crystal structure[42], Figure 4(c). Multi angle orientation of crystals is caused by crystal growth competition[43], in which one particle with fast growth direction can compete with others in other direction and successfully becomes the predominant direction. As the particle outgrowing in the predominant direction is determined, local nucleation of the remaining particles starts in a radial symmetry. Hence, high density of local spicules in aragonite crystals can be seen pointed out from one pole of the cluster[42]. Needle-shaped aragonite crystals can be observed by SEM at a specific range of Mg:Ca ratio.

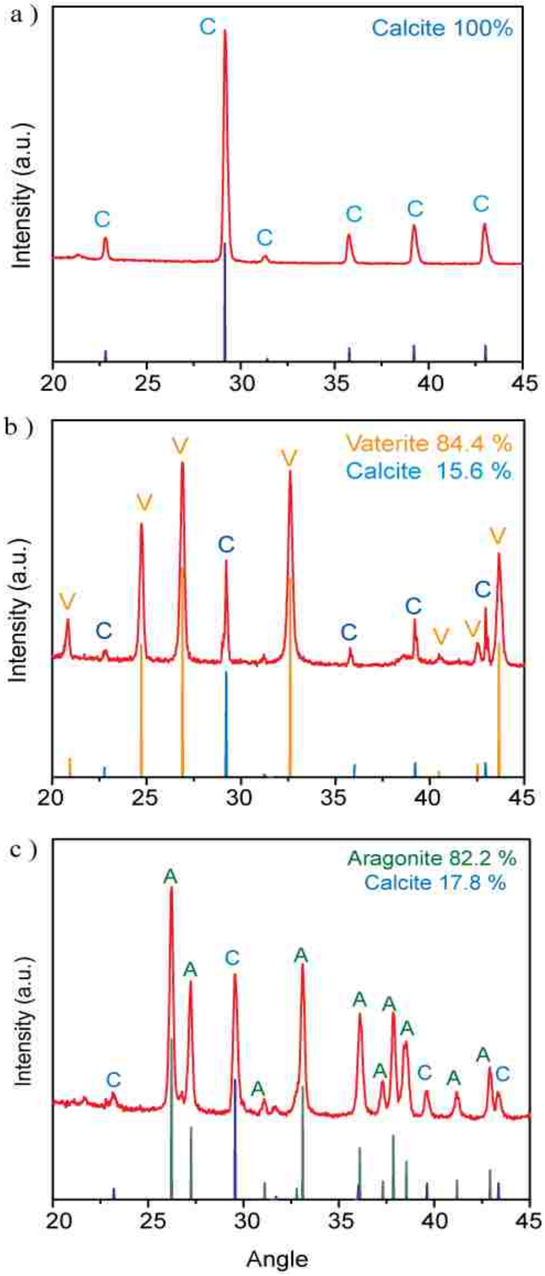

Figure 5: Representative XRD pattern of $CaCO_3$ Formed in a) Calcite crystal structure in the presence of $CaCl_2$, b) Vaterite crystal structure in the presence of Silicatein and $CaCl_2$, c) Aragonite crystal structure in the presence of $MgCl_2$, Silicatein and $CaCl_2$. Identical pattern of Calcite (ICDD:96-901-5762) as a blue line, Vaterite (ICDD:96-901-5899) as a yellow line, and Aragonite (ICDD:96-901-5150) as green line are showed.

Figure 5 presents the crystal structure of three morphologies observed by SEM, Figure 4. X-ray result of the control sample in the range of $20^\circ \leq 2\Theta \leq 45^\circ$ consists the most informative peaks with 29.46° (1 0 4), 36.33° (1 1 0), 39.45° (1 1 3), and 43.19° (2 0 2), corresponding to the pure calcite crystal structure, Figure 5(a). No peak attributed to impure crystals confirms both the presence of one crystal system called trigonal relevant to calcite morphology, and the formed calcite is not decomposed to CaO or CaOH crystals.

However, in the presence of protein, Hexagonal crystal system confirmed by XRD, Figure 5(b), proves the biomineralization of $CaCO_3$ in vaterite morphology more than 84% compared with calcite phase. The predominant vaterite peaks are located in 24.96°, 27.10°, 43.81°. The presence of extra calcite morphology presented in Figure 5b, 29.46° (1 0 4), is due to the stability of vaterite as a least stable $CaCO_3$ crystal; also, vaterite is a kinetic stable intermediate phase that mostly recrystallizes to calcite.

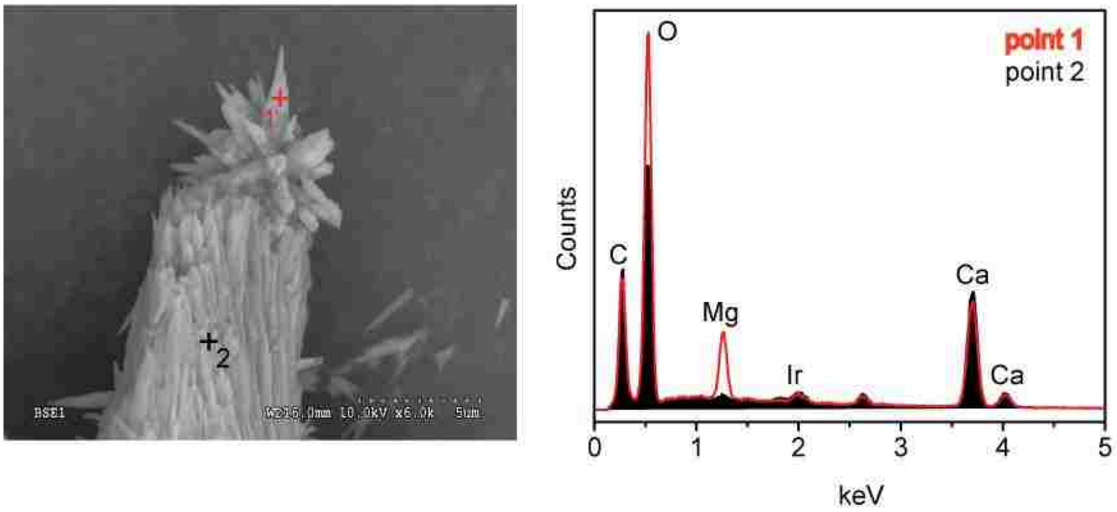

Figure 6: The typical SEM-EDAX mapping spot of precipitated $CaCO_3$ in Aragonite crystal structure to show the distribution of Ca and Mg between spicules and cluster.

Aragonite crystal structure is confirmed by XRD results of the mixture of protein and $MgCl_2$ to $CaCl_2$ solution, in the range of 20°-45°, Figure 5(c). Aragonite is traceable by two dominant peaks at 26.28° (1 1 1) and 27.26° (0 2 1). However, dominant calcite peak is positioned at 29.49° (1 0 4). It can be seen that all crystals that may have Mg^{2+} in the structure such as high-Mg calcite, dolomite $CaMg(CO_3)_2$ and magnesite $MgCO_3$ have the same hexagonal crystal system and they are incorporated into aragonite structure because the Mg^{2+} prefers a six-coordinate geometry (Octahedral geometry) being favorable for aragonite nucleation[44,45]. Also, SEM based EDAX results, Figure 6, shows the presence of Ca and Mg Crystals. The distribution of Mg and Ca between aragonite crystals and cluster polymorph is presented in Figure 6.

3.2.2. Mechanism of Silicatein in aragonite biosynthesis

In the second set of experiments, effects of protein in biomineralization of aragonite crystal structure is observed based on experimental design summarized in table 2.

Table 2: Precursors concentrations and experimental conditions of aragonite biosynthesis. Buffer is 500 mM Imidazole as the last solution in protein purification (IMAC)

	Concentration			**CO_2 flow**	**Time of synthesis**
	$CaCl_2$ (mM)	Silicatein (µM)	$MgCl_2$ (mM)	(ml/min)	hour
1	50	(buffer)[a]	125	100	16
2	50	6.75	125	100	16
3	50	6.75	125	100	4
4	50	6.75	125	100	12
5	50	6.75	125	100	16
6	50	6.75	125	100	24

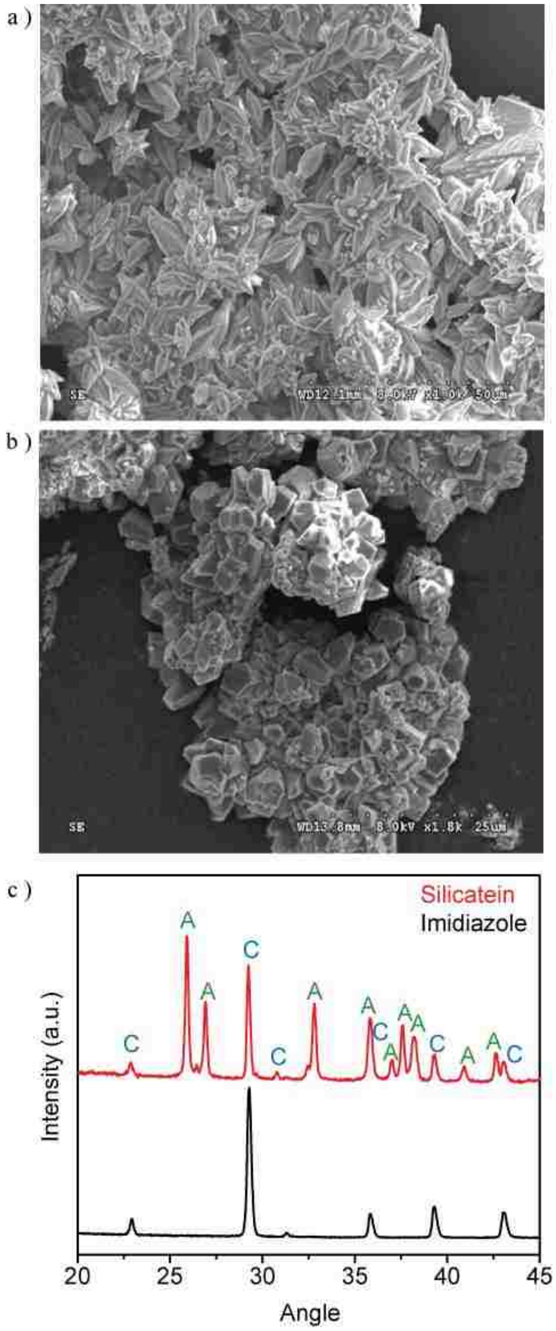

Figure 7: Formation of $CaCO_3$ crystals in buffer in the presence of $MgCl_2$ solution with and without Silicatein. a) Typical SEM image and b) corresponding XRD pattern of $CaCO_3$ in calcite crystal structure in the absent of Silicatein enzyme. c) Typical SEM image and d) corresponding XRD pattern of $CaCO_3$ in Aragonite crystal structure in the presence of Silicatein enzyme.

The effect of protein regard to aragonite morphology synthesis can be seen in Figure 7(a). Lots of aragonite microcrystals formed in the presence of protein and Mg^{2+} ions. However, cubic crystals are formed, Figure 7(b), by the same solution with the same concentration of Mg^{2+} ions that has only the same concentration of Imidazole without the protein. Also, Figure 7(c) shows the XRD results that confirms that the presence of Silicatein can form aragonite crystals. The main functional group of protein, polypeptide as a significant source of amino acids, has an strong affinity with crystal surface locations to incorporate with cluster and control the growth of polymorph in aragonite strucutre[40]. Also, it is reported that the carboxyl group such as Asx, Ser, and Gly amino acid residues, nearly 41 % of protein sequence, bind to Ca^{2+} and surpassing the growth of calcite that is favorable forwarding mechanism of aragonite morphology[46,47]. Additionally, nearly 5 % of protein sequence contributed by Lys and Arg amino acid residues are considered as active sites for interaction with carbonate[40].

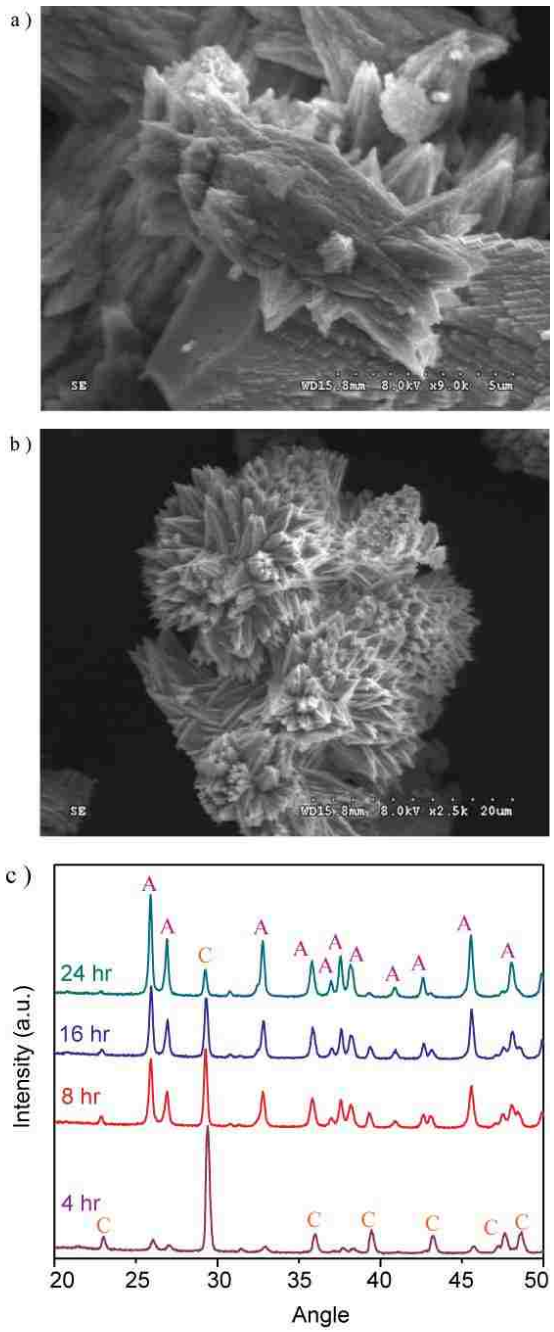

Figure 8: Synthesis of $CaCO_3$ in the combination of Aragonite and calcite crystals as a function of time. a) typical SEM image of a particle after 4 hours of synthesis, b) typical SEM image of particle after 16 hours of synthesis, c) X-ray spectrum of $CaCO_3$ particles at various time, and d) the ratio of aragonite crystal formation as a function of time.

Higher solubility and reactivity of Ca^{2+} compared to Mg^{2+} causes that $CaCl_2$ produces $Ca(OH)_2$ in the solution. Similarly, the formation of $Mg(OH)_2$ happens in the presence of $MgCl_2$. However, $Ca(OH)_2$ dissolved in water firstly to provide favorable conditions of reaction between Ca^{2+} and CO_3^{2-} to form $CaCO_3$ due to its higher solubility in water. Then, $Mg(OH)_2$ is dissolved in water and OH^- reacts with CO_2 to form CO_3^{2-} producing more $CaCO_3$. Both Mg^{2+} and Ca^{2+} have a hexagonal structure, but 0.33 A° is the difference between their radius. In addition, Ca^{2+} in calcite crystals can be substituted with Mg^{2+} to form Mg-Calcite crystals since they both are very interchanged easily[48]. Mg^{2+} can avoid calcite formation through poising the calcite surface growth, which causes an observable switch in crystal structure from calcite to aragonite at high ratios of Mg:Cl[48].

3.2.3. Improvement in biosynthesis of aragonite crystals structure

Due to biomineralization of aragonite crystal structures, $CaCO_3$ morphology selection, and effect of Silicatein in aragonite formation, improvement of aragonite biosynthesis is observed by tuning the ratio of Mg:Ca or increasing the Silciatein concentration summarized in table 3.

As the ratio of Mg:Ca increases, the yield of calcite decreases, while higher aragonite phase is formed, Figure 9(b). At higher concentration of $MgCl_2$, the molarity of Mg^{2+} ionized from $Mg(OH)_2$ increases in the solution as the reaction time goes on, which causes to slow down the dehydration. It can be seen that at lower ratio, no peaks are founded at 26° and 27° relevant to the aragonite morphology, Figure 9(a). However, as the ratio increases, predominant peaks of aragonite morphology located in 26.28° (1 1 1) and 27.26° (0 2 1) appear.

Table 3: Effect of a) tuning Mg:Ca ratio at the constant Silicatein concentration and b) changing Silicatein concentration at constant Mg:Ca ratio on improvement of biosynthesized aragonite. Crystal structure percentage is calculated by GSAS-II simulation.

a)	**Ratio**	**Concentration**	**Particle precipitation**
	Mg/Ca	Silicatein (µM))	Aragonite (%)
1	0.1	6.75	4.1
2	0.5	6.75	11.6
3	1	6.75	23.3
4	1.5	6.75	32.3
5	2	6.75	49.9
6	2.5	6.75	76.7

b)	**Concentration**			**Particle precipitation**
	$CaCl_2$ (mM)	$MgCl_2$ (mM)	Silicatein (µM))	Aragonite (%)
1	50	125	2.25	22.8
2	50	125	4.5	57.6
3	50	125	6.75	78.4
4	50	125	9	92.1

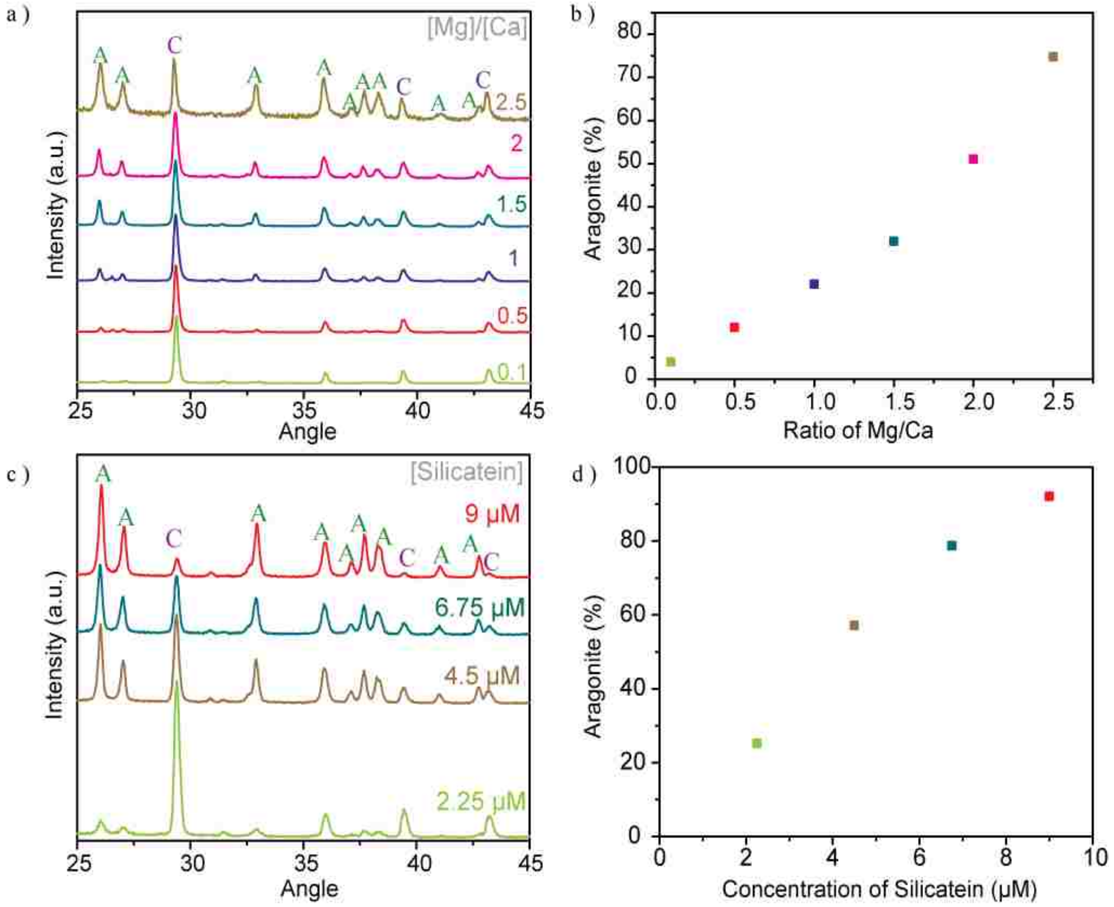

Figure 9: Biomineralization of CaCO3 in the combination of Aragonite and Calcite in the presence of Silicatein and $MgCl_2$ characterized by X-ray spectrum. a and b) the effect of ratio of $CaCl_2/MgCl_2$ concentration, c and d) the effect of Silicatein concentration on the formation of aragonite.

Macromolecule proteins can affect the crystallization of calcite and aragonite by changing the rate of nucleation. Aragonite crystals formation is observable at low kinetics of carbonation, which causes that aragonite typically is synthesized as the last phase crystal produced during the reaction[49]. Mg^{2+} is an ion that can decrease the growth rate of calcite, while the rate of aragonite formation is almost unchanged[50]. Wang and et al found that enrichment of two amino acid, Glu and Asp, can freeze the biomineralization of $CaCO_3$ in aragonite stage[51]. High concentration of Silicatein can provide higher source of Glu and Asp residue in media improving the ratio of aragonite crystals, Figure 9(d).

3.3. Discussion

Calcite is the stable polymorph of $CaCO_3$ crystal under ambient conditions thermodynamically, which naturally forms in the absence of any additives. Diffusion of CO_2 gas flowing through $(NH_4)_2CO_3$ into the solution leads to introduction of both CO_2 and NH_3 into the solution that may form NH_4HCO_3, which causes more alkaline medium being favorable for supersaturation and more precipitation of $CaCO_3$. Generally, the formation of calcite crystals can be explained through five steps from prenucleation to oriented single crystals. As Pouget and et al[51] described, smallest stable agglomerates of $CaCO_3$ formed initially. Then, nucleation of clusters started to form ACC nanoparticles, step 1. Next, the templated surface leads the growth of crystals where many nanoparticles are disturbed in neighborhood to make a local supersaturation, step 2. Then, random oriented crystals are initiated as domain among the ACC that can be still unstable and in equilibrium with ACC phase in step3. In step 4, some dominant orientations start to be stable when the energy of growth surface area is increased by reduction of energy of formation crystal lattice. Finally, the dominant oriented crystal develops to a single crystal, step 5.

Since vaterite is the less stable phase among $CaCO_3$ polymorph, it has the most solubility in water compared with calcite and aragonite. As a result, vaterite has a high tendency to transform into calcite in expose to water. On the other hand, Silicatein has a significant influence on oriented crystal growth since they can manipulate the polymorphic phases and crystal morphology. After nucleation of vaterite, some functional groups of protein such as C=O, HO-, N-H, C-N lead to stabilize this morphology through electrostatic matching, structural and interfacial molecular recognition[52]. In other words, protein can capture the Ca^{2+} by carboxylate group to make a Ca^{2+} local enrichment. When CO_3^{2-} introduces to the system, higher distribution of local calcium ions enrichment may provide a favorable supersaturation conditions for crystal precipitation. This influence on growth rate and changing the morphology of crystal is related to the affinity of silicatein functional groups to the calcium ions.

Metabolism of biosynthesis of $CaCO_3$ in the presence of protein can be categorized into three steps. First, biological metabolism of protein involves a passive route in which CO_2 is dissolved in water for local supersaturation leading to increase the concentration of CO_3^{2-} in the media[53]. Second, the nucleation of carbonation starts on active sites of cell walls by ion exchange through cell membrane. The mechanism of ion exchange is depended on the negative charged functional groups of protein that can capture Ca^{2+} cations[54]. Finally, the functional groups of silicatein play the role of either a biopolymer trapping Ca^{+2} in changing the polymorph of $CaCO_3$ or a growth modifier controlling the crystallization[55]. Low hydrophobic content, polar-charged amino acids and Gly residues of silicatein affect significantly the growth crystal control during biomineralization[27].

Sun and et al predict that calcite needs higher bulk driving force than aragonite to start nucleation. Additionally, when Mg^{2+} incorporate into calcite lattice, the surface energy and solubility increases, which leads to slower calcite nucleation rate by many orders of magnitude[56]. Calcite is the predominant crystals at initial time of the reaction. while the carbonation reaction time progresses, higher amount of Mg^{2+} is dissolved in the solution to form aragonite crystals. It can be considered that inhabitation of calcite nucleation in the presence of Mg^{2+} ions is occurred because of smaller dimension, higher charge density, and greater hydration energy of Mg^{2+}. Hence, the transition of crystal growth from calcite to aragonite happened as dehydration of Mg^{2+} occured[57], which causes that the growth kinetics of calcite decreases compared to the growth of aragonite[58,59].

3.4. Conclusion

In summary, Silicatein α has been demonstrated the role of catalyzing and templating in direct biomineralization route of vaterite and aragonite crystallization. This green synthesis approach due to aqueous-based, room temperature synthesis route, can control the morphology and crystallite of various $CaCO_3$ crystal structures under aerobic conditions. The resulting data shows the changes in shape and crystal structure of $CaCO_3$ from calcite to aragonite as a function of time in the presence of Silicatein, when Mg^{2+} is introduced to the solution. Increase the ratio of $MgCl_2$:$CaCl_2$ or concentration of Silicatein shows improvement in aragonite ratio. Thus, we have conclusively demonstrated an enzymatic low cost, low temperature environmentally synthesis route with easily accessible precursors to change and control the crystallite and morphology of three $CaCO_3$ crystal structures that can be easily implemented for scale-up industry.

Chapter 4

Single Enzyme Direct Biomineralization of ZnS, $Zn_xCd_{1-x}S$ and $Zn_xCd_{1-x}S$-ZnS Core-Shell Quantum Confined Nanocrystals

4.1. Introduction

Functional inorganic nanomaterials are utilized in an increasingly diverse range of applications. The synthesis of these materials is typically accomplished in the organic phase at elevated temperature with the addition of a reactive chemical precursor[2]. While these conventional approaches enable fine control over nanomaterial composition, crystallinity, size and often shape, and allow us to achieve highly active functional materials, this synthesis methodology inherently leads to significant environmental and thus economic implications for scale-up. In contrast, biological systems mineralize inorganic materials in the aqueous phase under ambient conditions. This has led to a significant interest in developing synthetic biomineralization or bioinspired synthesis routes to generate functional nanomaterials[3,52].

Nanoparticle biomineralization has been observed to occur within a wide range of bacterial biofilms[53], where the particles are bound within the extracellular matrix of the film and would require substantial purification prior to any technological application. Bacterial ZnS biomineralization has been observed to occur naturally at sites contaminated with high levels of Zn[54]. For example, Labrenz and Banfield[55] reported bacteria-induced ZnS precipitation within anaerobic biofilms formed in mine drainage systems. In addition, Gramp *et al* and Bai *et al* have both reported on ZnS biomineralization in a laboratory setting utilizing bacteria isolated from natural environments[56]. In all of these cases, the ZnS is biomineralized under anaerobic conditions and the mineralization process occurs over a period of days or longer. The requirement to (i) purify the nanoparticles from the biofilm bacteria responsible for their synthesis, (ii) use anaerobic processing conditions, and (iii) endure long synthesis times all negatively impact the potential to apply these approaches at an industrial scale.

Perhaps the most widely studied approach to overcome these barriers, while maintaining aqueous processing conditions, is to utilize a bio-derived or bio-inspired small molecule, typically a peptide, to mediate nanoparticle formation upon addition of a reactive precursor to an aqueous solution. This approach has been successfully applied to a wide range of materials including metals, metal chalcogenides and metal oxides[3].

We are pursuing an alternative and more direct approach to biomineralization whereby we isolate, engineer and in a scalable fashion produce a single enzyme that is responsible for the generation of the reactive chemical precursor from an otherwise inert solution and also plays a key role in templating nanomaterial formation[34,35,37,57,58]. We have previously demonstrated the application of a putative cystathionine γ-lyase, smCSE, in the direct biomineralization of CdS[34,35,57], PbS and PbS-CdS core-shell[37] quantum confined nanocrystals. In this work, we demonstrate the activity role of smCSE towards the biomineralization of ZnS, $Zn_xCd_{1-x}S$ and $Zn_xCd_{1-x}S$-ZnS quantum confined nanoparticles.

4.2. Results:

UV-vis absorption spectra and corresponding photoluminescence spectra obtained from solutions of Zn-acetate, L-cysteine and the smCSE enzyme as a function of incubation time are showed in Figure 10a and 10b. A distinct absorption shoulder at 270 nm was observed after 90 min of incubation. This feature became more distinct and intense with time, yielding a clear absorption peak centered at 280 nm after ~300 min of incubation. The position of the absorbance peak is consistent with the proposition that ZnS nanocrystals are being biomineralized by the smCSE enzyme in solution[59,60]. The reported bulk band gap values of ZnS in the cubic sphalerite form and hexagonal wurtzite form are 3.54 eV (350 nm)[61] and 3.94 eV (317 nm)[62], respectively. The lower wavelength, higher band gap, absorption maxima for the biomineralized particles is consistent with the formation of quantum confined ZnS nanocrystals. The corresponding emission peak in Figure 1b shows a large Stoke's shift of ~115 nm, indicative of photoemission from deep surface traps, and is typical of nanocrystals formed at low temperature in the aqueous phase where surface defects can be significant[63]. The fluorescence spectra show decreasing intensity with increasing incubation time, indicative of a gradually decreasing quantum yield (QY). The QY of these as-synthesize pure ZnS nanocrystals was 1.88% for the material formed after 300 min incubation.

These absorbance and fluorescence peaks are not observed for solutions prepared in the absence of any of the primary synthesis ingredients of smCSE, Zn-acetate or L-cysteine, when incubated for 300 min, Figure S17. An absorption shoulder at 279 nm and associated photoluminescence peak at 335 nm for solutions containing the enzyme and L-cysteine without any Zn-acetate are in the range expected for tryptophan within the smCSE protein[64]. It should be noted that these peaks originating from the enzyme in the reference samples do not change with incubation time.

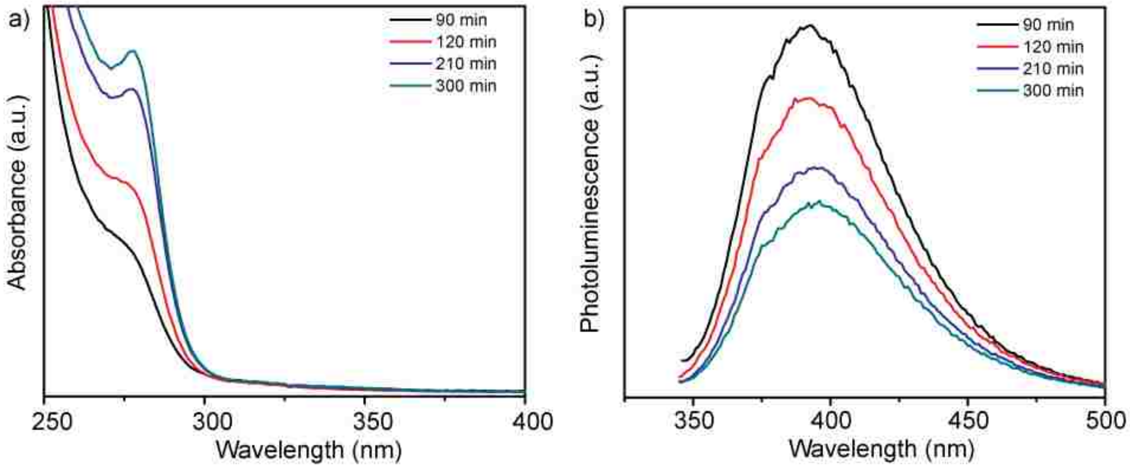

Figure 10:a) UV-vis absorption and b) corresponding fluorescence emission spectra of a buffered (pH=9.0) aqueous solution of Zn-acetate, L-cysteine and smCSE enzyme as a function of incubation time at room temperature. The spectra of solutions incubated in the absence of one or more of these components are provided in Figure S1 for reference.

Direct evidence for the formation of ZnS nanocrystals within the quantum confined size range is provided by HAADF-STEM imaging and XEDS analysis, Figure 11. The HAADF-STEM images show well defined nanoparticles with clear lattice fringes, Figures 11a and 11b. Analysis of the Fast-Fourier Transform (FFT), Figure 11c, derived from the single nanoparticle shown in Figure 11b, gives lattice spacings and inter-planar angles that could be consistent with those expected for either the cubic sphalerite ZnS structure viewed along [112] or the hexagonal wurtzite ZnS structure viewed along [112] or [110], Figure S18.

Particle size analysis of 175 nanoparticles gave a spherical equivalent average diameter of 2.55 ± 0.48 nm, Figure 11d, indicating that the ZnS nanocrystals diameter is close to the excitation Bohr radius[65]. Final confirmation that the nanocrystals are indeed ZnS was provided from STEM-XEDS analysis which showed the presence of both Zn and S in individual particles, Figure 11e. The Ni and Si peaks in this spectrum are artefacts and originate from the Ni-based TEM grid and the Si-based XEDS detector, respectively.

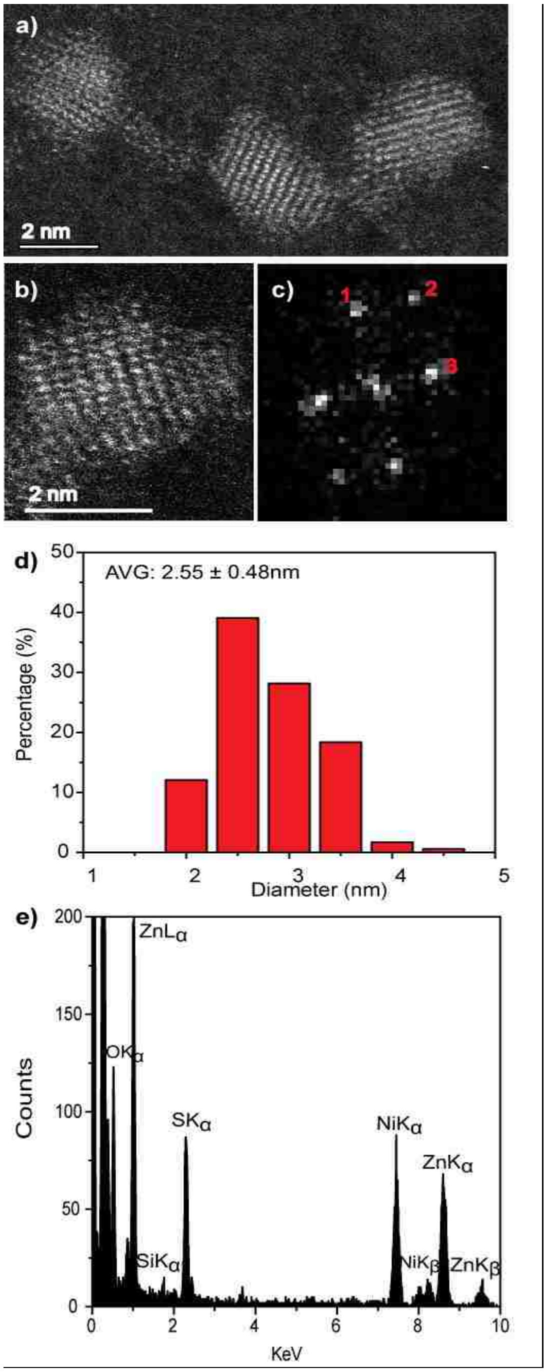

Figure 11: a,b) Representative HAADF-STEM images, c) the corresponding FFT pattern from b, d) particle size distribution and e) single particle STEM-XEDS spectrum of biomineralized ZnS nanocrystals.

We have previously reported that smCSE is active towards biomineralization of analogous CdS quantum confined nanocrystals from Cd acetate containing solutions[34]. Intriguingly, incubation of smCSE in a mixture of Cd and Zn acetate for 3 h leads to material with absorption and photoluminescence spectra peaks between those expected for the pure CdS and ZnS nanocrystals, Figure 12. This is consistent with the formation of $Zn_xCd_{1-x}S$ alloy nanocrystals where the band gap will lie between that of CdS and ZnS[66]. For example, the absorption peak for the $Zn_xCd_{1-x}S$ preparation shown in Figure 12 (with nominal x = 0.8) is at 335 nm, which lies between the 280 nm and 395 nm peaks of the pure ZnS and CdS nanocrystals, respectively. Similarly, the photoluminescence peak from the same sample lies at 450nm, again lying between the 390nm and 530nm peaks of the corresponding ZnS and CdS nanocrystals. SEM-based EDX analysis of the centrifuged and dried agglomerate powder from this sample gave an overall composition of $Zn_{0.73}Cd_{0.27}S$, Figure S19, which is slightly different from the nominal precursor composition of $Zn_{0.80}Cd_{0.20}S$. A Tauc plot analysis of the optical data gives direct band gap values of 2.8, 3.4, and 4.1 eV for the CdS, $Zn_{0.73}Cd_{0.27}S$, and ZnS nanoparticles, respectivlely[67], Figure S20a. The quantum yield of the biomineralized $Zn_{0.73}Cd_{0.27}S$ alloy nanoparticles was 5.21%. For comparison, we have previously reported typical quantum yields of 1.8% for the biomineralized CdS nanocrystals[34].

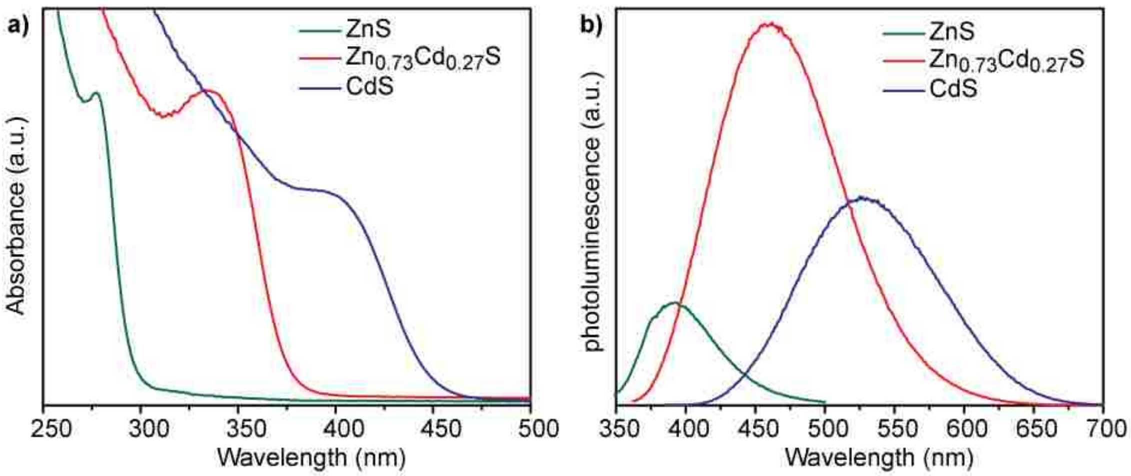

Figure 12: a) UV-vis absorption and b) corresponding fluorescence emission spectra of nanocrystals grown with 1 ml/mol of either Zn acetate (green lines), Cd acetate (blue lines), or a nominal 4:1 ratio of Zn:Cd acetate (red lines). The alloy composition Zn0.73Cd0.27S was determined from XEDS analysis, Figure S3.

As with the pure ZnS nanocrystals, HAADF-STEM imaging demonstrated that the $Zn_{0.73}Cd_{0.27}S$ alloy particles are crystalline, Figures 13a and 13b. Analysis of the FFT pattern, Figure 13c, from a single particle, Figure 13b, demonstrates a good fit with the sphalerite crystal structure viewed along [001] with d-spacing in good agreement with those calculated using a simple Vegard's law approach for $Zn_{0.79}Cd_{0.21}S$, Figure S21. The size distribution, Figure 13d, measured from 183 particles indicated an average spherical equivalent diameter of 2.70 ± 0.44 nm. Final confirmation of alloy formation was provided by STEM-XEDS analysis, Figure 13e, results of an individual particle that demonstrates the co-existence of Cd, Zn and S within a single particle. Quantitative analysis of the XEDS spectrum from this individual particle yielded a composition of $Zn_{0.79}Cd_{0.21}S$, which is in reasonable agreement with the $Zn_{0.73}Cd_{0.27}S$ average composition obtained from SEM based XEDS analysis of a much larger number of particles.

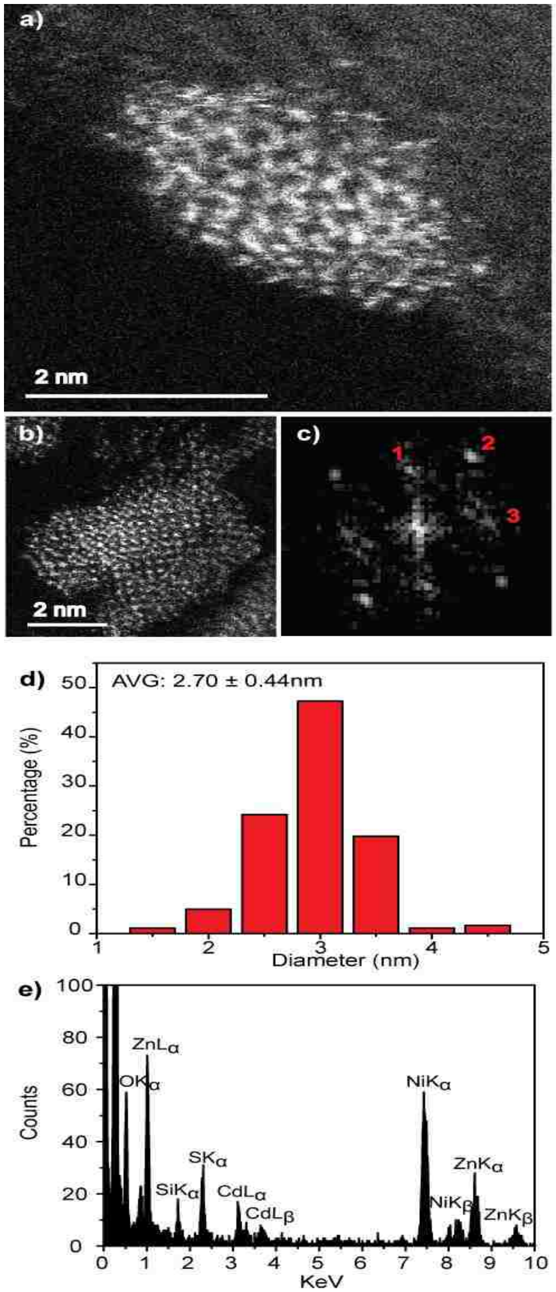

Figure 13: a,b) Representative HAADF-STEM images, c) corresponding FFT pattern from b, d) particle size distribution and e) individual particle STEM-XEDS spectrum for $Zn_{0.73}Cd_{0.27}S$ nanocrystals biomineralized from a precursor solution containing a nominal 4:1 Zn:Cd molar ratio.

We also investigated if the alloy composition in the biomineralized $Zn_xCd_{1-x}S$ particles can be tuned by varying the Zn:Cd ratio in the precursor solutions. Figure 14 shows the optical properties of nanocrystals obtained from solutions having nominal 1:1, 2:1, 3:1, 4:1 Zn:Cd ratios following 3 h incubation. All of the materials show clear absorption peaks with peak positions that progressively blue-shift from 385 to 335 nm with increasing Zn content, which is in agreement with the expected trend for $Zn_xCd_{1-x}S$ alloy particles that are getting more Zn-rich. The corresponding photoluminescence spectra show a similar trend, with peak position shifting from 528 to 478 nm as the nominal Zn:Cd ratio varies from 1:1 to 4:1. SEM based XEDS analysis of the dried nanocrystal aggregates yielded average compositions of $Zn_{0.38}Cd_{0.62}S$, $Zn_{0.61}Cd_{0.39}S$, $Zn_{0.65}Cd_{0.35}S$, and $Zn_{0.73}Cd_{0.27}S$, for the nanocrystals biomineralized from precursor solutions with 1:1, 2:1, 3:1, 4:1 Zn:Cd ratios, respectively, Figure S20. Comparison of the relative ratios of absorption to photoluminescence intensities of these other compositions to those for $Zn_{0.73}Cd_{0.27}S$ suggests that the quantum yield of these materials will be similar to or lower than the 5.21% determined for $Zn_{0.73}Cd_{0.27}S$. A Tauc plot analysis, Figure S20b, gave direct band gap values of 2.96, 3.02, 3.19, and 3.40 eV, respectively, for this systematic set of samples, with the band gap increasing as the Zn content in the $Zn_xCd_{1-x}S$ nanocrystals increases[68],[69].

Intriguingly, while the overall composition trend reflective of the increasing Zn content in solution, the SEM-EDX determined compositions of the biomineralized nanocrystals are not the same as the nominal Zn:Cd precursor ratio in solution. This differs from the route involving direct chemical synthesis from a mixed solution where the measured $Zn_xCd_{1-x}S$ alloy composition is a fairly close match to the composition of the precursor solution. For example, direct reaction of Na_2S with a 4:1 Zn:Cd molar ratio of the metal acetates in water produces particles with an average composition of $Zn_{0.80}Cd_{0.20}S$, Figure S22. Note that this chemical precipitation is performed in the presence of L-cysteine such that the only difference between the biomineralization and this approach is the presence and use of the enzyme to create the reactive sulfur species in biomineralization. Any influence of L-cysteine-metal complex formation on nanocrystal composition should be the same for both approaches.

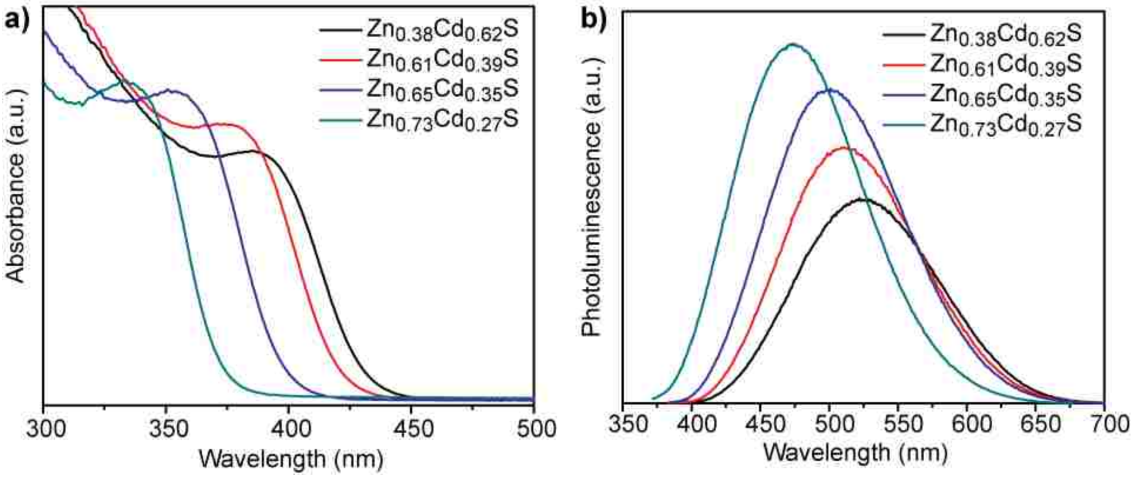

Figure 14: a) UV-vis absorption and b) corresponding fluorescence emission spectra of $Zn_xCd_{1-x}S$ QDs of various compositions synthesized using different molar ratios of zinc acetate to cadmium acetate.

ZnS shells are commonly grown onto CdS and $Zn_xCd_{1-x}S$ alloy core materials to improve photoluminescent quantum yield[70]. The higher band gap of ZnS relative to the core aids in confining the exciton in the core while the small lattice mismatch between the materials aids in shell formation[71]. Figure 14a and 14b show the change in absorbance and photoluminescence spectra upon secondary incubation of as-synthesized core shell $Zn_{0.73}Cd_{0.27}S$ particles in a solution of Zn acetate, L-cysteine and smCSE enzyme. The measured red-shift in both the absorption and photoluminescence peaks, the 12nm reduction in Stoke's shift, and the increase in photoluminescence intensity are all consistent with the formation of a ZnS on the surface of the core particles[71]. The measured quantum yield of these $Zn_{0.73}Cd_{0.27}S$-ZnS particles increases to 7.02%, in contrast with the 5.21% determined for the $Zn_{0.73}Cd_{0.27}S$ core particles.

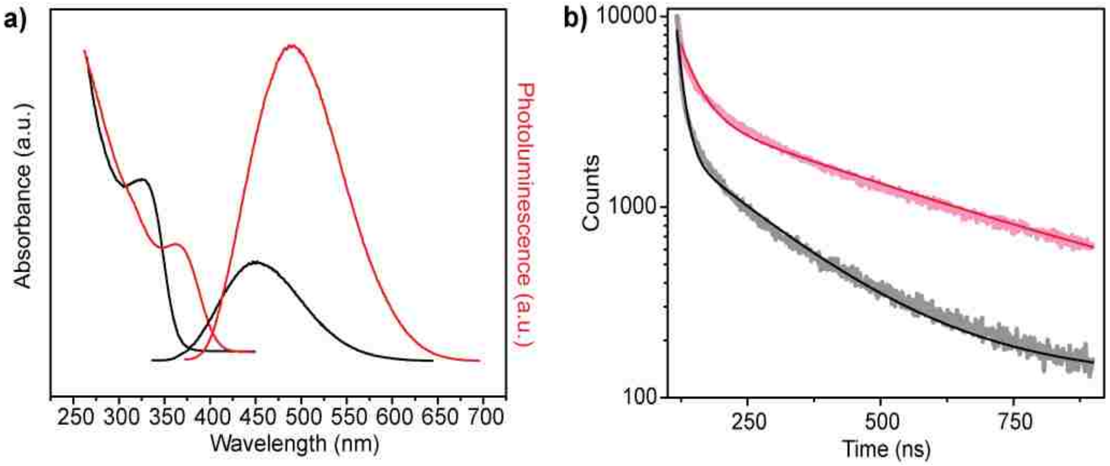

Figure 15: a) Absorption and corresponding photoluminescence spectra and b) fluorescence decay-time measurements of $Zn_{0.73}Cd_{0.27}S$ core (black) and $Zn_{0.73}Cd_{0.27}S$-ZnS (red) biomineralized nanocrystals.

Analysis of the photoluminescence decay profile shown in Figure 15b provides further evidence for the formation of a passivating ZnS shell on the $Zn_{0.73}Cd_{0.27}S$ core. The double-exponential fitting procedure we and others have employed assigns the faster decay step, τ_1, to non-radiative decay and the slower decay step, τ_2, to the radiative process[72],[73]. The radiative recombination rate of the $Zn_{0.73}Cd_{0.27}S$-ZnS nanocrystals was determined to be 97.6 ns, which is significantly longer than the 40.9 ns measured for the bare $Zn_{0.73}Cd_{0.27}S$ core crystals, Table 4.

Table 4: Photoluminescence (PL) lifetime decay measurements of core-only $Zn_{0.73}Cd_{0.27}S$ and $Zn_{0.73}Cd_{0.27}S$-ZnS samples in solution.

Sample	B_1 (%)	τ_1 (ns)	B_2 (%)	τ_2 (ns)	$\bar{\tau}$ (ns)[a]
$Zn_{0.73}Cd_{0.27}S$	155	2.7	35	40.9	9.7
$Zn_{0.73}Cd_{0.27}S$-ZnS	67.1	7.8	34.8	97.6	38.8

[a]: $\bar{\tau}$ (average life time) = ${\sum B_i.\tau_i}/{\sum B_i}$

$$y = B_1.\exp(-{t}/{\tau_1}) + B_2.\exp(-{t}/{\tau_2})$$

An electron microscopy analysis of the $Zn_{0.73}Cd_{0.27}S$-ZnS particles is presented in Figure 16, with representative HAADF-STEM images shown in Figure 16a and b. Further analysis of lattice fringes presents in the individual particle shown in Figure 16b and its corresponding FFT transform, Figure 16c, gives a reasonable fit to the wurtzite structure viewed along [212] with fringe spacings and interplanar angles in good agreement with those predicted for a $Zn_{0.73}Cd_{0.27}S$ alloy as predicted from a Vegard's law estimate, Figure S23. The presence of a ZnS shell is also indicated suggested by a measurable increase in average size to 3.02 nm, Figure 16d, from the initial 2.70 nm value found for the core-only particles. Taking the ZnS wurtzite c lattice parameter as c 0.626 nm[74], this increase in diameter corresponds to an approximate sub-monolayer ZnS decoration on the core surface. Thus, we must be cautious about the use of the word shell to describe what is more accurately described as a surface enrichment of ZnS. STEM-XEDS compositional analysis, Figure 16e, of an isolated $Zn_{0.73}Cd_{0.27}S$-ZnS single particle demonstrates the co-existence of Cd, Zn, and S in the nanocrystal. Thus, while a clear shell is not directly discernable in the HAADF-STEM images of the $Zn_{0.73}Cd_{0.27}S$-ZnS particles due to the small size of the particles and the thin incomplete shell coverage, the increase in quantum yield, average diameter, and photoluminescence time are all consistent with the formation of some sort of passivating surface layer.

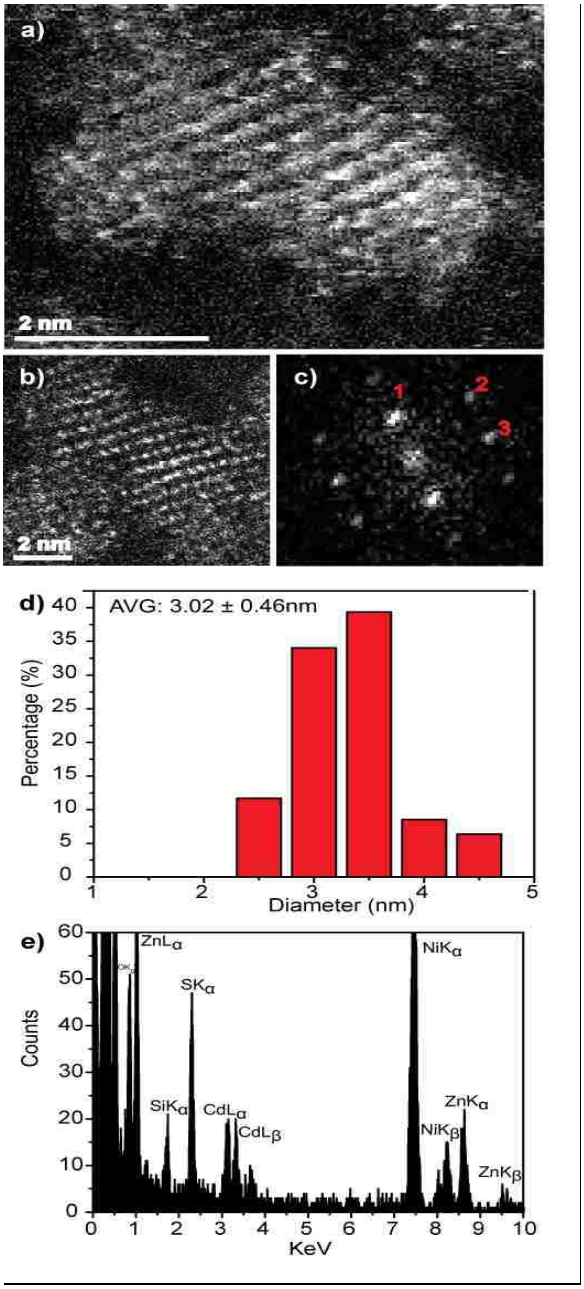

Figure 16: a,b) Representative HAADF-STEM images of $Zn_{0.73}Cd_{0.21}S$-ZnS QDs, c) corresponding FFT from the particle in b that can be fitted to the wurtzite structure viewed along the $[21\bar{2}]$ projection, Figure S23, d) corresponding spherical equivalent nanocrystal size distribution from measurements on over 100 particles and e) XEDS spectrum demonstrating the co-existence of Zn, Cd and S in an individual nanocrystal.

4.3. Discussion:

The optical properties of the biomineralized ZnS nanocrystals produced in this study are in good agreement with those reported for chemically synthesized ZnS particles of the same size. For example, Ghatak et al report an absorbance peak at 287 nm for particles with a calculated mean diameter of 2.3 nm, which is within the error limits of our 2.55 ± 0.48 nm ZnS particles which display an absorbance peak at 280 nm[75]. Similarly, Li et al reported an absorption peak at 276 nm for ZnS particles with crystallite size of 2.62 nm, as calculated by a Scherrer analysis of their XRD data[76]. The growth in intensity and slight red-shifting of this absorbance peak with increasing incubation time in our biomineralization process is indicative of a gradually increasing average particle size, which is similar to the trend observed in our previous reports for CdS biomineralization[34].

Manzoor et al have ascribed the photoluminescence displayed by ZnS nanocrystals to arise primarily from transitions between S vacancies acting as electron traps below the conduction band, and Zn vacancies or surface states[77]. The central luminescence peak position of 434 nm reported by Manzoor et al is higher than the 395nm peak position noted for our materials. This discrepancy is unlikely to be due to differences in the degree of quantum confinement as the materials from the Manzoor paper had a smaller average crystallite size (2 nm) than those in this work, (2.55 nm), which would be expected to lead to an increase in band gap. Tang et al synthesized ZnS nanocrystals with a 2.9 nm average crystallite size which displayed dual photoluminescence peaks at 385 and 405 nm due to (i) interaction of the capping agent and surface Zn^{2+} and (ii) recombination of electrons at surface S vacancy traps with holes at surface Zn vacancies, respectively[78]. By way of contrast, Lu et al ascribed a similar photoluminescence peak at 391 nm, albeit for ZnS crystallites larger than 3.6 nm, to a direct recombination event from the conduction band to Zn vacancies with an additional peak at 422 nm assigned to recombination from a S vacancy to a hole in the valence band[79]. The involvement of a surface state in the observed photoluminescence is in good agreement with our data, where the peak position is found to be essentially independent of incubation time. These observations on our biomineralized materials are in good agreement with the work of Tang et al who also reported a similar lack of shift in photoluminescence peak position with increasing ZnS crystallite size[78].

Co-incubation of Zn acetate and Cd acetate causes a decrease in band gap in the resultant $Zn_xCd_{1-x}S$ nanoparticles relative to the pure ZnS nanocrystals (Figure 3), exhibiting a band gap value between that of pure CdS and ZnS, indicative of biomineralization of crystalline alloy nanocrystals[80]. This alloy formation is confirmed by the single particle STEM-XEDS data. The composition of these alloy nanocrystals can be controlled to some extent through manipulation of the Zn:Cd precursor ratio in the original reaction solution. Thus, smCSE is in principle capable of catalyzing the formation of $Zn_xCd_{1-x}S$ nanocrystals with compositions spanning the entire range from ZnS to CdS. The calculated quantum yield of 5.21% for our biomineralized $Zn_{0.73}Cd_{0.27}S$ material is similar to that reported for aqueous phase chemically synthesized $Zn_xCd_{1-x}S$ materials[81].

The growth of a wider band gap ZnS shell on the surface of $Zn_xCd_{1-x}S$ alloy core nanocrystals leads to surface passivation and an associated increase in both quantum yield and exciton lifetime. Unfortunately, we are unable to form a thick shell on the core materials purely via secondary biomineralization of ZnS. The relatively thin shell layer and the lack of mass-contrast between Cd and Zn prohibits direct imaging of the ZnS outer layer. Indirect evidence for shell growth, rather than Zn substitution to increase the Zn fraction in the $Zn_xCd_{1-x}S$ alloy core, comes from the observed increase in quantum yield, average particle diameter, and red-shift in both absorbance and photoluminescence peaks. A blue-shift in the opposite direction would be expected if the Zn content of the core were simply increasing, as is frequently reported[82,83] and demonstrated by us in Figure 16.

The biomineralization mechanism in play here is based on the enzymatic turnover of the sulfur containing amino acid L-cysteine to form H_2S, NH_3 and pyruvate in solution.

smCSE is a member of the cystathionine γ-lyase class of enzymes that are widely reported as active for this reaction[84,85]. This H_2S then goes on to react with the metal cations in solution to form, in this case, ZnS, CdS or $Zn_xCd_{1-x}S$. The development of this enzymatic biomineralization approach, with reference to CdS biomineralization, is discussed in a previous publication[58]. The same mechanism of biomineralization of smCSE is realized in our previous works to react with other metal cations and synthesize nanocrystals such as PbS[14], $CulnS_2$ and $(CuInZn)S_2$[86]. However, simply adding H_2S, or more easily Na_2S, to an aqueous solution of metal cations leads to the formation of bulk material rather than nanocrystals. Nanocrystal formation requires a templating agent to arrest growth. While L-cysteine can play a role as a capping agent, we have previously demonstrated a propensity for the smCSE enzyme itself to also template nanocrystal growth[34].

A more active role for the enzyme in the formation of the $Zn_xCd_{1-x}S$ nanocrystals reported in this study is supported by the finding that the alloy nanocrystal compositions are not identical to the ratio of precursors in solution. This is in contrast to the result obtained upon direct chemical precipitation via Na_2S, even in the presence of L-cysteine, where the $Zn_xCd_{1-x}S$ alloy composition is much closer to that of the precursor solution, Figure S19. That is, the mechanism of nanocrystal formation is more complex than the indiscriminate precipitation of metal sulfides from solution that typically occurs upon direct precipitation of metal sulfides[87]. Developing a deeper understanding of this additional active role of the enzyme in mediating particle synthesis is a focus of ongoing work.

4.4. Conclusions

The smCSE enzyme has been demonstrated to be active for the direct co-biomineralization of ZnS and CdS to form quantum confined $Zn_xCd_{1-x}S$ nanocrystals in aqueous solution at room temperature under aerobic conditions. The composition of the resulting $Zn_xCd_{1-x}S$ alloy nanocrystals can be tuned through adjusting the ratio of cadmium acetate and zinc acetate precursors in solution. However, in contrast to direct chemical precipitation of an alloy material, the ratio of Zn:Cd in the nanocrystals is not the same as the precursor solution indicating an additional role for the enzyme in controlling the particle composition. Sequential biomineralization of ZnS on a $Zn_xCd_{1-x}S$ nanocrystal enables the formation of ZnS surface layer on the nanocrystals to improve quantum yield.

4.5. Supplementary data

The following data are supplementary information presented in 4.2 section:

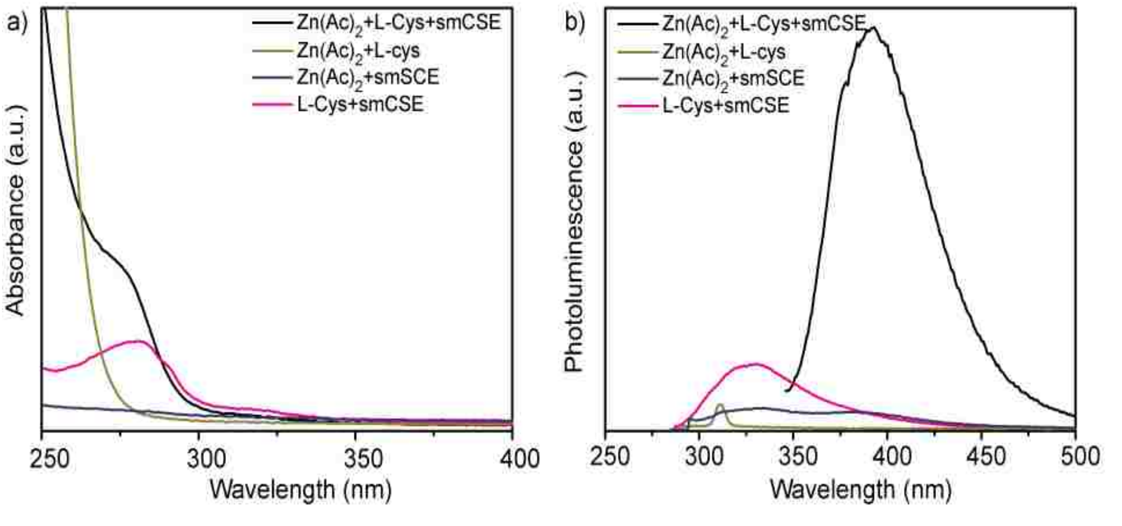

Figure 17**:** a) UV-vis absorption and b) corresponding fluorescence emission spectra of buffered (pH=9.0) solutions containing various combinations of Zn acetate ($Zn(Ac)_2$), L-cysteine (L-Cys), the smCSE enzyme incubated for 90 min at room temperature. Note that all three components are required to obtain absorbance and photoluminescence consistent with ZnS formation. The absorbance and photoluminescence peaks for the L-Cys+smCSE sample originate from the enzyme.

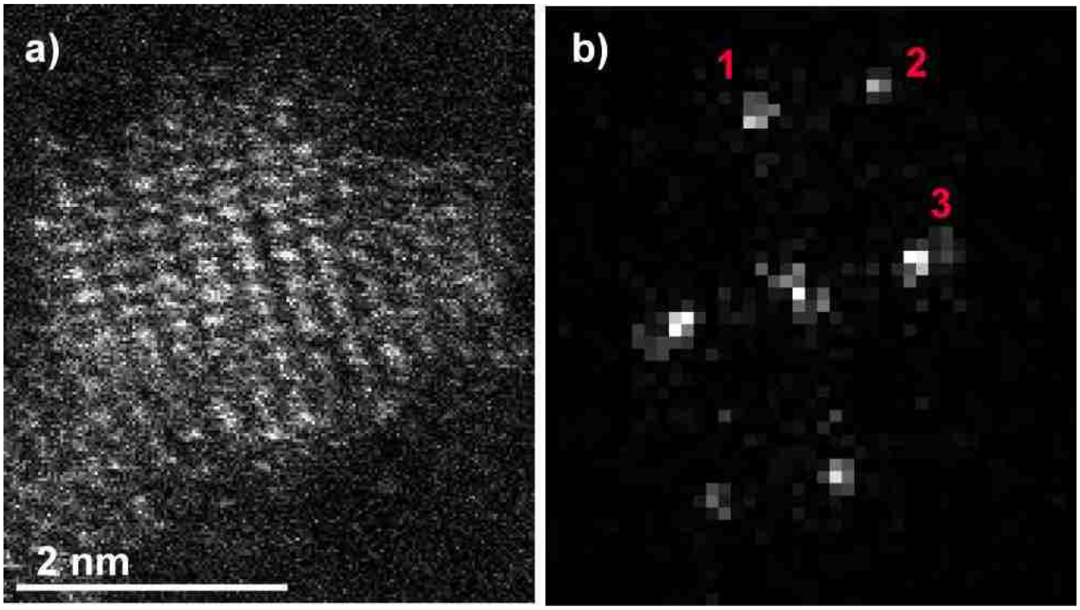

c)	Measurement	Sphalerite ZnS [11$\bar{2}$]	Wurtzite ZnS [1$\bar{1}$0]	Wurtzite ZnS [1$\bar{1}\bar{2}$]
Plane 1	d=2.02 Å	1.91 Å (2$\bar{2}$0)	1.91 Å (110)	1.91 Å (110)
Plane 2	d=1.66 Å	1.63 Å (3$\bar{1}$1)	1.62 Å (112)	1.59 Å (201)
Plane 3	d=2.93 Å	3.12 Å (111)	3.10 Å (002)	2.91 Å (1$\bar{1}$1)
<1,2>	32.8°	31.5°	31.6°	33.2°
<2,3>	54.0°	58.5°	58.4°	56.8°
<3,1>	86.8°	90.0°	90.0°	90.0°

Figure 18**:** Lattice fitting of the ZnS nanocrystal shown in Figure 11b; a) HAADF-STEM image, b) Corresponding FFT image and c) table of measured lattice spacings and interplanar angles compared with ideal values for sphalerite ZnS viewed along [11$\bar{2}$] and wurtzite ZnS viewed along [1$\bar{1}$0] and [1$\bar{1}\bar{2}$].

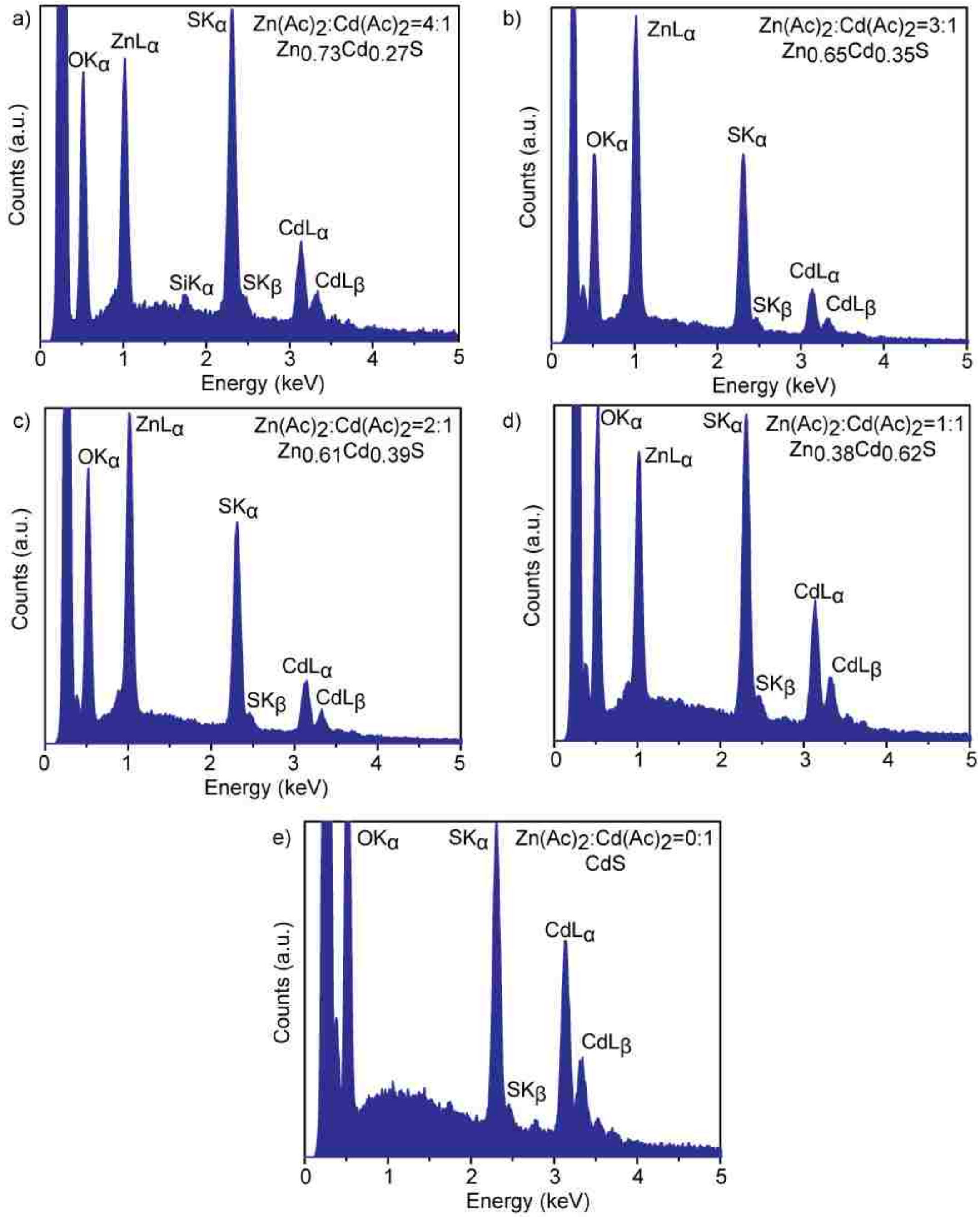

Figure 19**:** SEM-XEDS spectra and calculated mean compositions of $Zn_xCd_{1-x}S$ nanocrystals synthesized with varying ratios of zinc acetate ($Zn(Ac)_2$) to cadmium acetate ($Cd(Ac)_2$).

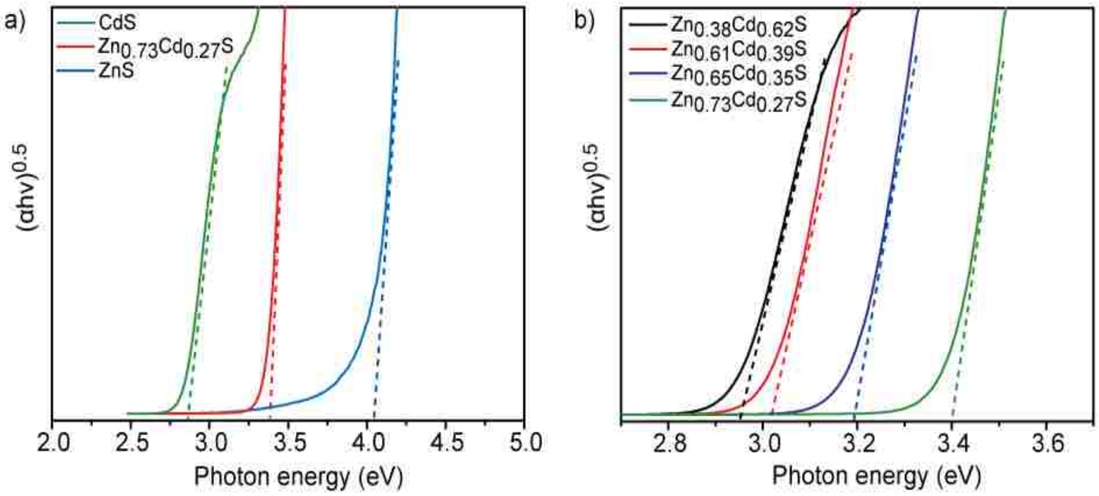

Figure 20**:** Tauc plots of $(\alpha h\nu)^{1/2}$ versus photon energy (hν) showing the band gaps of a) biomineralized ZnS, CdS, and $Zn_{0.73}Cd_{0.27}S$ nanocrystals and b) $Zn_xCd_{1-x}S$ biomineralized nanocrystals of varying composition.

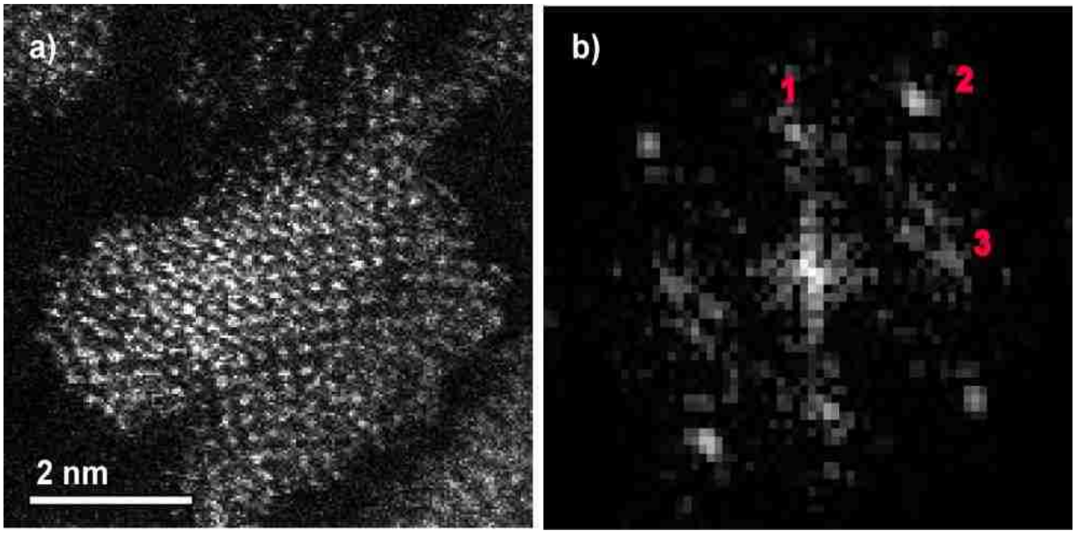

c)	Measurement	Sphalerite ZnS [001]	Calculated Sphalerite $Zn_{0.73}Cd_{0.27}S$ [001]	Sphalerite CdS [001]
Plane 1	d=2.80 Å	2.70 Å (200)	2.75 Å (200)	2.91 Å (200)
Plane 2	d=1.99 Å	1.91 Å (220)	1.94 Å (220)	2.06 Å (220)
Plane 3	d=2.78 Å	2.70 Å (020)	2.75 Å (020)	2.91 Å (020)
<1,2>	43.0°	45.0°	45.0°	45.0°
<2,3>	48.0°	45.0°	45.0°	45.0°
<3,1>	89.0°	90.0°	90.0°	90.0°

Figure 21**:** Lattice fitting of the $Zn_{0.73}Cd_{0.27}S$ nanocrystal shown in Figure 13b; a) HAADF-STEM image, b) corresponding FFT image and c) table of measured lattice spacings and interplanar angles compared with ideal values for the sphalerite structures of ZnS, $Zn_{0.73}Cd_{0.27}S$ and CdS viewed along [001].

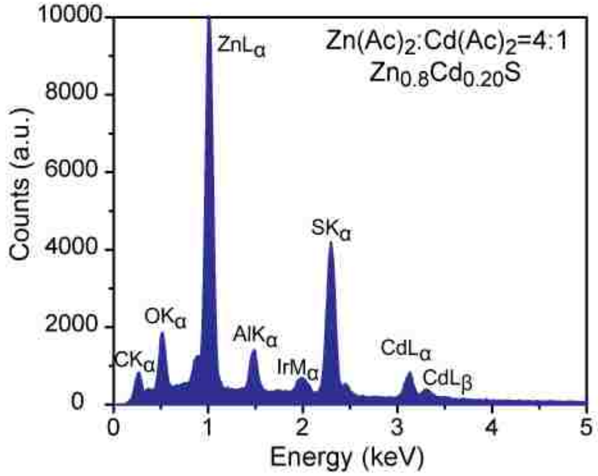

Figure 22**:** SEM-XEDS spectra and calculated mean composition of $Zn_xCd_{1-x}S$ nanocrystals synthesized by addition of Na_2S to an aqueous solution of cadmium acetate and zinc acetate in a 4:1 Zn:Cd molar ratio in the presence of L-cysteine. In contrast to the biomineralized materials, this shows a close correspondence between the actual and nominal nanoparticle compositions.

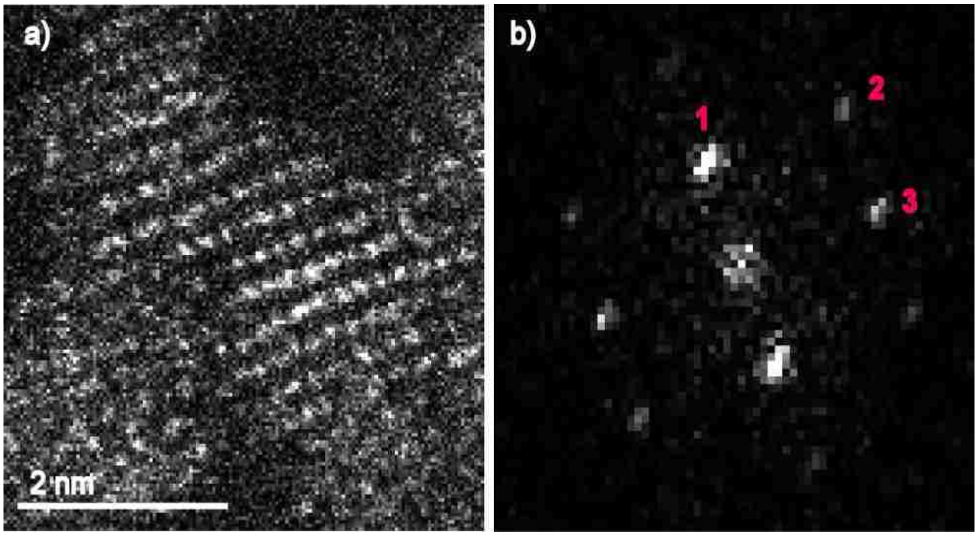

c)	Measurement	Wurtzite ZnS $[21\bar{2}]$	Calculated Wurtzite $Zn_{0.73}Cd_{0.27}S$ $[21\bar{2}]$	Wurtzite CdS $[21\bar{2}]$
Plane 1	d=2.95 Å	2.92 Å (101)	2.96 Å (101)	3.16 Å (101)
Plane 2	d=1.66 Å	1.59 Å (021)	1.62 Å (021)	1.73 Å (021)
Plane 3	d=2.02 Å	1.90 Å (120)	1.94 Å $(1\bar{2}0)$	2.07 Å (120)
<1,2>	54.9°	56.8°	56.8°	56.8°
<2,3>	34.6°	33.2°	33.2°	33.2°
<3,1>	89.5°	90.0°	90.0°	90.0°

Figure 23**:** Lattice fitting of the 3nm diameter $Zn_{0.73}Cd_{0.27}S$-ZnS particle shown in Figure 16b; a) HAADF-STEM image, b) corresponding FFT and c) table of measured lattice spacings and interplanar angles compared with ideal values for wurtzite ZnS, $Zn_{0.73}Cd_{0.27}S$ and CdS viewed along $[21\bar{2}]$.

Chapter 5

Direct single Biomineralization of SnS and CuZnSnS Quantum Dots confined in nanocrystals

5.1. Introduction

Tin sulfide (SnS) is one of the new attracted candidates of archetypal IV-VI groups semiconductors that owned both n-type and p-type conduction activity with an optical band gap of 1.09-1.3 eV which is little smaller than CdS. Tunable band gap, nonpoisonous, relatively inexpensive, and chemically stable properties of SnS lead to potential applications such as absorber layer in solar cells[88], photovoltaics[89], anode material in Li-ion batteries, and semiconductor sensors. Tin sulfide has various components such as SnS, Sn_2S_3, Sn_3S_4, and SnS_2. However, tin sulfide and tin disulfide are the most common structures due to their potential applications and properties. There are few work on synthesis of SnS QDs and its applications such as one-pot hydrothermal SnS nanocrystals at 200 ^oC by Muthuvinayagam et al[90], 4 nm SnS QDs synthesis at room temperature by Prastani et al[91], 4 nm SnS QDs using triethanolamine ligand by Xu et al[92], 5 nm SnS nanoparticles using organic material like octadecene by Tang et al[93], and Deepa and Nagaraju[94] synthesized SnS QDs by SILAR method. Mostly, these traditional methods of synthesis have some limits such as special applications, toxic reagents, organic precursors, and surfactants. Also, some specific reaction conditions such as high temperature, free of water and oxygen are needed. While conventional approaches enable fine control over the composition, crystallinity, size, and shape of nanomaterial to achieve highly active functional materials, these synthesis methodologies inherently lead to environmental and economical implications for scale-up goals.

However, bioinspired synthesis routes or biomineralization has developed nowadays to generate functional inorganic nanomaterials in the aqueous phase under ambient conditions to apply at an industrial scales potentially[3,52]. So far, to the best of our knowledge, there are few reports working on biological formation of SnS nanoparticles even though they use big molecules like bacteria[95] that requires further preparations, purifications, and longer synthesis time. To overcome these barriers, small bio-derived molecules, peptide, can approach the formation of nanoparticles upon additional reactive precursors. There are many works that successfully applied this approach to a wide range of materials such metals, metal chalcogenides, and metal oxides[3,58].

CZTS is one of the relative compounds of SnS gained lots of attention since it can be a potential replacement of conventional absorbers in photovoltaic applications due to its band gap. Also, compared with other metals such as In and Ga (to synthesize $CuInGaSe_2$), zinc and tin are non-toxic earth-abundant elements, near optimal direct band gap, and large absorption coefficient[96]. Most of conventional methods of CZTS thin film fabrication such as spray pyrolysis deposition[97], pulsed laser deposition[98], coevaporation[99], and hot injection[100]. However, all of these methods need high temperature procedures at vacuum which could be expensive. SILAR is one the conventional methods of non-vacuum CZTS thin film synthesis at room temperature in which the thickness, compositions, and phase purity can be controlled by growth parameters such as reaction time, deposition cycles, and precursors concentration. However, these room temperature synthesis methods have some issues such as non-uniformity and non-stoichiometric compositions[101].

In this work, we worked on more direct approach to biomineralization whereby we isolate, engineer, and in a scalable fashion produce a single enzyme that is responsible for the generation of the reactive chemical precursor from an inert solution and also plays a key role in templating nanomaterial formation[34,35,37,57,58]. We have previously demonstrated the application of a putative cystathionine γ-lyase, smCSE, in the direct biomineralization of CdS[34,35,57], PbS and PbS-CdS core-shell[37], ZnS and $Cd_xZn_{1-x}S$-ZnS core-shell[102] quantum confined nanocrystals and an engineered form of silicatein for the biomineralization of $CeO_{2-\delta}$ and $Ce_{1-x}Zr_xO_{2-\delta}$ catalytic nanocrystals[58]. In this work, we demonstrate the activity role of smCSE towards the biomineralization of SnS and CuZnSnS quantum confined nanoparticles.

5.2. Results

Optical properties such as UV-vis absorption spectra and corresponding photoluminescence spectra from solutions of tin (II) chloride, L-cysteine and the smCSE enzyme are showed in Figure 24. A distinct absorption shoulder at 350 nm was observed after 6 hrs. of incubation, which confirms that SnS solution has a strong absorption from NIR to UV range due to its perfect orientation[103,104]. The corresponded photoluminescence spectra of SnS nanoparticles with photon excitation at 350 nm, Figure 24a, shows the quality of crystals and presence of impurities. A broad peak centered around 392 nm and a large stock`s shift of 50 nm can be representative of deep level transition from tin vacancies[105].

The first step in adapting our previously demonstrating single enzyme biomineralization step to the formation of CZTS alloys is to confirm that this process can biomineralized tin sulfide nanocrystals. The UV-vis absorption spectra and corresponding photoluminescence spectra from incubated solutions of tin (II) chloride, L-cysteine and the smCSE enzyme are showed in Figure 24a. Both the clear absorption feature beginning at 350 nm and the corresponding photoluminescence at 392 nm (350 nm excitation) observed after 6 hrs incubation are in the range expected for quantum confined SnS nanocrystals[103,104]. The corresponding direct optical band gap of 3.3 eV determined from a Tauc plot of the absorption data, Figure 24b, is higher than bulk SnS value of 1.3 eV[106], again in the range of previous reports for SnS nanocrystals[107] and indicating the blue shift expected due to quantum confinement.

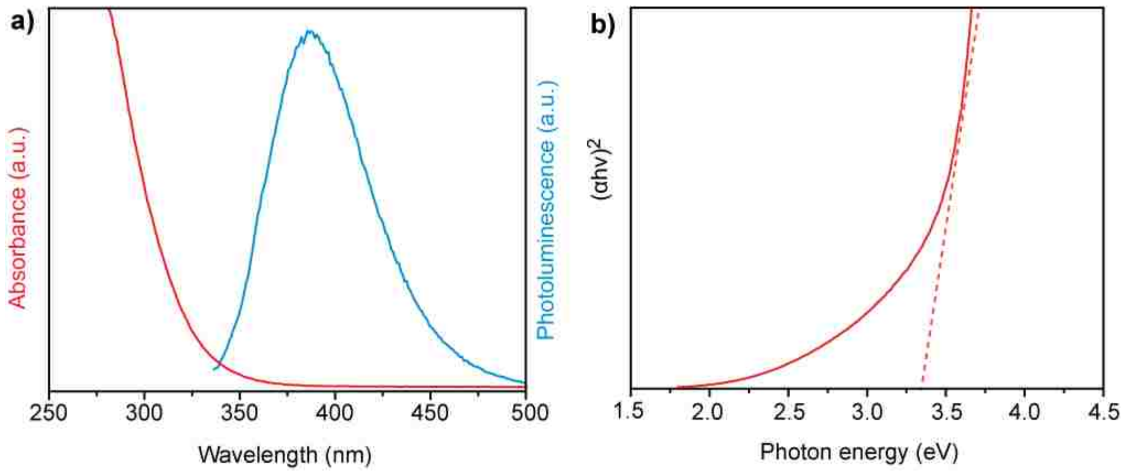

Figure 24: a) UV-vis absorption and corresponding fluorescence emission spectra, b) direct optical band of a buffered (pH=7) aqueous solution of tin (II) chloride, L-cysteine and smCSE enzyme at room temperature

X-ray diffraction (XRD) of the precipitated, centrifuged and dried particles, Figure 25b, is in good agreement with the orthorhombic structure of SnS (space group *Cmcm*, ICDD 96-900-8296 or *Pnma*, ICDD 96-900-8786). The XRD pattern shows peak broadening consistent with the formation of small nanocrystals with no observable impurity peaks. SEM based XEDS analysis indicates a Sn:S ratio of 0.91, again consistent with the formation of SnS and the absence of any significant impurity. The slight excess of sulfur is attributable to the capping ligand, L-cysteine, and to some residual L-cysteine from the biomineralization solution.

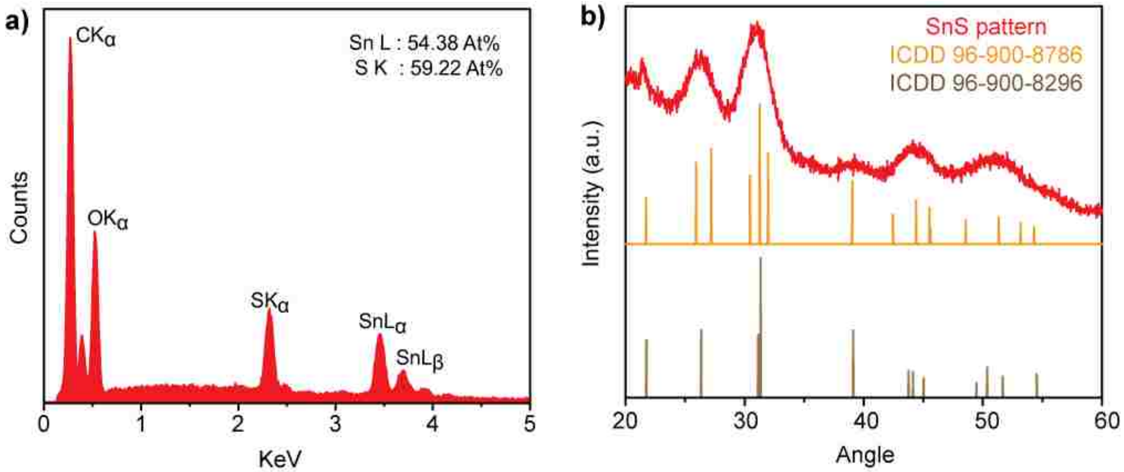

Figure 25: a) Typical SEM-XEDS spectrum of dried particles of SnS particles that are coated with Iridium and b) representative XRD pattern of SnS Formed in Orthorhombic crystal structure. The identical pattern of SnS crystals (ICDD 96-900-8296) is shown.

Direct evidence for the biomineralization of quantum confined SnS nanoparticles is provided by HAADF-STEM imaging and associated analysis. Figure 26a, shows a HAADF-STEM image of a cluster of nanocrystals showing clear lattice fringes and particle diameters of 2.25 nm, substantially below the 7 nm Bohr radius of SnS[108]. Analysis of the lattice fringes of one particle, Figure 26b, by Fast-Fourier Transform (FFT), Figure 26c, indicates inter-planer spacing angles consistent with orthorhombic SnS viewed along the [001] axis, Figure 30. XEDS analysis of a single nanocrystal, Figure 26d, confirms the co-existence of Sn and S in individual particles. Therefore, optical, structural, and chemical analysis results are all consistent with the formation of quantum confined SnS nanocrystals, confirming that our single enzyme biomineralization approach can be extended for SnS biomineralization. As noted above, we have reported the application of our enzymatic direct biomineralization to the formation of CuS and ZnS quantum confined nanocrystals[102,86], and in combination, these results point to the feasibility of CZTS biomineralization.

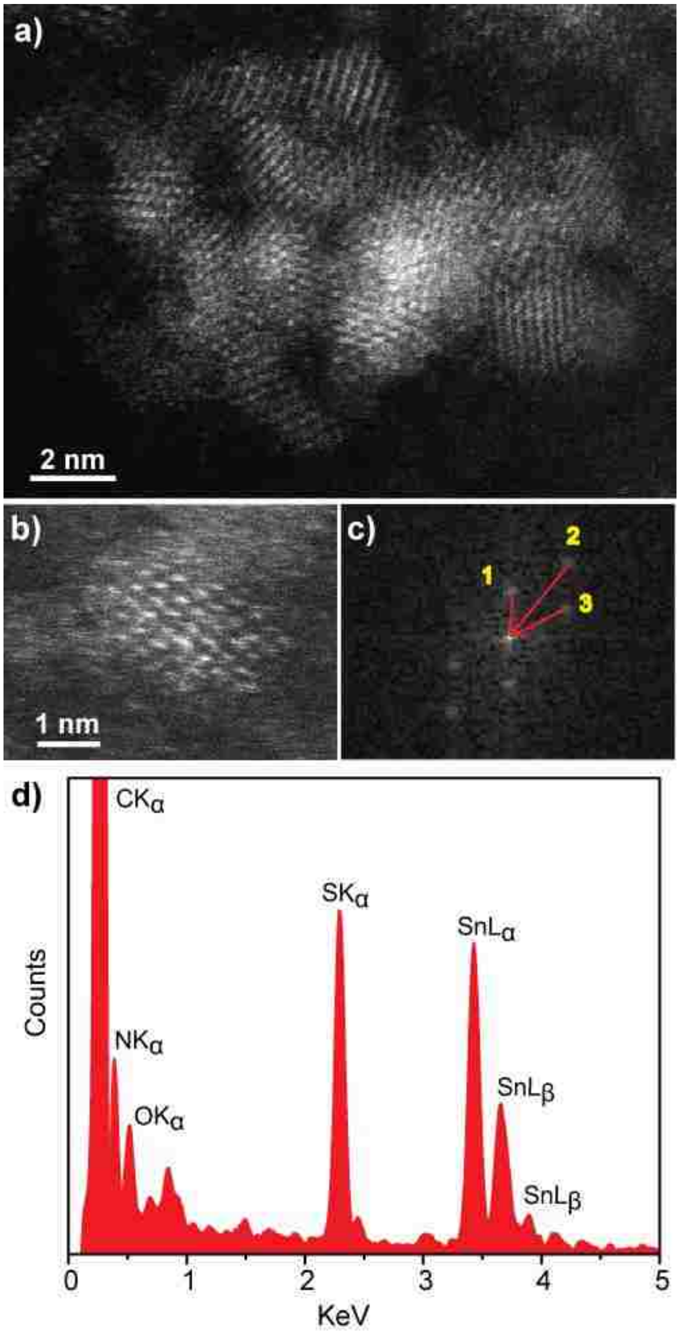

Figure 26: a and b) Representative HAADF-STEM images, c) corresponding lattice fringes of single nanocrystal analyzed by FFT, and d) single particle STEM-XEDS spectrum of biomineralized SnS nanocrystal showing the existence of Sn and S.

Incubation of a buffered mixture of Cu acetate, Zn acetate, tin chloride (Cu:Zn:Sn=1:2:2), L-cysteine, and smCSE for 6 hours yields solutions and nanocrystals with significantly different optical properties to those where only one of the metal precursors is present, Figure 27a. We denote this mixed metal sample as CZTS for clarity in the following prior to providing full compositional details and optimization later in the manuscript. The UV-Vis absorption spectra, Figure 27a, and photoluminescence, Figure 27b, of nominally CuS, SnS, and ZnS are consistent with the previously reported formation of quantum confined nanocrystals of these materials[37,102]. In contrast, the UV-vis spectrum of CZTS shows broad absorption in the visible region with a shoulder at 375 nm, consistent with other works in which quantum confined CZTS nanocrystals are synthesized by more conventional routes[96]. The corresponding photoluminescence of CZTS, Figure 27b, shows a very low intensity, similar to the low intensity observed for CuS, due to the presence of Cu ions in the solution which may quench the fluorescence emission[109]. A Tauc plaot for CZTS, Figure 27c, indicates a direct optical band gap of 2.35 eV, again consistent with prior reports[110].

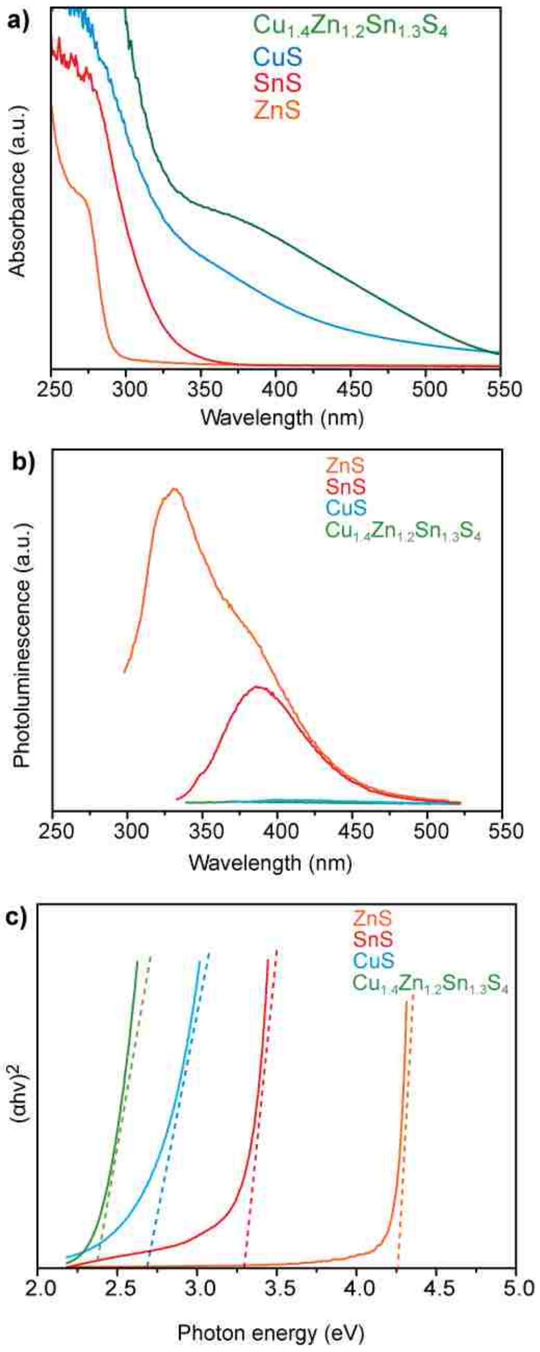

Figure 27: a) UV-vis absorption, b) corresponding fluorescence emission spectra of nanocrystals grown, and c) direct optical band gap of either Zn acetate, Cu acetate, Sn chloride, or nominal ratio of Cu:Zn:Sn=1:2:2 in buffered (pH=7) aqueous solution of L-cysteine and smCSE enzyme at room temperature.

XRD pattern of synthesized CZTS shows, Figure 18a, clear diffraction peaks at $2\theta=$ 28.49, 32.17, 47.37, 56.16 corresponding to the (112), (200), (220), and (312) planes, which matches well with the CZTS in kesterite Tetragonal crystal structure with a=0.54340, b=50.4340, c=10.850, and *I-4* space group (ICCD 96-432-8659). Representative EDX pattern of CZTS nanocrystals indicates the co-existence of Cu, Zn, Sn, and S within a single dried particle, Figure 28b.

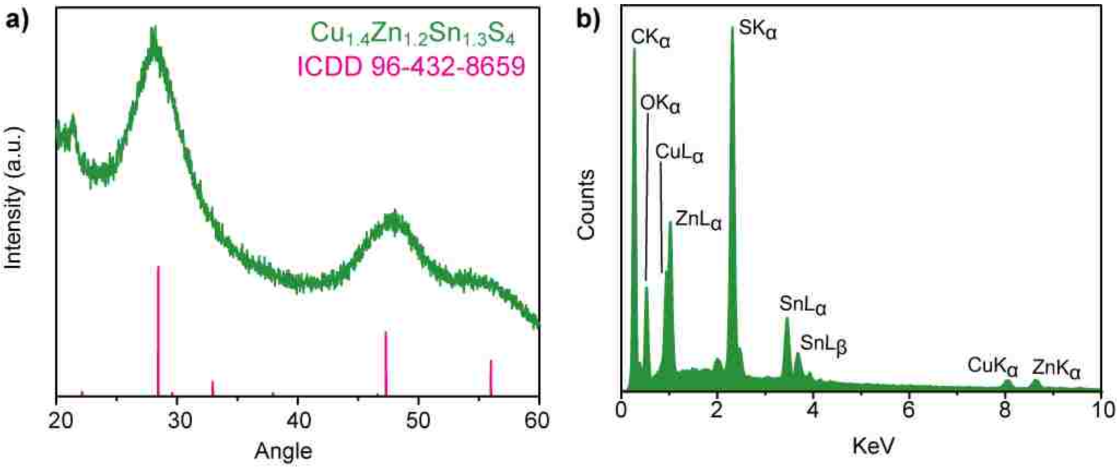

Figure 28: a) representative XRD pattern of CZTS Formed in Tetragonal crystal structure and b) Typical SEM-XEDS spectrum of dried particles of CZTS particles that are coated with Iridium. The identical pattern of CZTS crystals (ICCD 96-432-8659) is shown.

Direct evidence of CZTS alloy nanocrystal formation is provided by HAADF-STEM imaging, Figure 29a, FFT based analysis of the structure of a single particle, Figure 29b, 29c and Figure 31, and STEM-XEDS confirming the presence of Cu, Zn, Sn, and S in a single particle, Figure 29d. The HAADF-STEM imaging shows clearly defined nanocrystals of 3.75 nm in diameter with clear lattice fringes. The FFT analysis confirms the tetragonal structure indicted by the bulk XRD data in Figure 28a.

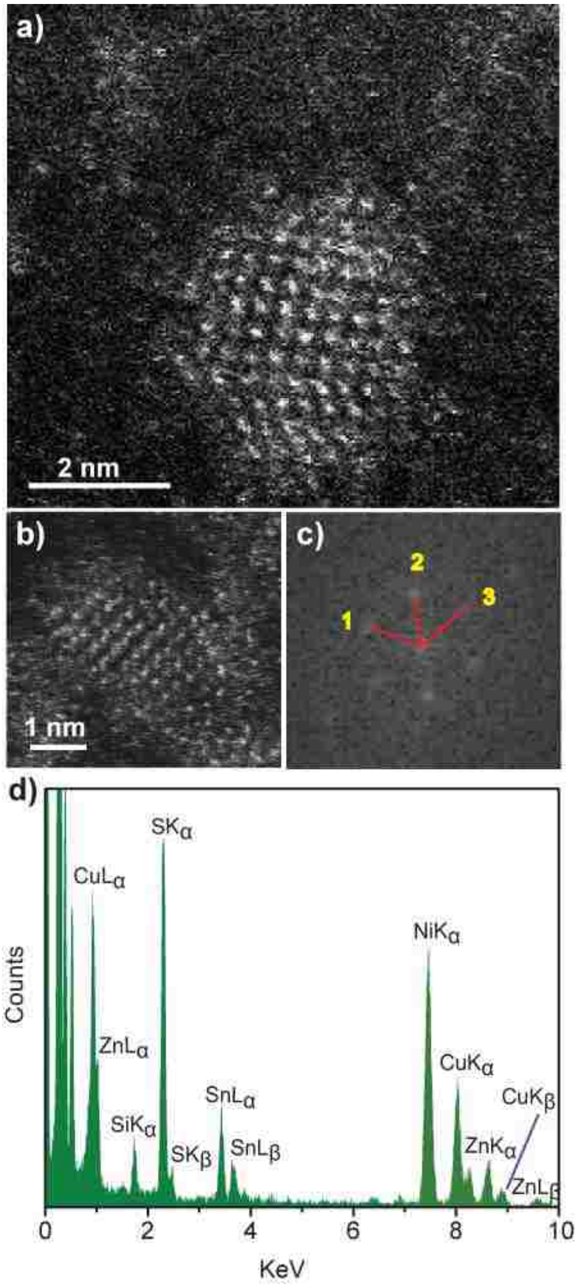

Figure 29: a and b) Representative HAADF-STEM images, c) clear lattice fringes of single nanocrystals analyzed by FFT, and d) single particle STEM-XEDS spectrum of biomineralized Cu1.4Zn1.2Sn1.3S4 nanocrystals showing the coexistence of Cu, Zn, Sn and S in dried Cu1.4Zn1.2Sn1.3S4 particle. The Ni and Si peaks in this spectrum are artefacts and originate from the Ni-based TEM grid and the Si-based XEDS detector, respectively.

5.3. Conclusion

We have demonstrated the biomineralization of SnS and CuZnSnS quantum confined nanocrystals. Single nanocrystals of SnS and CZTS were showed by HRTEM image dark field with clear lattice fringes that is matched well with Orthorhombic and tetragonal crystal structure, respectively. Both XRD and FFT analysis confirm the crystallite of both SnS and CZTS. Also, STEM-XEDS shows the existence of elements in single nanocrystal. Optical band gap of SnS and CZTS demonstrate the potential application of SnS and CZTS QDs as an absorber layer in QD-sensitized solar cell.

5.4. Supplemental Information

The following information is provided for the presented results in section 5.2 as supplementary data:

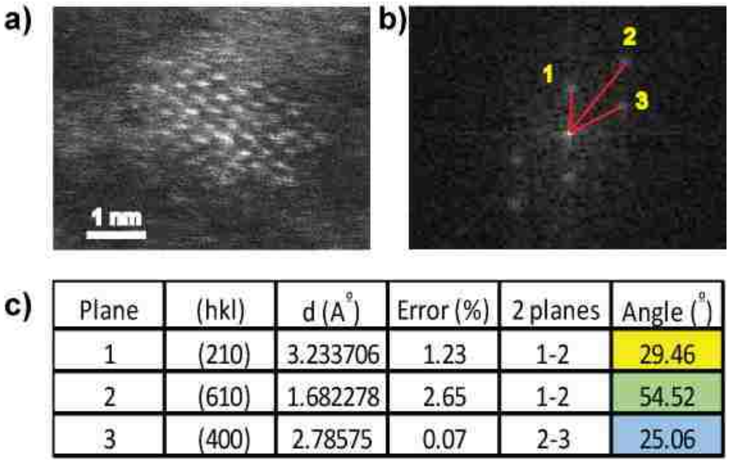

Plane	(hkl)	d (Å)	Error (%)	2 planes	Angle (°)
1	(210)	3.233706	1.23	1-2	29.46
2	(610)	1.682278	2.65	1-2	54.52
3	(400)	2.78575	0.07	2-3	25.06

Figure 30**:** Lattice fitting of SnS nanocrystal shown in Figure 26b; a) HAADF-STEM image, b) corresponding FFT analysis, and c) table of measured lattice spacings and interplanar angles compared with ideal values of Orthorhombic SnS viewed along [001]

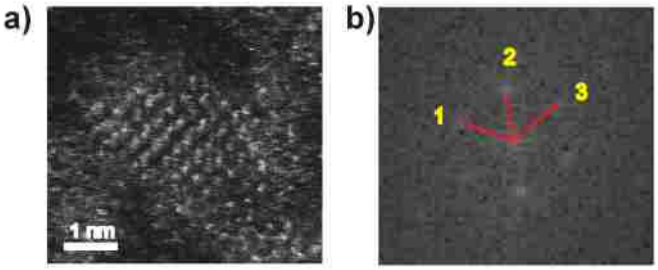

c)

Plane	(hkl)	d (Å)	Error (%)	2 planes	Angle (°)
1	(112)	3.134627	-2.41	1-2	70.49
2	(11-2)	3.134627	2.00	1-3	54.76
3	(004)	2.716000	6.01	2-3	54.76

Figure 31**:** Lattice fitting of CZTS nanocrystal shown in Figure 29b; a) HAADF-STEM image, b) corresponding FFT analysis, and c) table of measured lattice spacings and interplanar angles compared with ideal values of Tetragonal CZTS viewed along [110]

Chapter 6

Improvement in Efficiency of sensitized-solar Cells by CuZnSnS Nanocrystals as an Alloy of SnS QDs

6.1. Introduction

Clean renewable source of energy has been one of the recent global issues for decades[111]. Among various alternative sources of energy, sun’s energy has attracted great interest due its low-cost, easily manufactured, and efficient source of energy. However, a big challenge of efficient devices to convert sunlight into electricity, solar cell, has been still under focused because the cost of existing technologies being too high for scale-up fabrication[112]. Three types of solar cells have engineered in recent years including (i) dye-sensitized solar cell, (ii) bulk heterojunction photovoltaic cell, and (iii) quantum dots solar cell[113]. Previous generations of photovoltaic technologies that were based on single-crystalline semiconductor or semiconductor thin films are classified on solid-state semiconductor technologies, which needs expensive process like high-pressure, high-temperature, and high-cost implements for scale-up goals[112]. Recently, quantum dot-sensitized solar cell (QDSCs) have become promising and attractive technology due to unique properties of quantum dots like high extinction coefficient, broad spectral ranges, easily tunable band gaps, and solution processability[114]. Assembly of QDSCs is based on three components. First, photoanode or working electrode, as a light energy harvester, is composed by large band gap transparent mesoporous TiO_2 or ZnO. Modification of TiO_2 paste with QDs in working electrode is described by different methods such as drop casting, chemical bath, SILAR, electrophoretic deposition, and molecular linker of QD particles to oxide surface[115].

Second component is cathode or counter electrode that is various high-conductive metals or metal sulfides. The importance of finding appropriate material in fabrication of counter electrode is due to providing lower resistance and higher reduction rate. One of the widely used metals in counter electrode has been Pt; however, adsorption of sulfides on its surface causes limitation in QDSC efficiency[116,117]. Au as a high chemically stable metal against sulfides has been considered as an alternative for Pt in CE although it has been an expensive replacement[118,119]. Thus, inexpensive alternative metal with high conductivity and stability includes transition metal sulfides (Cu_xS), conductive polymers, and carbonaceous materials, in which Cu_xS attracts more attention due to catalytic activity of reduction reaction[112]. The last component of QDSCs is electrolyte as a separator of working electrode and counter electrode in which a sulfide/polysulfide redox couple reaction completes the cell[120].

Basic working principle of QDSCs is separation of charge carriers under illumination. Energy of light harvested by working electrode can excite electrons of QDs form valence band (VB) to conduction band (CB). Then, free photoexcited electrons are injected to electron acceptor (TiO_2) and finally transferred out with external circuit. On the other hand, photogenerated holes in valence band of QDs oxidize polysulfide redox couple reaction in electrolyte. Finally, oxidized polysulfide is turned back to the native state by absorption of transferred photoelectron from working electrode through the external circuit. Thus, completing the circuit of separation of electrons and holes of QDs and recombination of separated carriers in electrolyte can generated current through the external circuit. This photogenerated current and voltage are called solar cell characterization parameters that can be presented by J-V curves. Among the favorable pathway of photocurrent generation, there are several scavenging pathways against the basic favorable working principle of QDSCs. There are more recombination pathways of photoexcited electron with photogenerated hole including (1) recombination of photoexcited electrons form CB with photogenerated holes in VB of QDs, (2) transfer back of photoexcited electrons from CB of TiO_2 with holes in VB of QDs, (3) recombination of photoexcited electrons form CB of QDs with transferred holes into electrolyte before oxidation, (4) recombination of injected electrons form TiO_2 with transferred holes into electrolyte before oxidization[120]. Most of these unfavorable events happen at junctions between TiO_2/working electrode/electrolyte that have received great attention by researchers recently[121–124].

One of the recent modification techniques in working electrode assembly is association of TiO_2 acceptor with quantum dots in which inorganic nanostructure metal sulfide semiconductors have gained interest due to their remarkable physical and chemical properties such as electronic, magnetic, and optic. J-V characteristics of CZTS can be enhanced by further development of CZTS nanocrystal. A new Fermi equilibrium can promote the effective charge carrier transfer by using nano-sized metal sulfides, which causes greater photovoltaic properties of semiconductor materials with longer carrier lifetime. Metals such as Au, Ag, and Cu can capture the solar radiations due to their light-trapping effect and strong surface plasmon resonance property[125]. Synthesis of Au-CZTS core-shell nanoparticles reported by Ha and et al[126] shows the enhancement of absorption in the Vis-NIR region and generation of more photoelectrons.

We are pursuing an alternative green method of solar cell assembly by direct in-situ biosynthesis of SnS QDs on TiO_2 as the harvesting light component in solar cell to enhance solar cell characterization parameters.

6.2. Results

6.2.1. Solar cell improvement by in-situ growth of nanocrystals

The initial improvement in quantum dots-sensitized solar cell (QDSSCs) is the fabrication method of photoanode. One of the traditional methods of fabrication is drop-casting method in which putting a drop of QDs solution on TiO_2 paste and dried the anode before solar cell assembly. In this method, synthesized nanoparticles are stayed in the surface of TiO_2 paste. It has been reported that TiO_2 particles have an association with metal sulfide nanocrystals. Figure 32 shows that the association of CZTS nanocrystals into the TiO_2 particles. In this experiment, annealed TiO_2 are resuspended into water and after sonication for 10 minutes, synthesized CZTS nanocrystals are mixed with TiO_2 solution. It is seen that CZTS absorption is increased with tiny shift in the absorption peak in the presence of TiO_2 particles. This increase may due to the lower transparency in the solution after mixing with TiO_2 particles. After the centrifuge, heavy TiO_2 particles make a pellet at the bottom of the tube. The reason of lower absorption of supernatant can demonstrate that most of CZTS nanoparticles are attached to the TiO_2 particles and sit with heavy TiO_2 particles in the pellet after centrifuge, which is consistent with other literatures. For example, Ghosh et al. reported that the weak van der Waals force between substrate surface and S^{2-} is the main force of adsorption of metals sulfides to TiO_2 paste[127].

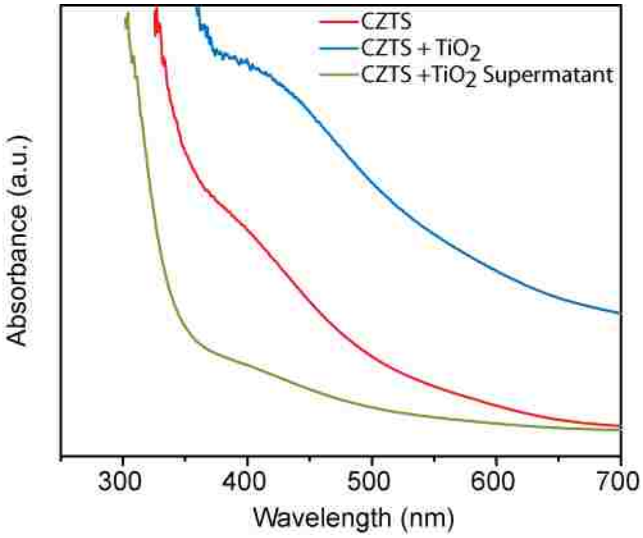

Figure 32: UV-Vis absorption of regular biosynthesis of CZTS (red line), added TiO_2 particles to biosynthesized CZTS (blue line), and supernatant of added TiO2 particles to biosynthesized CZTS after centrifuge (green line)

Due to the high affinity of metal sulfides to the TiO_2 substrate, innovative fabrication method of photoanode is applied by in-situ growth of nanocrystals in the presence of TiO_2 substrate. To assemble solar cells, working electrode is fabricated by in-situ growth of SnS or CZTS. After the annealing of TiO_2 paste on cleaned FTO, in-situ biosynthesis is started by immersing the TiO_2-paste FTO into the solution of metal precursors, L-Cysteine, and Enzyme. During the incubation of solution, biosynthesis of QDs happens in the presence of TiO_2 paste. Thus, QDs can penetrate into TiO_2 paste in contrast with other conventional fabrication methods in which QDs are just sitting on the surface of TiO_2 paste, Figure S40 and S41. Figure 33a and 33b are cross-sectional view SEM images of working electrodes that are fabricated by drop casting and in-situ growth of CZTS QDs on TiO_2 paste, respectively. SEM-EDAX scanning line of the thickness of TiO_2 paste can quantify the distribution of Cu-Zn-Sn-S elements in 200 points of TiO_2 paste. Figure 33a shows very low non-uniform distribution of S, Sn, Zn, and Cu by drop casting as a conventional method that presents the penetration of elements increase from the bottom to surface of TiO_2 paste, confirms surface coating of TiO_2 paste by CZTS QDs. However, Figure 33b, the cross-sectional view SEM image of working electrode, fabricated by in-situ growth of CZTS QDs, shows the uniform presence of all S, Sn, Zn, and Cu into TiO_2 paste. Also, SEM-EDAX scanning line of the thickness of TiO_2 paste confirms that in-situ biosynthesis of CZTS leads to homogeneous penetration of CZTS QDs into TiO_2 paste during the incubation.

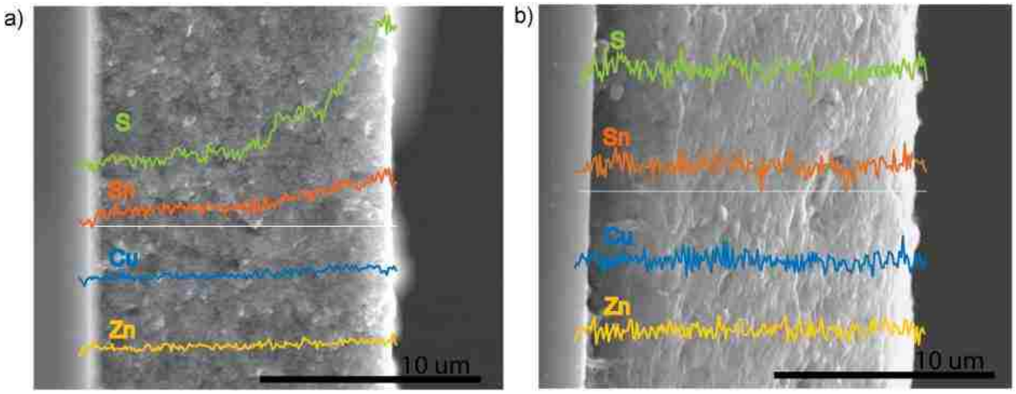

Figure 33: a) SEM cross-sectional view of drop-casting of CZTS on TiO_2 paste showing EDAX line scanning of Sn, S, Cu, Zn distribution sited on the surface of TiO_2 paste, b) SEM cross-sectional view of in-situ growth of CZTS on TiO_2 paste showing EDAX line scanning of Sn, S, Cu, Zn distribution penetrated into the TiO_2 paste

Figure 34 presents the solar cell characterization parameters of SnS QD-sensitized solar cell that is fabricated by drop-casting and in-situ growth method. It is clear that in-situ growth of SnS QDs on TiO_2 paste shows better performance under illumination. Enhanced FF, higher open-circuit voltage (V_{oc}), and higher short circuit current (J_{sc}) are due to the uniform penetration of QDs into the TiO_2 paste during the simultaneous synthesis of SnS QDs and anode fabrication.

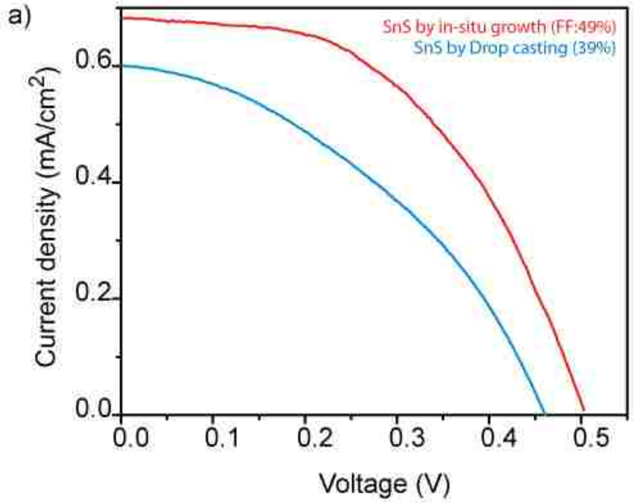

b)

	V_{oc} (V)	J_{sc} (mA/cm^2)	FF (%)
SnS by Drop casting	0.45	0.6	39
SnS by in-situ growth	0.5	0.69	49

Figure 34: J-V characteristics of TiO_2 thin film on FTO glass associated with SnS QDs in two fabrication methods, drop-casting (blue line) and in-situ growth method (red line).

6.2.2. Solar cell improvement by CuS cathode

Solar cells are assembled by three main components including photoanode, polysulfide electrolyte, and cathode. Many researchers have worked on the effect of cathode materials on solar cell performance. Previously, the applied cathode in assembled solar cells was Au. One of the other common high efficient cathode materials is CuS that is reported by literates[127–129]. Thus, CuS is formed on FTO glasses by electrochemical deposition method with Gamry instrument. SEM images and EDAX analysis confirm the formation of thin microlayer of CuS on FTO glass, Figure 35.

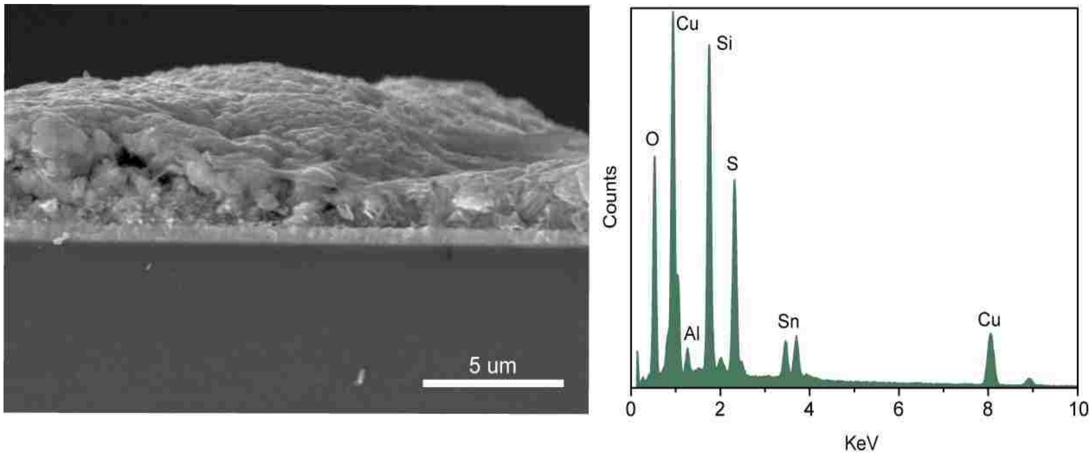

Figure 35: a) SEM cross-sectional view of CuS microlayer formed by electrochemical deposition, b) corresponding EDAX analysis showing the coexistence of Cu and S. (related Sn and Si peaks are come from FTO glass)

The effect of CuS cathode on solar cell performance is tested by J-V characterizes measurements of SnS QDs photoanodes that are fabricated by in-situ growth on TiO_2 paste. Figure 36 presents the solar cell performance of SnS QD-sensitized solar cells with Au and CuS as two cathodes. Control experiment that is Au cathode presents lower photovoltaic properties such as V_{oc} and *FF* suggesting the influence of better performance of solar cell by using CuS cathode. It can be seen that applying CuS cathode can enhance the short-circuit current density (J_{sc}) from 0.7 to 1.6 $mAcm^{-2}$, which causes the improvement in fill factor (*FF*) from 49% To 50%, which is a great improvement compared to other works[130].

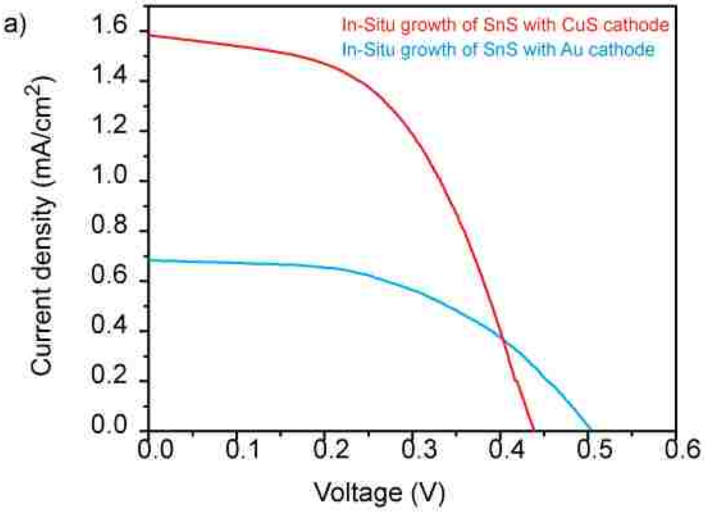

b)

	V_{oc} (V)	J_{sc} (mA/cm^2)	FF (%)
In-situ SnS anode with Au cathode	0.5	0.68	49
In-situ SnS anode with CuS cathode	0.43	1.6	50

Figure 36: J-V characteristics of TiO_2 thin film on FTO glass coated with SnS QDs synthesized (blue line). Photovoltaic behavior of TiO_2 (orange line) and synthesized solution (green line) without the presence of $SnCl_2$ are presented as reference experiments.

6.2.3. Solar cell improvement by Cu-Zn-Sn-S QDs

We showed that CuS cathode and in-situ growth fabrication of photoanode lead to better performance in SnS quantum dot-sensitized solar cell. Due to those modifications in solar cell components, FF of SnS QDSSC is improved from 39% to 50%. It is highly reported that SnS relative alloy like Cu-Zn-Sn-S can improve the solar cell efficiency due to its desirable band gap of CZTS.

J-V characteristics measurement shows the performance of SnS and CZTS QDs on TiO_2 prepared by in-situ synthesis, Figure 37. Control experiment that is TiO_2 in the absence of SnS presents lower photovoltaic properties such as V_{oc} and FF, Figure 37, suggesting the considerable influence of SnS QDs on TiO_2 in solar cells under visible irradiation. It can be seen that SnS QDs can enhance the open-circuit voltage (V_{oc}) considerably from 0.21 to 0.45 V with increase in short-circuit current density (J_{sc}) from 0.45 to 1.6 $mAcm^{-2}$, which causes the improvement in fill factor (FF) from 39% To 50%, which is a great improvement compared to other works[130]. This considerable enhancement in J-V characterization parameters and FF by SnS QDs can indicate the high probability of electron-hole recombination in SnS promising photovoltaic properties, which leads to potential applications of SnS nanocrystals in scale-up optoelectrical devices. Further improvement of solar cell performance was achieved by applying CZTS nanocrystals instead of SnS nanocrystals. Improvement in open-circuit voltage (V_{oc}) from 0.45 to 0.55 V is a considerable influence of applying CZTS as a working electrode in solar cell. Also, more than two times improvement in short-circuit current density (J_{sc}) causes an enhance in FF of solar cell from 50% to 61% when CZTS nanocrystals are used as an absorber layer in solar cell compared with applied SnS nanocrystals.

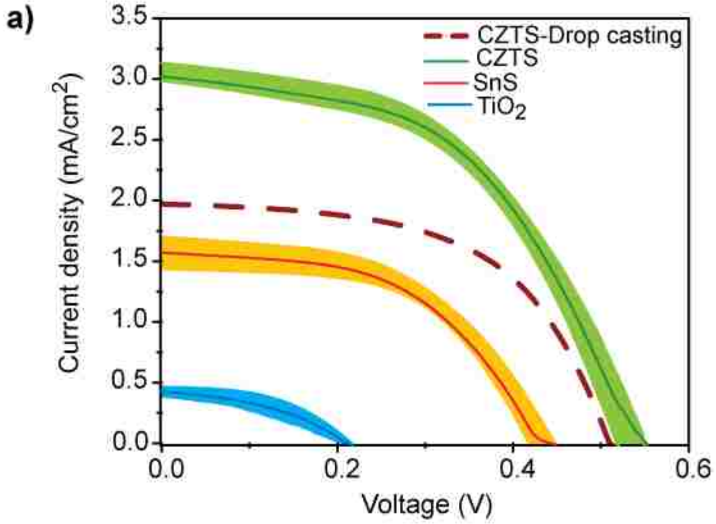

b)

	V_{oc} (V)	J_{sc} (mA/Cm^2)	FF (%)
TiO$_2$	0.21	0.45	39
SnS	0.45	1.6	50
CZTS	0.55	3.1	61
CZTS-Drop Casting	0.51	1.96	56

Figure 37: J-V characteristics of TiO$_2$ thin film on FTO glass coated with CZTS QDs synthesized

Higher FF of CZTS QDs than that of SnS QDs as an absorber layer in solar cells made by in-situ synthesis method could be due to higher density of deep defects of CZTS nanocrystals, which traps the charges and avoids electron-hole recombination[131]. V_{oc} can be increased by higher quality of crystals and lower defects inside the cell. Also, J_{sc} depends on the numbers of excited dyes and electrons injected to the conduction band and transmitted to the TiO$_2$ thin film and electrolyte. As a result, it can be concluded that high values photovoltaic properties such as V_{oc} and FF indicate good crystallinity of CZTS nanostructures. However, low J_{sc} indicates that the number of electrons injected into the conduction band are very low since they could not reach the surface of TiO$_2$.

6.2.4. Solar cell improvement by optimized CZTS composition

The last but not least improvement in solar cell performance is due to tuning the composition of CZTS by changing the nominal ratio of Cu:Zn:Sn in the synthesis solution.

Table 5: Composition ratio of CZTS pellet quantified by EDAX-SEM.

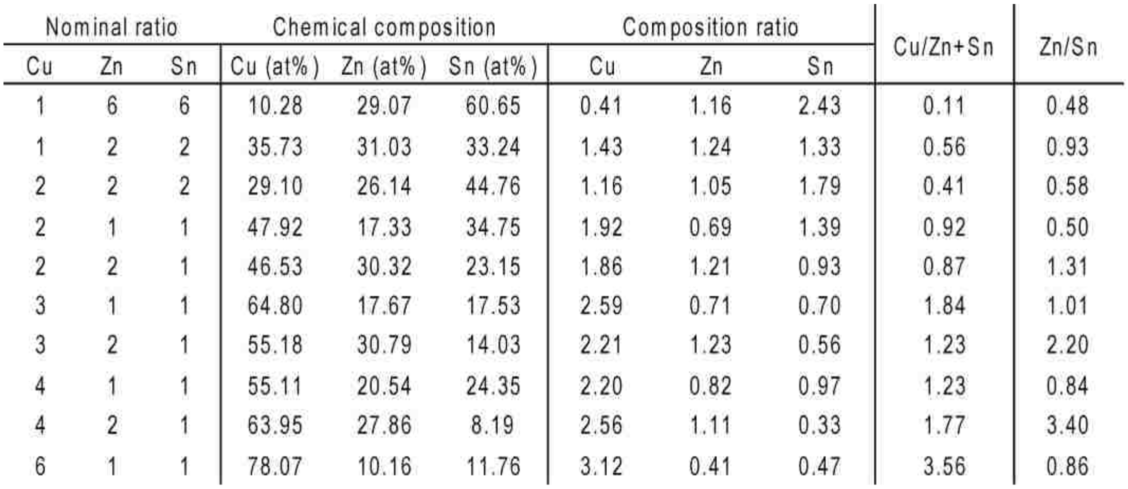

Nominal ratio			Chemical composition			Composition ratio			Cu/Zn+Sn	Zn/Sn
Cu	Zn	Sn	Cu (at%)	Zn (at%)	Sn (at%)	Cu	Zn	Sn		
1	6	6	10.28	29.07	60.65	0.41	1.16	2.43	0.11	0.48
1	2	2	35.73	31.03	33.24	1.43	1.24	1.33	0.56	0.93
2	2	2	29.10	26.14	44.76	1.16	1.05	1.79	0.41	0.58
2	1	1	47.92	17.33	34.75	1.92	0.69	1.39	0.92	0.50
2	2	1	46.53	30.32	23.15	1.86	1.21	0.93	0.87	1.31
3	1	1	64.80	17.67	17.53	2.59	0.71	0.70	1.84	1.01
3	2	1	55.18	30.79	14.03	2.21	1.23	0.56	1.23	2.20
4	1	1	55.11	20.54	24.35	2.20	0.82	0.97	1.23	0.84
4	2	1	63.95	27.86	8.19	2.56	1.11	0.33	1.77	3.40
6	1	1	78.07	10.16	11.76	3.12	0.41	0.47	3.56	0.86

Regards to the application of CZTS as an absorber layer in QDSSCs, controlling the ratio of Cu and Zn precursors are playing a significant role in solar cell performance, that are defined as Cu/Zn+Sn and Zn/Sn atomic ratios. Researchers have demonstrated that formation of Cu vacancies (V_{Cu}) and avoid domination of valence difference between Cu and Zn (Cu_{Zn})[132] are the most effect of controlling the precursors ratio. Also, it is reported that stoichiometry formation of CZTS happens in the very small region of nominal molar ratio. As a result, it is important to control the CZTS composition to form the optimal composition, dominate V_{Cu} and Zn_{Cu}, and avoid formation of secondary phases like ZnS[133]. The best solar cell performance happens when Cu/Zn+Sn and Zn/Sn are in the range 0.73-0.96 and 1.00-1.71, respectively[132–138].

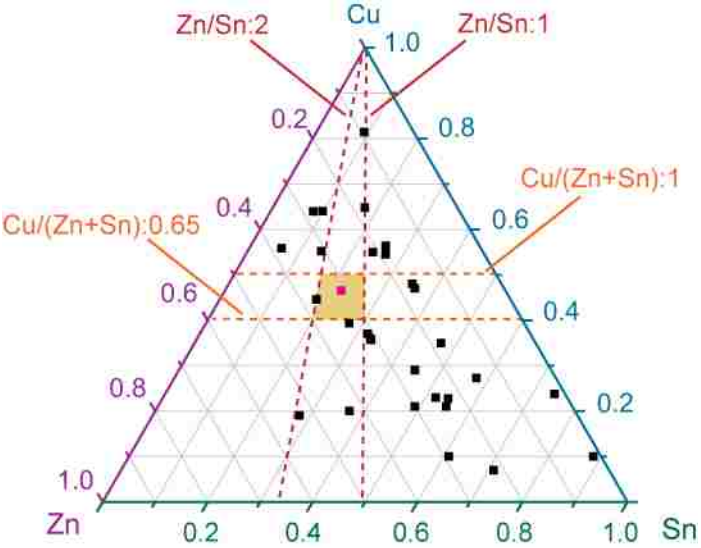

Figure 38: Pseudo-ternary phase diagram of Cu-Zn-Sn based on SEM-EDAX quantification of several CTZS samples synthesized with various nominal molar ratio of Cu:Zn:Sn. The optimal composition is shown as a red point siting in the ordered range of Cu/Zn+Sn and Zn/Sn.

Figure 38 is pseudo-ternary phase diagram of CZTS composition based on EDAX through SEM analysis of synthesized CZTS with various nominal ratio of Cu:Zn:Sn. To follow the order of forming the optimal CZTS composition, we consider Cu/Zn+Sn and Zn/Sn in the range of 0.65-1.00 and 1.00-2.00, respectively. The red point showed in Figure 38 is correspond to the Cu nominal molar ratio of 2 that forms chemical composition of $Cu_{1.9}Zn_{1.2}Sn_{0.9}S_4$, that is the closest composition to the ideal stoichiometry ratio of 2:1:1:4.

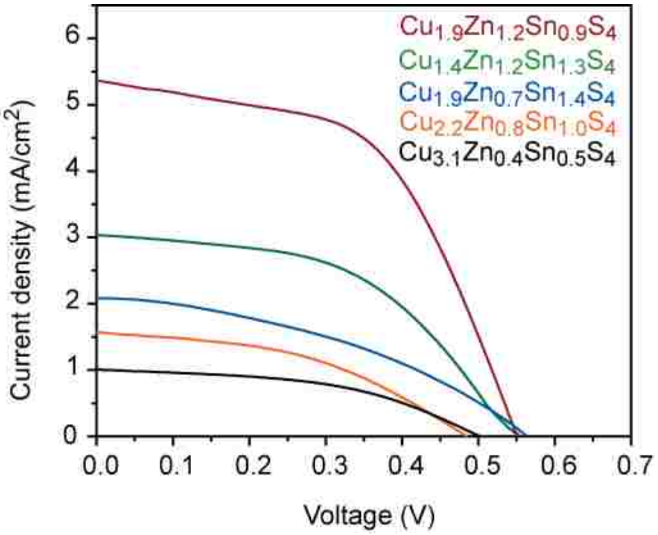

Figure 39: effect of CZTS composition on solar cell presented by J-V characteristic measurement

Depends on the nominal ratio of Cu:Zn:Sn in CZTS composition, Cu/Zn+Sn and Zn/Sn ratios change in composition that influence the performance of solar cell. Figure 39 shows that the optimized CZTS composition, $Cu_{1.9}Zn_{1.2}Sn_{0.9}S_4$, has the best performance among other compositions, that follows the order of Cu-poor and Zn-rich solution. The corresponding ratios of Cu/Zn+Sn and Zn/Sn are 0.87 and 1.31, respectively, Table 5.

6.3. Conclusions

Modified working electrode of quantum dot-sensitized solar cell was fabricated on FTO glass substrate by in-situ biosynthesis of CZTS quantum dots. Engineered single enzyme, smSCE, biomineralized CZTS quantum dots in the presence of L-cysteine at ambient conditions. Both TEM and XRD analysis confirmed the crystallite of biosynthesized CZTS. Also, biosynthesized QDs can attached to TiO_2 particles that could be the reason of fully diffusion of QDs into the TiO_2 paste on FTO substrate through in-situ biosynthesis of QDs, characterized by SEM-EDAX line scanning. Improved working electrodes of in-situ biosynthesized CZTS QDs were applied in solar cell assembly associated with CuS counter electrode, which leads to enhancement in solar cell characterization parameters (V_{oc} and J_{sc}) and FF of 61% for utilized CZTS QDs.

6.4. Supplemental Information

The following information is provided for the presented results in section 6.2 as supplementary data:

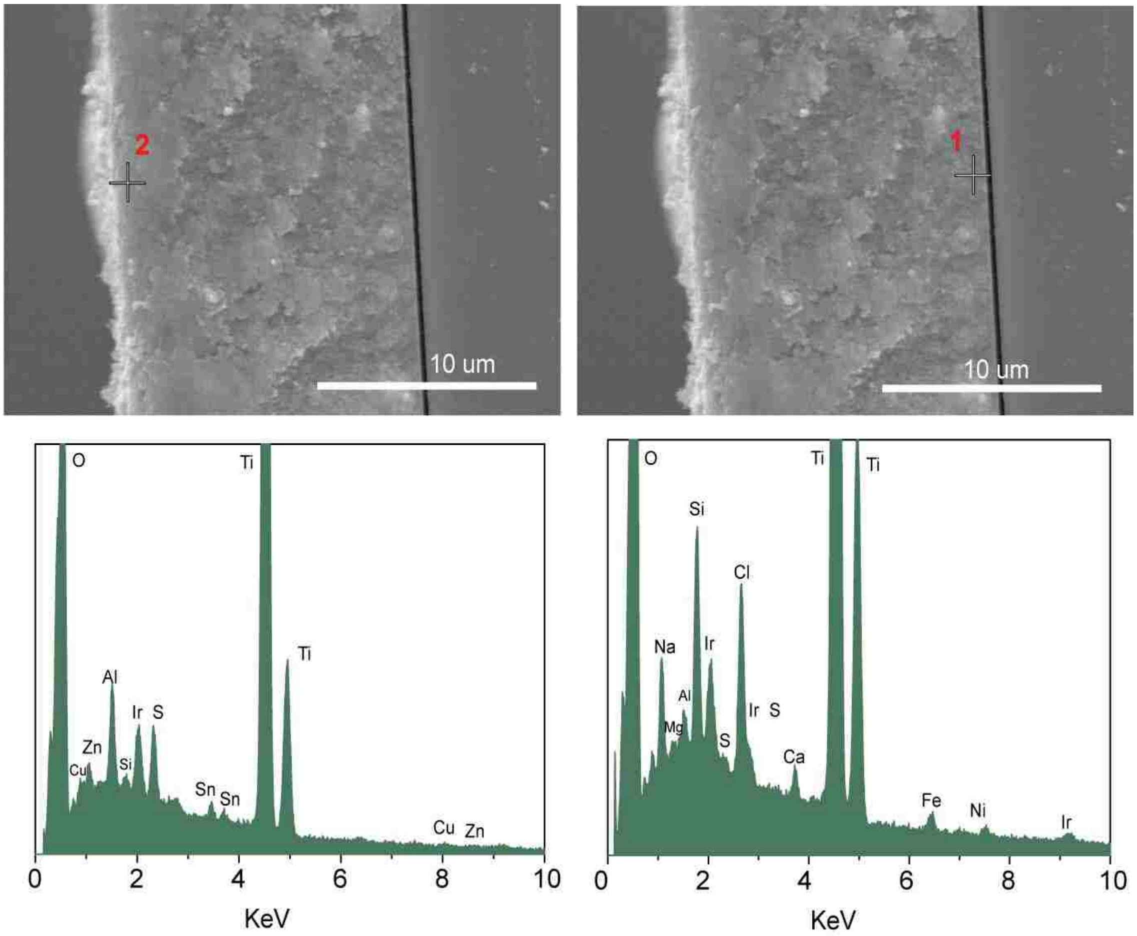

Figure 40**:** SEM-EDAX analysis of CZTS nanocrystals distribution on TiO_2 paste by Drop casting method; a) cross-sectional view SEM images of TiO_2 paste on FTO glass substrate, b) cross-sectional view SEM-EDAX spotting of top and bottom layer of TiO_2 paste

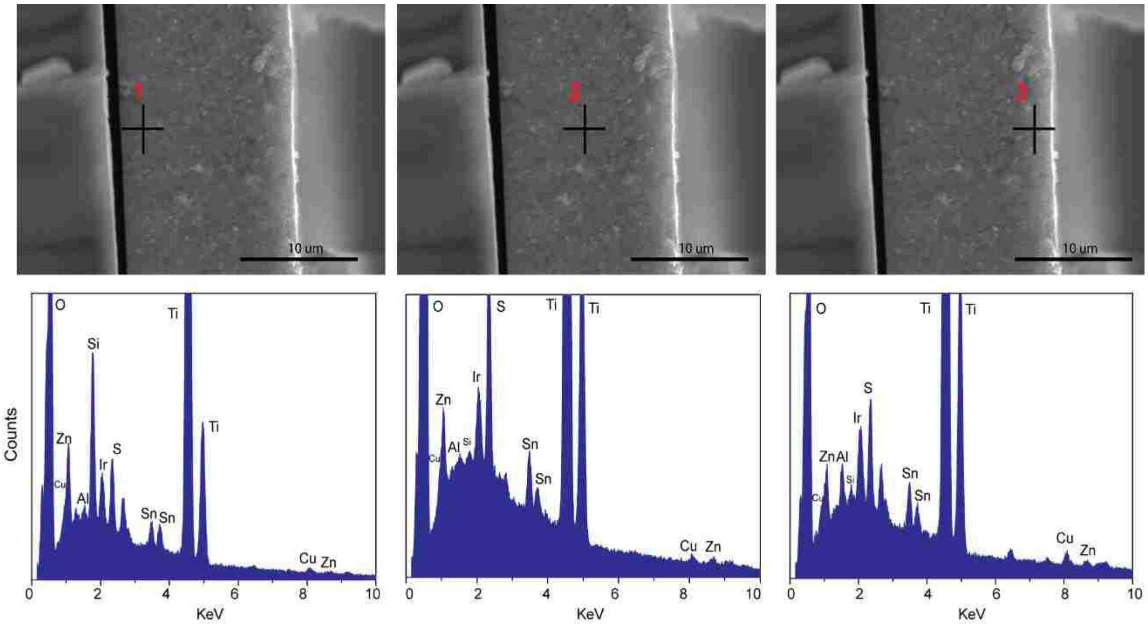

Figure 41: SEM-EDAX analysis of in-situ growth of CZTS nanocrystals distribution on TiO_2; a) cross view SEM images of TiO_2 paste on FTO glass substrate, b) cross-sectional view SEM-EDAX spotting of top, middle, and bottom layer of TiO_2 paste

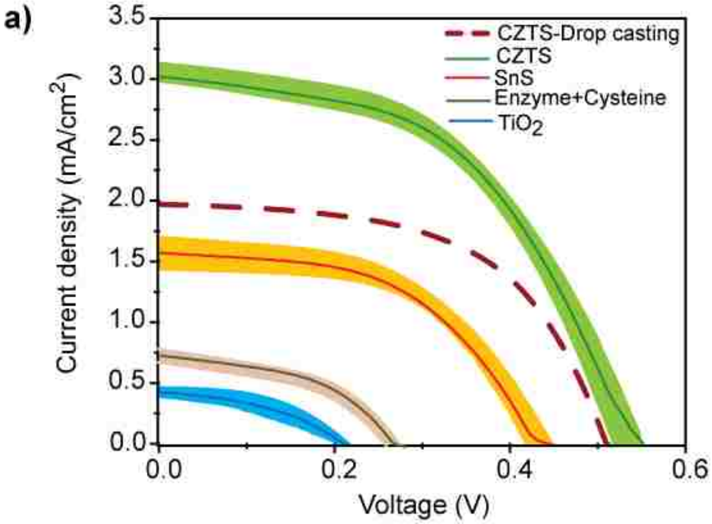

b)

	V_{oc} (V)	J_{sc} (mA/cm2)	FF (%)
TiO_2	0.21	0.45	39
Enzyme+Cysteine	0.27	0.74	41
SnS	0.45	1.6	50
CZTS	0.55	3.1	61
CZTS-Drop casting	0.51	1.96	56

Figure 42**:** J-V curve of solar cell characterization comparison; a) J-V curve of TiO_2 paste on FTO substrate, In-situ growth of SnS QDs, In-situ growth of CZTS QDs, and drop-casted CZTS on TiO_2 paste, b) Table of corresponding solar cell characterization parameters

Conclusion

In this work, biomineralization was studied as a green, low cost synthesis method of various crystals in which a single enzyme is responsible for catalyzing the reaction and templating the crystallization. We showed that engineered enzyme can synthesis crystals at room temperature and ambient conditions in aqueous phase, which decrease the implements of their potential application in industrial scales.

Chapter 3 demonstrated the bio-imitation of $CaCO_3$ with vaterite and aragonite crystal structures by utilizing well-known protein called Silicatein α at room temperature and aqueous phase. We designed only one crystallization method that can form calcite, vaterite, and aragonite as three morphologies of $CaCO_3$. First, in the absence of Silicatein, crystallization of calcite in cubic shape was confirmed by SEM images and XRD. Second, when silicatein was added to the solution, XRD confirmed the change in crystal structure to vaterite with mushroom-like shape. Then, the third $CaCO_3$ morphology, aragonite, was achieved by adding silicatein and Mg^{2+} into the solution. SEM images showed the rod-liked shape particles formed in a circular symmetry. We showed that higher concentration of Silicatein and higher ratio of Mg/Ca leads to higher ratio of aragonite formation.

Chapter 4 demonstrated that cystathionine γ-lyase is able to turn over L-Cysteine to H_2S, as a source of sulfur, at ambient conditions. ZnS nanocrystals was biosynthesized in the presence of SCE and L-cysteine with great optical properties showed by absorbance spectrum and photoluminescence. We also biosynthesized $Zn_xCd_{1-x}S$ nanocrystals as a ZnS alloy with tunable band gap when the ratio of Zn:Cd was changed. Next, quantum yield of biosynthesized ZnS, and $Zn_xCd_{1-x}S$ was improved by synthesis of $Zn_xCd_{1-x}S$-ZnS core-shell in which Zn precursor, SCE, and l-cysteine was added to a solution of pre-synthesized $Zn_xCd_{1-x}S$ for second incubation. We showed that

$Zn_xCd_{1-x}S$-ZnS core-shell can enhance the QY to 7% and increase 97.6 ns in decay time confirmed by life time decay photoluminescent.

Additional biosynthesis of metal sulfides by utilizing SCE was described in chapter 5 in which SnS nanocrystals was biosynthesized with the same procedure. XRD, HRTEM and HAADF was confirmed the crystal structure of SnS nanocrystals. The most relative compound of SnS, CuZnSnS was synthesized by incubation of Zn, Cu, Sn precursors in the presence of CSE and l-cysteine. Biosynthesized CZTS QDs was confined in nanocrystals by XRD and HRTEM.

Chapter 6 demonstrated the application of QDs as an absorber layer in working electrode of sensitized solar cell. In this work, we showed the innovative green method of working electrode fabrication of QDSSCs in which SnS and CZTS QDs were biosynthesized directly on TiO_2-paste of working electrode. In-situ growth of QDs caused a uniform penetration of all elements in thickness of TiO_2 paste during the biosynthesis that leads to improvement in solar cell characterization parameters of solar cell such as V_{oc}, J_{sc}, and FF to 5.5 V, 3.1 $\frac{\text{mA}}{\text{cm}^2}$, and 61%, respectively.

List of publications

1- A. Sadeghnejad, L. Lu, C. J. Kiely, B. W. Berger, S. McIntosh, “Single enzyme direct biomineralization of ZnS, $Zn_xCd_{1-x}S$ and $Zn_xCd_{1-x}S$–ZnS quantum confined nanocrystals” RSC Advances, 2017, 7, 38490-38497.

Bibliography

1. Chaki, S. H. *et al.* Wet chemical synthesis and characterization of SnS2 nanoparticles. *Appl. Nanosci.* **3,** 189–195 (2013).
2. Yin, Y. & Talapinb, D. The chemistry of functional nanomaterials. *Chem. Soc. Rev.* **42,** 2484–2487 (2013).
3. Chiu, C.-Y., Ruan, L. & Huang, Y. Biomolecular specificity controlled nanomaterial synthesis. *Chem. Soc. Rev.* **42,** 2512–2527 (2013).
4. Li, J. J. *et al.* Large-Scale Synthesis of Nearly Monodisperse CdSe/CdS Core/Shell Nanocrystals Using Air-Stable Reagents via Successive Ion Layer Adsorption and Reaction. *J. Am. Chem. Soc.* **125,** 12567–12575 (2003).
5. Doke, S., Sonawane, K., Raghavendra Reddy, V., Ganguly, P. & Mahamuni, S. Low power operated highly luminescent ferroelectric liquid crystal doped with CdSe/ZnSe core/shell quantum dots. *Liq. Cryst.* 1–7 (2018). doi:10.1080/02678292.2018.1449260
6. Tang, J. *et al.* Morphology Evolution of Gradient-Alloyed CdxZn1–xSeyS1–y@ZnS Core–Shell Quantum Dots during Transmission Electron Microscopy Determination: A Route to Illustrate Strain Effects. *J. Phys. Chem. C* **122,** 4583–4588 (2018).
7. Datta, A., Panda, S. K. & Chaudhuri, S. Synthesis and Optical and Electrical Properties of CdS / ZnS Core / Shell Nanorods. *J. Phys. Chem. C* **111,** 17260–17264 (2007).
8. Colvin, V. L., Schlamp, M. C. & Allvisatos, A. P. Light-emitting diodes made from cadmium selenide nanocrystals and a semiconducting polymer. *Nature* **370,** 354–357 (1994).
9. Kairdolf, B. A. *et al.* Semiconductor Quantum Dots for Bioimaging and Biodiagnostic Applications. *Annu. Rev. Anal. Chem.* **6,** 143–162 (2013).

10. Carey, G. H. *et al.* Colloidal Quantum Dot Solar Cells. *Chem. Rev.* **115,** 12732–12763 (2015).
11. Klimov, V. I., Mikhailovsky, A. A., McBranch, D. W., Leatherdale, C. A. & Bawendi, M. G. Quantization of Multiparticle Auger Rates in Semiconductor Quantum Dots. *Science (80-.).* **287,** 1011 LP-1013 (2000).
12. Medintz, I. L., Uyeda, H. T., Goldman, E. R. & Mattoussi, H. Quantum dot bioconjugates for imaging, labelling and sensing. *Nat. Mater.* **4,** 435 (2005).
13. Li, Q. *et al.* Highly Efficient Visible-Light-Driven Photocatalytic Hydrogen Production of CdS-Cluster-Decorated Graphene Nanosheets. *J. Am. Chem. Soc.* **133,** 10878–10884 (2011).
14. Shen, L., Liang, S., Wu, W., Liang, R. & Wu, L. CdS-decorated UiO–66(NH2) nanocomposites fabricated by a facile photodeposition process: an efficient and stable visible-light-driven photocatalyst for selective oxidation of alcohols. *J. Mater. Chem. A* **1,** 11473 (2013).
15. Dubertret, B. *et al.* In Vivo Imaging of Quantum Dots Encapsulated in Phospholipid Micelles. *Science (80-.).* **298,** 1759 LP-1762 (2002).
16. Bai, H.-J. & Zhang, Z.-M. Microbial synthesis of semiconductor lead sulfide nanoparticles using immobilized Rhodobacter sphaeroides. *Mater. Lett.* **63,** 764–766 (2009).
17. Yugang Sun and Younan Xia. Large-Scale Synthesis of Uniform Silver Nanowires Through a Soft,Self-Seeding,Polyol Process. *Adv. Mater.* **4095,** 833–837 (2002).
18. Sachin, S., K., S. & Meenal, K. Green synthesis of lead sulfide nanoparticles by the lead resistant marine yeast, Rhodosporidium diobovatum. *Biotechnol. Prog.* **27,** 1464–1469 (2011).
19. Speirs, M. J. *et al.* Origin of the increased open circuit voltage in PbS–CdS core–shell quantum dot solar cells. *J. Mater. Chem. A* **3,** 1450–1457 (2015).
20. Ma, N., Marshall, A. F. & Rao, J. Near-Infrared Light Emitting Luciferase via

Biomineralization. *J. Am. Chem. Soc.* **132,** 6884–6885 (2010).

21. Singh, S., Bozhilov, K., Mulchandani, A., Myung, N. & Chen, W. Biologically programmed synthesis of core-shell CdSe/ZnS nanocrystals. *Chem. Commun.* **46,** 1473–1475 (2010).
22. Gaponik, N., Talapin, D. V, Rogach, A. L., Eychmüller, A. & Weller, H. Efficient Phase Transfer of Luminescent Thiol-Capped Nanocrystals: From Water to Nonpolar Organic Solvents. *Nano Lett.* **2,** 803–806 (2002).
23. Semonin, O. E. *et al.* Absolute Photoluminescence Quantum Yields of IR-26 Dye, PbS, and PbSe Quantum Dots. *J. Phys. Chem. Lett.* **1,** 2445–2450 (2010).
24. Kumnorkaew, P., Ee, Y.-K., Tansu, N. & Gilchrist, J. F. Investigation of the Deposition of Microsphere Monolayers for Fabrication of Microlens Arrays. *Langmuir* **24,** 12150–12157 (2008).
25. Bisquert, J. & Mora-Seró, I. Simulation of steady-state characteristics of dye-sensitized solar cells and the interpretation of the diffusion length. *J. Phys. Chem. Lett.* **1,** 450–456 (2010).
26. Santoni, A. *et al.* Valence band offset at the CdS/Cu2ZnSnS4 interface probed by x-ray photoelectron spectroscopy. *J. Phys. D. Appl. Phys.* **46,** 1–5 (2013).
27. Li, J. *et al.* The band offset at CdS/Cu 2ZnSnS 4 heterojunction interface. *Electron. Mater. Lett.* **8,** 365–367 (2012).
28. Yan, C. *et al.* Band alignments of different buffer layers (CdS, Zn(O,S), and In 2S3) on Cu2ZnSnS4. *Appl. Phys. Lett.* **104,** 173901–173904 (2014).
29. Fabregat-Santiago, F., Garcia-Belmonte, G., Mora-Seró, I. & Bisquert, J. Characterization of nanostructured hybrid and organic solar cells by impedance spectroscopy. *Phys. Chem. Chem. Phys.* **13,** 9083–9118 (2011).
30. Kamat, P. V. Boosting the efficiency of quantum dot sensitized solar cells through modulation of interfacial charge transfer. *Acc Chem Res* **45,** 1906–1915 (2012).
31. Lee, M. M., Teuscher, J., Miyasaka, T., Murakami, T. N. & Snaith, H. J. Efficient

Hybrid Solar Cells Based on Meso-Superstructured Organometal Halide Perovskites. *Science (80-.).* **338,** 643−647 (2012).

32. Gimenez, S. *et al.* Improving the performance of colloidal quantum-dot-sensitized solar cells. *Nanotechnology* **20,** 1–6 (2009).
33. Jiang, Y. *et al.* Yan Jiang, Xing Zhang, Qian-Qing Ge, Bin-Bin Yu, Yu-Gang Zou, Wen-Jie Jiang, Wei-Guo Song, * Li-Jun Wan, * and Jin-Song Hu *. *Nano Lett.* **14,** 365–372 (2014).
34. Dunleavy, R., Lu, L., Kiely, C. J., Mcintosh, S. & Berger, B. W. Single-enzyme biomineralization of cadmium sulfide nanocrystals with controlled optical properties. *PNAS* **113,** 5275–5280 (2016).
35. Yang, Z. *et al.* Biomanufacturing of CdS quantum dots. *Green Chem.* **17,** 3775–3782 (2015).
36. Petty, K. J. Metal-chelate affinity chromatography. *Curr. Protoc. Protein Sci.* **4,** 1–16 (2001).
37. Spangler, L. C., Lu, L., Kiely, C. J., Berger, B. W. & Mcintosh, S. Biomineralization of PbS and PbS–CdS core–shell nanocrystals and their application in quantum dot sensitized solar cells. *J. Mater. Chem. A* **4,** 6107–6115 (2016).
38. Zhao, K., Yu, H., Zhang, H. & Zhong, X. Electroplating Cuprous Sulfide Counter Electrode for High-Efficiency Long-Term Stability Quantum Dot Sensitized Solar Cells. *J. Phys. Chem. C* **118,** 5683–5690 (2014).
39. Jones, G., Jackson, W. R., Choi, C. Y. & Bergmark, W. R. Solvent effects on emission yield and lifetime for coumarin laser dyes. Requirements for a rotatory decay mechanism. *J. Phys. Chem.* **89,** 294–300 (1985).
40. Fu, G., Valiyaveettil, S., Wopenka, B. & Morse, D. E. CaCO 3 Biomineralization : Acidic 8-kDa Proteins Isolated from Aragonitic Abalone Shell Nacre Can Specifically Modify Calcite Crystal Morphology. *Biomacromolecules* **6,** 1289–1298 (2005).

41. Lakshminarayanan, R., Valiyaveettil, S. & Loy, G. L. Selective Nucleation of Calcium Carbonate Polymorphs : Role of Surface Functionalization and Poly (Vinyl Alcohol) Additive 2003. *Cryst. Growth Des.* **3,** 953–958 (2003).
42. Willinger, M. *et al.* Structural evolution of aragonite superstructures obtained in the presence of the siderophore deferoxamine. *CrystEngComm* **17,** 3927–3935 (2015).
43. Checa, A. G., Okamoto, T. & Ramírez, J. Organization pattern of nacre in Pteriidae (Bivalvia: Mollusca) explained by crystal competition. *Proc. R. Soc. London B Biol. Sci.* **273,** 1329–1337 (2006).
44. Kawano, J., Maeda, S. & Nagai, T. The effect of Mg 2 + incorporation on the structure of calcium carbonate clusters : investigation by the anharmonic downward distortion following method. *Phys. Chem. Chem. Phys.* **18,** 2690–2698 (2016).
45. Seto, J. *et al.* Structure-property relationships of a biological mesocrystal in the adult sea urchin spine. *PNAS* **109,** 3699–3704 (2012).
46. Tong, H. *et al.* Control over the crystal phase , shape , size and aggregation of calcium carbonate via a l -aspartic acid inducing process. *Biomaterials* **25,** 3923–3929 (2004).
47. Sondi, I. & Matijevic, E. Homogeneous Precipitation of Calcium Carbonates by Enzyme Catalyzed Reaction. *J. Colloid Interface Sci.* **238,** 208–214 (2001).
48. Park, W. K. *et al.* Effects of magnesium chloride and organic additives on the synthesis of aragonite precipitated calcium carbonate. *J. Cryst. Growth* **310,** 2593–2601 (2008).
49. Blue, C. R. *et al.* ScienceDirect Chemical and physical controls on the transformation of amorphous calcium carbonate into crystalline CaCO 3 polymorphs. *Geochim. Cosmochim. Acta* **196,** 179–196 (2017).
50. Hu, Z. & Deng, Y. Synthesis of needle-like aragonite from calcium chloride and sparingly soluble magnesium carbonate. *Powder Technol.* **140,** 10–16 (2004).

51. Wang, X., Schroder, H. C. & Muller, W. E. G. Enzyme-based biosilica and biocalcite : biomaterials for the future in regenerative medicine. *Trends Biotechnol.* **32,** 441–447 (2014).

52. Sarikaya, M., Tamerler, C., Jen, A. K., Schulten, K. & Baneyx, F. Molecular biomimetics : nanotechnology through biology. *Nat. Mater.* **2,** 577–585 (2003).

53. Ikuma, K., Decho, A. W. & Lau, B. L. T. When nanoparticles meet biofilms — interactions guiding the environmental fate and accumulation of nanoparticles. *Front. Microbiol.* **6,** 1–6 (2015).

54. Vitor, G. *et al.* Start-up , adjustment and long-term performance of a two-stage bioremediation process , treating real acid mine drainage , coupled with biosynthesis of ZnS nanoparticles and ZnS / TiO 2 nanocomposites. *Miner. Eng.* **75,** 85–93 (2015).

55. Labrenz, M. & Banfield, J. F. Sulfate-Reducing Bacteria-Dominated Biofilms That Precipitate ZnS in a Subsurface Circumneutral-pH Mine Drainage System. *Microb. Ecol.* **47,** 205–217 (2004).

56. Gramp, J. P., Bigham, J. M., Sasaki, K. & Tuovinen, O. H. Formation of Ni-and Zn-sulfides in cultures of sulfate-reducing bacteria. *Geomicrobiol. J.* **24,** 609–614 (2007).

57. Yang, Z., Lu, L., Kiely, C. J., Berger, B. W. & Mcintosh, S. Biomineralized CdS Quantum Dot Nanocrystals : Optimizing Synthesis Conditions and Improving Functional Properties by Surface Modi fi cation. *Ind. Eng. Chem. Res.* **55,** 11235 − 11244 (2016).

58. Curran, C. D. *et al.* Direct Single-Enzyme Biomineralization of Catalytically Active Ceria and Ceria − Zirconia Nanocrystals. *ACS Nano* **11,** 3337−3346 (2017).

59. Unni, C., Philip, D. & Gopchandran, K. G. Studies on optical absorption and photoluminescence of thioglycerol-stabilized ZnS nanoparticles. *Opt. Mater. (Amst).* **32,** 169–175 (2009).

60. Kumbhojkar, N., Nikesh, V. V, Kshirsagar, A. & Mahamuni, S. Photophysical properties of ZnS nanoclusters Photophysical properties of ZnS nanoclusters. *J. Appl. Phys.* **88,** 6260–6264 (2000).

61. Bochev, B. & Yordanov, G. Colloids and Surfaces A : Physicochemical and Engineering Aspects Room temperature synthesis of thioglycolate-coated zinc sulfide (ZnS) nanoparticles in aqueous medium and their physicochemical characterization. *Physicochem. Eng. Asp.* **441,** 84–90 (2014).

62. T. K. Bergstressr & Cohen, M. L.)=1«rr). *Phys. Rev.* **164,** 1069–1080 (1967).

63. Rogach, A. L., Kornowski, A., Gao, M. & Eychmu, A. Synthesis and Characterization of a Size Series of Extremely Small Thiol-Stabilized CdSe Nanocrystals. *J. Phys. Chem. B* **103,** 3065–3069 (1999).

64. Vivian, J. T. & Callis, P. R. Mechanisms of Tryptophan Fluorescence Shifts in Proteins. *Biophys. J.* **80,** 2093–2109 (2001).

65. Trajic, J. *et al.* Raman spectroscopy of ZnS quantum dots. *J. Alloys Compd.* **637,** 401–406 (2015).

66. Mariappan, R., Ragavendar, M. & Ponnuswamy, V. Growth and characterization of chemical bath deposited Cd 1 − x Zn x S thin films. *J. Alloys Compd.* **509,** 7337–7343 (2011).

67. Bera, K., Saha, S., Rana, C. & Jana, paresh chandra. composition dependent structural and optical properties of nanocrystallites ZnxCd1-xS. *Phys. Sci. Int. J.* **10,** 1–6 (2016).

68. Safta, N., Sakly, A., Mejri, H. & Bouazra, Y. Electronic and optical properties of Cd 1 − x Zn x S nanocrystals. *Eur. Phys. J. B* **51,** 75–78 (2006).

69. Fang, X. *et al.* ZnS nanostructures: From synthesis to applications. *Prog. Mater. Sci.* **56,** 175–287 (2011).

70. Bae, W. K., Nam, M. K., Char, K. & Lee, S. Gram-Scale One-Pot Synthesis of Highly Luminescent Blue Emitting Cd 1 - x Zn x S / ZnS Nanocrystals. *Chem. Mater* **20,** 5307–5313 (2008).

71. Steckel, J. S. *et al.* Blue Luminescence from (CdS)ZnS Core–Shell Nanocrystals**. *Angew. Chem. Int. Ed.* **43,** 2154–2158 (2004).
72. Berends, A. C. *et al.* Radiative and Nonradiative Recombination in CuInS 2 Nanocrystals and CuInS 2 - Based Core/Shell Nanocrystals. *J. Phys. Chem. Lett.* **7,** 3503−3509 (2016).
73. Cao, S. *et al.* Robust and Stable Ratiometric Temperature Sensor Based on Zn – In – S Quantum Dots with Intrinsic Dual-Dopant Ion Emissions. *Adv. Funct. Mater.* **26,** 7224–7233 (2016).
74. Liu, X., Jiang, Y., Fu, F. & Guo, W. Materials Science in Semiconductor Processing Facile synthesis of high-quality ZnS , CdS , CdZnS , and CdZnS / ZnS core / shell quantum dots : characterization and diffusion mechanism. *Mater. Sci. Semicond. Process.* **16,** 1723–1729 (2013).
75. Ghatak, A., Debnath, G. H. & Mukherjee, P. Lanthanide cation-induced tuning of surface capping properties in zinc sulfide nanoparticles: an infrared absorption study. *RSC Adv.* **5,** 32920–32932 (2015).
76. Li, Y., Ding, Y., Zhang, Y. & Qian, Y. Photophysical properties of ZnS quantum dots. *J. Phys. Chem. Solids* **60,** 13–15 (1999).
77. Manzoor, K., Vadera, S. R., Kumar, N. & Kutty, T. R. N. Synthesis and photoluminescent properties of ZnS nanocrystals doped with copper and halogen. *Mater. Chem. Phys.* **82,** 718–725 (2003).
78. Tang, H., Xu, G., Weng, L., Pan, L. & Wang, L. Luminescence and photophysical properties of colloidal ZnS nanoparticles. *Acta Mater.* **52,** 1489–1494 (2004).
79. Lu, H., Chu, S. & Tan, S. The characteristics of low-temperature-synthesized ZnS and ZnO nanoparticles. *J. Cryst. Growth* **269,** 385–391 (2004).
80. Ouyang, J. *et al.* Gradiently Alloyed Zn x Cd 1 - x S Colloidal Photoluminescent Quantum Dots Synthesized via a Noninjection One-Pot Approach. *J. Phys. Chem. C,* **112,** 4908–4919 (2008).
81. Xing, C., Zhang, Y., Yan, W. & Guo, L. Band structure-controlled solid solution

of Cd 1 − x Zn x S photocatalyst for hydrogen production by water splitting. *Int. J. Hydrogen Energy* **31,** 2018–2024 (2006).

82. Kim, M. R., Kang, Y.-M. & Jang, D.-J. Synthesis and Characterization of Highly Luminescent CdS@ ZnS Core− Shell Nanorods. *J. Phys. Chem. C* **111,** 18507–18511 (2007).
83. Xie, R., Kolb, U., Li, J., Basche, T. & Mews, A. Synthesis and Characterization of Highly Luminescent. *J. Am. Chem. Soc.* **127,** 7480–7488 (2005).
84. Nakagawa, H. & Kimura, H. Purification and properties of cystathionine synthetase from rat liver: separation of cystathionine synthetase from serine dehydratase. *Biochem. Biophys. Res. Commun.* **32,** 208–214 (1968).
85. Brown, F. C. & Gordon, P. H. Cystathionine synthase from rat liver: partial purification and properties. *Can. J. Biochem.* **49,** 484–491 (1971).
86. Spangler, L. C. *et al.* Enzymatic biomineralization of biocompatible CuInS2, (CuInZn)S2 and CuInS2/ZnS core/shell nanocrystals for bioimaging. *Nanoscale* **9,** 9340–9351 (2017).
87. Karar, N., Singh, F. & Mehta, B. R. Structure and photoluminescence studies on ZnS: Mn nanoparticles. *J. Appl. Phys.* **95,** 656–660 (2004).
88. Hegde, S. S., Kunjomana, A. G., Ramesh, K., Chandrasekharan, K. A. & Prashantha, M. Preparation and Characterization of SnS Thin Films for Solar Cell Application. *Int. J. Soft Comput. Eng.* **1,** 38–40 (2011).
89. Stavrinadis, A. *et al.* SnS/PbS nanocrystal heterojunction photovoltaics. *Nanotechnology* **21,** (2010).
90. Muthuvinayagam, A., Manovah David, T. & Sagayaraj, P. Investigation on a one-pot hydrothermal approach for synthesizing high quality SnS quantum dots. *J. Alloys Compd.* **579,** 594–598 (2013).
91. Prastani, C., Nanu, M., Nanu, D. E., Rath, J. K. & Schropp, R. E. I. Synthesis and conductivity mapping of SnS quantum dots for photovoltaic applications. *Mater. Sci. Eng. B* **178,** 656–659 (2013).

92. Xu, Y., Al-Salim, N., Bumby, C. W. & Tilley, R. D. Synthesis of SnS Quantum Dots. *J. Am. Chem. Soc.* **131,** 15990–15991 (2009).
93. Tang, P. *et al.* Nanoparticulate SnS as an efficient photocatalyst under visible-light irradiation. *Mater. Lett.* **65,** 450–452 (2011).
94. Deepa, K. G. & Nagaraju, J. Materials Science in Semiconductor Processing Development of SnS quantum dot solar cells by SILAR method. *Mater. Sci. Semicond. Process.* **27,** 649–653 (2014).
95. Jang, G. G. *et al.* In situ capping for size control of monochalcogenide (ZnS, CdS and SnS) nanocrystals produced by anaerobic metal-reducing bacteria. *Nanotechnology* **26,** (2015).
96. Zhou, Y. L., Zhou, W. H., Du, Y. F., Li, M. & Wu, S. X. Sphere-like kesterite Cu2ZnSnS4nanoparticles synthesized by a facile solvothermal method. *Mater. Lett.* **65,** 1535–1537 (2011).
97. Kamoun, N., Bouzouita, H. & Rezig, B. Fabrication and characterization of Cu2ZnSnS4 thin films deposited by spray pyrolysis technique. *Thin Solid Films* **515,** 5949–5952 (2007).
98. Pawar, S. M. *et al.* Effect of laser incident energy on the structural, morphological and optical properties of Cu2ZnSnS4 (CZTS) thin films. *Curr. Appl. Phys.* **10,** 565–569 (2010).
99. Tooru, T., Daisuke, K., Mitsuhiro, N., Qixin, G. & Hiroshi, O. Fabrication of Cu2ZnSnS4 thin films by co-evaporation. *Phys. status solidi c* **3,** 2844–2847 (2006).
100. Guo, Q., Hillhouse, H. W. & Agrawal, R. Synthesis of Cu2ZnSnS4 Nanocrystal Ink and Its Use for Solar Cells. *J. Am. Chem. Soc.* **131,** 11672–11673 (2009).
101. Suryawanshi, M. P. *et al.* A chemical approach for synthesis of photoelectrochemically active Cu2ZnSnS4 (CZTS) thin films. *Sol. Energy* **110,** 221–230 (2014).
102. Sadeghnejad, A., Lu, L., Kiely, C. J., Berger, B. W. & McIntosh, S. Single

enzyme direct biomineralization of ZnS, $Zn_x Cd_{1-x} S$ and $Zn_x Cd_{1-x} S$–ZnS quantum confined nanocrystals. *RSC Adv.* **7,** 38490–38497 (2017).

103. Letters, C. *et al.* PROPERTIES OF P-TYPE SnS THIN FILMS PREPARED BY CHEMICAL BATH DEPOSITION. *Chalcogenide Lett.* **7,** 685–694 (2010).

104. Henry, J., Mohanraj, K., Kannan, S., Barathan, S. & Sivakumar, G. Structural and optical properties of SnS nanoparticles and electron-beam-evaporated SnS thin films. *J. Exp. Nanosci.* **10,** 78–85 (2015).

105. Ghosh, B., Das, M., Banerjee, P. & Das, S. Fabrication and optical properties of SnS thin films by SILAR method. *Appl. Surf. Sci.* **254,** 6436–6440 (2008).

106. Sohila, S., Rajalakshmi, M., Ghosh, C., Arora, A. K. & Muthamizhchelvan, C. Optical and Raman scattering studies on SnS nanoparticles. *J. Alloys Compd.* **509,** 5843–5847 (2011).

107. Ning, J. *et al.* Facile synthesis of iv–vi SnS nanocrystals with shape and size control: Nanoparticles, nanoflowers and amorphous nanosheets. *Nanoscale* **2,** 1699 (2010).

108. Mani, P., Manikandan, K. & Prince, J. J. Influence of molar concentration on triethanolamine (TEA) added tin sulfide (SnS) thin films by SILAR method. *J. Mater. Sci. Mater. Electron.* **27,** 9255–9264 (2016).

109. Kim, H. & Choi, H. Spectrofluorimetric determination of copper (II) by its static quenching effect on the fluorescence of. *Talanta* **55,** 163–169 (2001).

110. Pawar, S. M. *et al.* Electrochimica Acta Single step electrosynthesis of Cu 2 ZnSnS 4 (CZTS) thin films for solar cell application. *Electrochim. Acta* **55,** 4057–4061 (2010).

111. Nayak, P. K., Garcia-Belmonte, G., Kahn, A., Bisquert, J. & Cahen, D. Environmental Science Photovoltaic efficiency limits and material disorder. *Energy Environ. Sci.* **5,** 6022–6039 (2012).

112. Halder, G., Ghosh, D., Ali, Y., Sahasrabudhe, A. & Bhattacharyya, S. Interface Engineering in Quantum-Dot-Sensitized Solar Cells. *Langmuir* **34,** 10197−10216

(2018).

113. Kamat, P. V, Tvrdy, K., Baker, D. R. & Radich, J. G. Beyond Photovoltaics: Semiconductor Nanoarchitectures for Liquid-Junction Solar Cells. *Chem. Rev.* **110,** 6664–6688 (2010).

114. Dao, V. *et al.* Facile synthesis of carbon dot-Au nanoraspberries and their application as high-performance counter electrodes in quantum dot-sensitized solar cells. *Carbon N. Y.* **96,** 139–144 (2016).

115. Kamat, P. V. Quantum Dot Solar Cells. The Next Big Thing in Photovoltaics. *J. Phys. Chem. Lett.* **4,** 908–918 (2013).

116. Youn, D. H. *et al.* TiN Nanoparticles on CNT–Graphene Hybrid Support as Noble-Metal-Free Counter Electrode for Quantum-Dot-Sensitized Solar Cells. *ChemSusChem* **6,** 261–267 (2013).

117. Chakrapani, V., Baker, D. & Kamat, P. V. Understanding the Role of the Sulfide Redox Couple (S2–/Sn2–) in Quantum Dot-Sensitized Solar Cells. *J. Am. Chem. Soc.* **133,** 9607–9615 (2011).

118. Lee, J.-W. *et al.* Quantum-Dot-Sensitized Solar Cell with Unprecedentedly High Photocurrent. *Sci. Rep.* **3,** 1050 (2013).

119. Finn, S. T. & Macdonald, J. E. Petaled Molybdenum Disulfide Surfaces: Facile Synthesis of a Superior Cathode for QDSSCs. *Adv. Energy Mater.* **4,** 1400495 (2014).

120. Kamat, P. V. Boosting the Efficiency of Quantum Dot Sensitized Solar Cells through Modulation of Interfacial Charge Transfer. *Acc. Chem. Res.* **45,** 1906–1915 (2012).

121. Kamat, P. V. Meeting the Clean Energy Demand: Nanostructure Architectures for Solar Energy Conversion. *J. Phys. Chem. C* **111,** 2834–2860 (2007).

122. Hines, D. A. & Kamat, P. V. Recent Advances in Quantum Dot Surface Chemistry. *ACS Appl. Mater. Interfaces* **6,** 3041–3057 (2014).

123. Halder, G. & Bhattacharyya, S. photoconversion efficiency †. 11746–11755

(2017). doi:10.1039/c7ta00268h

124. Tian, J. & Cao, G. Control of Nanostructures and Interfaces of Metal Oxide Semiconductors for Quantum-Dots-Sensitized Solar Cells. *J. Phys. Chem. Lett.* **6,** 1859–1869 (2015).

125. Thomann, I. *et al.* Plasmon enhanced solar-to-fuel energy conversion. *Nano Lett.* **11,** 3440–3446 (2011).

126. Ha, E. *et al.* Significant Enhancement in Photocatalytic Reduction of Water to Hydrogen by Au/Cu $_2$ ZnSnS $_4$ Nanostructure. *Adv. Mater.* **26,** 3496–3500 (2014).

127. Ghosh, B., Das, M., Banerjee, P. & Das, S. Applied Surface Science Fabrication and optical properties of SnS thin films by SILAR method. *Appl. Surf. Sci.* **254,** 6436–6440 (2008).

128. Jun, H. K., Careem, M. A. & Arof, A. K. Performances of some low-cost counter electrode materials in CdS and CdSe quantum dot-sensitized solar cells. *Nanoscale Res. Lett.* **9,** 1–7 (2014).

129. Li, Y. *et al.* Flexible quantum dot-sensitized solar cells with improved e ffi ciencies based on woven titanium. *J. Mater. Chem. A* **2,** 15546–15552 (2014).

130. Deepa, K. G. & Nagaraju, J. Growth and photovoltaic performance of SnS quantum dots. *Mater. Sci. Eng. B Solid-State Mater. Adv. Technol.* **177,** 1023–1028 (2012).

131. Chen, S., Walsh, A., Gong, X. G. & Wei, S. H. Classification of lattice defects in the kesterite Cu2ZnSnS 4 and Cu2ZnSnSe4 earth-abundant solar cell absorbers. *Adv. Mater.* **25,** 1522–1539 (2013).

132. Woo, K., Kim, Y. & Moon, J. A non-toxic, solution-processed, earth abundant absorbing layer for thin-film solar cells. *Energy Environ. Sci. View* **5,** 5340–5345 (2012).

133. Chen, S. *et al.* Defect physics of the kesterite thin-film solar cell absorber Defect physics of the kesterite thin-film solar cell absorber Cu 2 ZnSnS 4. *Appl. Phys. Lett.* **96,** 1–3 (2010).

134. Washio, T. *et al.* 6 % Efficiency Cu2ZnSnS4 -based thin film solar cells using oxide precursors. *J. Mater. Chem. View* **22,** 4021–4024 (2012).

135. Araki, H. *et al.* Solar Energy Materials & Solar Cells Preparation of Cu2ZnSnS4 thin films by sulfurizing electroplated precursors. *Sol. Energy Mater. Sol. Cells* **93,** 996–999 (2009).

136. Lin, Y., Chi, Y., Hsieh, T., Chen, Y. & Huang, K. Preparation of Cu 2 ZnSnS 4 (CZTS) sputtering target and its application to the fabrication of CZTS thin- fi lm solar cells. *J. Alloys Compd.* **654,** 498–508 (2016).

137. Scragg, J. J., Dale, P. J. & Peter, L. M. Synthesis and characterization of Cu2ZnSnS4 absorber layers by an electrodeposition-annealing route. *Thin Solid Films* **517,** 2481–2484 (2009).

138. Katagiri, H. *et al.* Development of CZTS-based thin film solar cells. *Thin Solid Films* **517,** 2455–2460 (2009).

Biological Information

Hamid Sadeghnejad was born in Kashmar, Mashhad, Iran. He lived in Tehran until the age 28. After the high school, He passed the entrance exam of university and got an admission of AmirKabir University of Technology in chemical engineering in Tehran. He was awarded as a top ten undergraduate students. Based on his ranking, he could continue his education in master degree without any entrance exam in chemical engineering at AmirKabir University. His master thesis was "Antibacterial silver nanoparticles coating on the surface of polyethylene films using corona discharge" in which he synthesized silver nanoparticles. Then corona discharge treated the surface of polymer to make it active for silver nanoparticles coating. The antibacterial properties of nanocomposite was tested by E.coli and S.aureus as a gram positive and gram negative bacteria, respectively. He could publish his master research on 2014 under supervision of Dr. Raisi. After graduation, He started to work at Pardis Technology Park and Bonyan Daneshpajuhan Institute as a R&D process engineer and associate researcher, respectively from 2012 to 2014. Then, he could get an admission in PhD in chemical engineering at Lehigh University, PA at 2014. He Joined Dr.Steven McIntonsh research group and worked on biomineralization of metal sulfides confined as quantum dots. In this research, he studied on bioengineering, enzyme purification, and enzyme utilization to biosynthesis of various quantum dots such as ZnS, SnS, and relative compounds such as $Zn_xCd_{1-x}S$ and CuZnSnS that was applied on solar cell. He could publish his PhD research titled "Single enzyme direct biomineralization of ZnS, $Zn_xCd_{1-x}S$ and $Zn_xCd_{1-x}S$–ZnS quantum confined nanocrystals" in 2017.